NUMERICAL SIMULATION OF TIRE-PAVEMENT INTERACTION FOR NOISE, SAFETY, AND ROLLING RESISTANCE

by

YANGMIN DING

A dissertation submitted to the

School of Graduate Studies

Rutgers, The State University of New Jersey

In partial fulfillment of the requirements

For the degree of

Doctor of Philosophy

Graduate Program in Civil and Environmental Engineering

Written under the direction of

Hao Wang

And approved by

_____

_____

_____

_____

New Brunswick, New Jersey

OCTOBER, 2018

ABSTRACT OF THE DISSERTATION

Numerical Simulation of Tire-Pavement Interaction

for Noise, Safety, and Rolling Resistance

by YANGMIN DING

Dissertation Director:

Hao Wang

Pavement surface is constructed to provide smooth, safe, quiet, and comfortable driving, which plays an important role in traffic noise, wet weather crash, energy consumption and greenhouse gas (GHG) emission. The challenge of providing pavement with low noise, high friction, and less energy consumption requires systematic and accurate study of the tire-pavement interaction mechanism behind each functional requirement, as well as the methods that can be used to tackle the problem. The main objective of this research is to develop and validate numerical models for the above-mentioned tire-pavement interaction mechanisms and investigate the effect of different pavement surface characteristics on noise, safety, and rolling resistance.

Firstly, this study developed a coupled finite element and boundary element method (FEM/BEM) analysis approach for tire-pavement interaction noise simulation and quantified the influence of pavement surface characteristics on generation and propagation of tire vibration noise. Secondly, for safety analysis, this research evaluated hydroplaning risk and skid resistance of multi-lane roadways at different rainfall intensities and the

effectiveness of porous friction course (PFC). An analysis framework and methodology was proposed to incorporate consideration of hydroplaning risk in roadway design. Finally, this study investigated tire rolling resistance from the perspective of pavement and quantified the impact of pavement stiffness on fuel consumption and CO_2 emission.

This study concludes that the pavement surface type with higher texture levels generates greater noise for both porous and non-porous surfaces. The overall noise decreases with the increase of porosity under the same surface texture condition. In addition, the quantification of hydroplaning speed and braking distance using the developed model can help transportation agencies reduce wet-weather safety risk. The study findings can guide the project selection of PFCs at the locations having high hydroplaning risk. Finally, the rolling resistance analysis results indicated the difference of fuel consumption and CO_2 emission affected by asphalt pavement layer thickness and pavement temperature are not significant as compared pavement type (flexible vs rigid). This finding suggested that optimal maintenance of roads with good surface characteristics, such as texture and roughness might be a better way to provide greater fuel economy.

ACKNOWLEDGEMENT

First and foremost, I would like to express my sincere gratitude to my advisor Prof. Hao Wang for his continual guidance, support and encouragement of my Ph. D study and related research. I am deeply inspired by his enthusiasm for research, his immense knowledge and his dedication to profession. He has taught me, both consciously and unconsciously, how to manage time and how to conduct research in an efficient way. It has been an honor to be his student, as well as a great experience working with him.

Besides my advisor, I am also grateful to the members of my graduate committee: Prof. Nenad Gucunski, Prof. Franklin Moon, and Prof. Jingang Yi, for their insightful comments and encouragement, which motivated me to widen my research from various perspectives.

My sincere thanks also go to my colleagues and friends from Civil and Environmental Engineering Department at Rutgers for their encouragement and for all the fun we have had in the last five years. In particular, I am grateful to Dr. Haichao Zhou for his stimulating discussions and tips on my research topic.

Finally, I would like to thank my parents and family for all their love, care and encouragement in all my pursuits. And most of all for my loving, supportive, encouraging, and caring wife, Juan Guo whose faithful support during my entire study.

ACKNOWLEDGEMENT OF PREVIOUS PUBLICATIONS

A part of Chapter 1, 2, 6 and the entire Chapter 3 of this dissertation were previous published by Yangmin Ding and Hao Wang (2017) in International Journal of Pavement Engineering and has been reproduced with permission. Copyright is held by Taylor & Francis. A part of Chapter 1, 2, 4, 6 of this dissertation were previously published by Yangmin Ding and Hao Wang (2018) in Transportation Research Record: Journal of the Transportation Research Board and has been reproduced with permission. Copyright is held by SAGE Publications.

TABLE OF CONTENTS

LIST OF FIGURES

LIST OF TABLES

CHAPTER 1 INTRODUCTION

1.1 Introduction

Traffic noise pollution, wet weather crash and greenhouse gas (GHG) emission have become growing concerns in the modern society. Environmental noise regulations specify the limit value of the outdoor noise level up to 60-65 dB(A). However, the equivalent sound pressure on roads with high volume of traffic can reach up to 75-80 dB(A) (Yoshida et al. 1997). Noise exposure has been proved to cause adverse impact on human health, such as hypertension, hearing loss, sleep disturbances etc. (Nelson 1987; Franssen et al. 2002; Georgiadou et al. 2004).

Wet weather crash is another hazardous that threatens drivers. According to the National Highway Traffic Safety Administration NHTSA data, there are over 5,748,000 vehicle crashes annually, and among which approximately 22% are weather-related in average. It has been recorded that 73% of weather-related crashes happened on wet road surface and 46% are happened during rainfall (Booz 2012). Although statistically the evidence of the exact causes of wet-weather accidents is not clear, it is generally believed that relatively thick water layers and high speeds were primary factors in the loss of traction of the tires on the road surface (Murad et al. 1949, Alvarez et al. 2006, McGovern et al. 2011).

Finally, changes in the greenhouse gas concentrations affect the global warming potential and result in human health consequences. The total U.S. greenhouse gas emissions in 2016 exceeds 6.5 billion ton, of which 28.5% is generated by the

transportation sector (U.S. Environmental Protection Agency 2016). Therefore, it is also urgent to reduce tire rolling resistance for energy savings and GHG emission reductions.

Pavement surface is constructed to provide smooth, safe, quiet, and comfortable driving, which plays an important role in traffic noise, wet weather crash, and GHG emissions. Three performance measures that would quite well represent the major functionality of pavement surfaces within the mentioned topics would be noise emission, wet friction, and rideability. On the one hand, road surface is designed to facilitate safety of travelers. On the other hand, pavement surface should provide comfortable driving (smooth and quiet) without sacrificing safety. The challenge of providing pavement with low noise, high friction, and less energy consumption requires systematic and accurate study of tire-pavement interaction mechanism behind each functional requirement, as well as the methods that can be used to tackle the problem.

Two main approaches are currently widely used to study tire-pavement interaction phenomena: empirical method and numerical method. The first approach is based on field testing and statistical analysis, and as such it is not based on the principles of mechanics. Therefore, the empirical models cannot be applied outside the range of data used to build the models. The second approach, numerical models, on the other hand, is based on the mechanics of interactions between pavement and tire. As those models are based upon physical principles, they can be applied to different road surfaces and various tire types for which the pavement surfaces characteristics and tire configuration data are available. However, due to the complexity of these models, most of the current numerical studies is limited to smooth road surface, ignoring pavement surface characteristics.

Experimental measurements have documented that tire pavement interaction noise, hydroplaning, and rolling resistance are influenced by many factors including tire types, vehicle loading, pavement surfaces characteristics, pavement types, road surface conditions and several other factors. For example, it has been shown that modification of pavement surface characteristics (such as texture and porosity) can result in significant tire-pavement noise reductions (Sandberg and Eismont 2002). In addition, pavement types have been found to impact wet weather road safety. For example, porous pavement courses (PFCs) are found to improved road safety during rain events, by reducing the risk of hydroplaning, reducing splash and spray, and improving the visibility of pavement markings (Alvarez et al. 2009). In addition, tire characteristics and pavement conditions have been identified as influential characteristics on rolling resistance (National Academies of Sciences, Engineering, and Medicine 2007). Therefore, it is important to develop versatile numerical models which can take different pavement surfaces characteristics into consideration, which can be applied to different tire-pavement interaction scenarios after model validation.

1.2 Problem Statement

Pavement surface texture and sound absorption of porous pavement have been found to be two leading factor affecting tire-pavement noise generation and propagation (Sandberg and Ejsmont 2002; Sandberg 1987; Anfosso-Lédée 2002; Nelson 2008; Sakhaeifar et al 2018). Many researchers developed analytical and numerical models for tire-pavement interaction noise and investigated the impact of pavement texture on noise

due to tire-pavement interaction (Beckenbauer 2008; Klein et al. 2008). These studies focused on tire vibration noise of passenger car tires on dense-asphalt road surface and thus cannot consider the sound adsorption of tires on porous road surface. Therefore, it is necessary to develop numerical models to simulate tire-pavement noise on porous pavement surface.

PFCs is used increasingly in the United States due to its safety benefits such as reduced splash and spray, better visibility and reduced hydroplaning risks (Berbee et al. 1999). PFCs are primarily made of open-graded aggregates which are bonded together by polymer-modified binder or resin to form a composite matrix with interconnected voids (Wang et al. 2016; Chen et al. 2018). At low rainfall rain rates or at the onset of rainfall, surface runoff enters the pores in the PFC and flows toward the shoulder. However, the pore space can be filled with water at high rainfall rates or with continuous rainfall, which can cause water to flow both on pavement surface and within the PFC.

In addition, PFCs have been shown to clog over time, which will weaken the subsurface drainage capacity, thus forcing more flow on pavement surface (Suresha 2010). The flow on pavement surface under these conditions is referred to as overland flow or sheet flow, which tends to increase water film thickness along the drainage path. From the perspective of safety, water flow over pavement surface can reduce skid resistance. In addition, the hydroplaning risk on multi-lane roadways with PFCs under different rainfall rates, or when clogging or rutting occurs in PFC, has not been sufficiently studied.

Reduction of tire rolling resistance is a major technical challenge to improve fuel economy as well as to reduce greenhouse gas emissions. Tire hysteresis loss is the primary

reason for tire rolling resistance which is greatly influenced by pavement surface characteristic at different wavelengths, as well as different tire configurations. Most of the current rolling resistance study focuses on either tire structure improvement to reduce energy dissipation or pavement structure-induced rolling resistance due to the mechanical response of pavement by moving vehicle loads (which is related but not real rolling resistance of tire).

Furthermore, many researchers started to investigate the impact of tire-pavement interactions of different pavement surface characteristic such as textures and surface deflections on tire rolling resistance, which is the key to understanding the role of pavement surface on rolling resistance for the reduction of energy consumption and design of environmentally friendly pavement. Although a wide range of literature results can be found, there is still much confusion and uncertainty about to what extent and under which conditions (pavement type and temperature) pavement stiffness is an important factor influencing tire rolling resistance.

1.3 Objective and Methodology

The main objective of this study is to develop and validate numerical models for tire-pavement interaction mechanisms including noise, safety, and rolling resistance, and investigate the effect of influential factors of different pavement surface characteristics (pavement texture, porosity), pavement types (rigid or flexible surface, permeable pavement) and pavement conditions (pavement rut, cross slop etc.) on the above-mentioned mechanisms. Figure 1.1 presents the framework of tire-pavement interaction analysis.

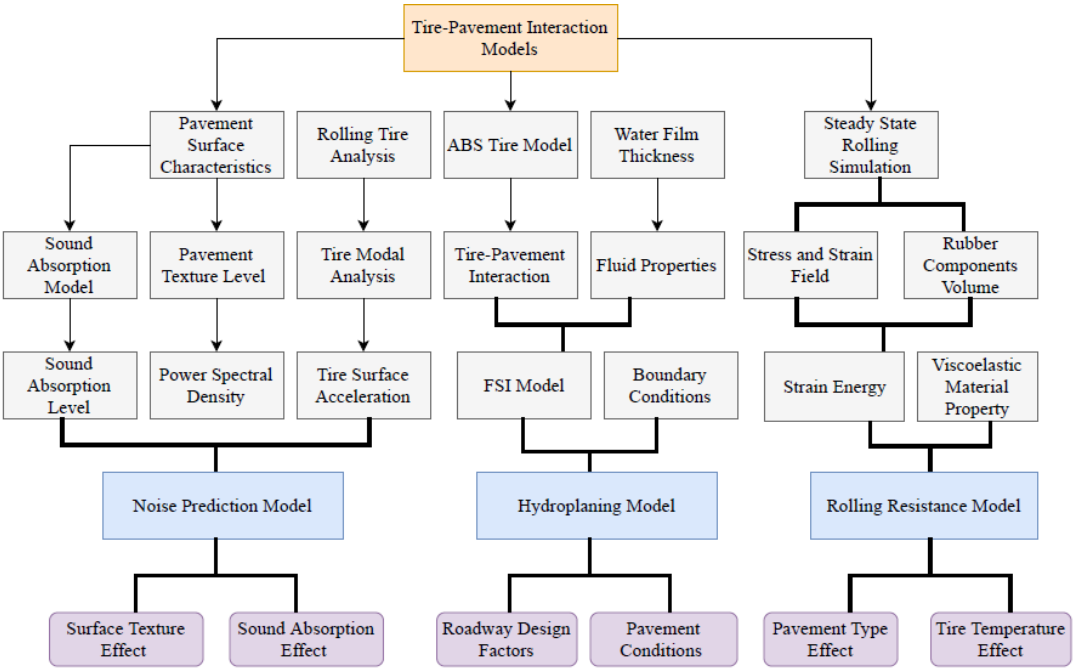

Figure 1.1 Framework of tire-pavement interaction analysis

To achieve this objective, the following research tasks will be conducted:

1) To develop a coupled finite element and boundary element method (FEM/BEM) analysis approach for tire-pavement interaction noise simulation and quantify the influence of pavement surface characteristics on generation and propagation of tire vibration noise. The FEM/BEM approach was validated to predict tire-pavement noise for passenger car tires considering various surface characteristics.

2) To develop fluid–structure interaction models for hydroplaning and skid resistance analysis for specific tires based on fluid dynamics and FEM. To Investigate skid resistance and braking distance at various vehicle speed and different water film depths.

3) To propose an analysis framework and methodology to incorporate consideration of hydroplaning risk, skid resistance and braking distance in roadway design with PFCs,

which enables highway agencies to assess and evaluate hydroplaning potential of PFCs with different design parameters

4) To investigate tire rolling resistance from the perspective of pavement, considering energy loss in the tire contributed by pavement structure factors. These are pavement types (rigid vs flexible) and surface layer thickness. The impact of pavement stiffness on rolling resistance was analyzed and compared with related experimental studies.

1.4 Scope

This dissertation is divided into six chapters. The first chapter gives an overview of problem statement, objective, and methodology. The second chapter reviews the existing literature on numerical modeling of tire-pavement interaction noise, tire hydroplaning, and tire rolling resistance. The third chapter describes the tire-pavement interaction noise model and analyzes the overall noise level under different surface characteristics. The fourth chapter presents the development of numerical model to evaluate hydroplaning risk of multi-lane roadways with PFCs at different rainfall intensities and pavement conditions. Discussion of wet road surface skid resistance and braking distance is also presented in this chapter. The fifth chapter focuses on the prediction of rolling resistance of rolling tire and quantifies the effect of pavement deflection, pavement surface thickness, and temperature on rolling resistance. The final chapter presents research findings, conclusions, and recommendations of future study.

CHAPTER 2 RESEARCH BACKGROUND

2.1 Tire-Pavement Interaction Noise

2.1.1 Tire-Pavement Noise Generation Mechanisms

To better understand the influence of pavement surface characteristics on tire-pavement interaction noise, it is necessary to sutdy the mechanisms of noise generation and propagation. The tire-pavement interaction noise is affected by the properties of both tire and pavement surface, and the complex interaction mechanisms between these two factors. At the tire-pavement interface, energy generated by several mechanisms eventually radiated as sound.

In general, tire-pavement noise mechanisms can be classified into two categories: the vibration-related mechanism and aerodynamically-related mechanisms. In vibrational noise, the tire tread impact and adhesion are the major sources, while in aerodynamical noise, the pipe resonance and air pumping are main contributions. It has been found that vibrational noise is the dominant noise generation mechanism in tire-pavement interaction noise (Yang 2013).

Vibrational noise can be further categorized into noise caused by radial and tangential vibration of the tire, sidewall vibrations, stick-slip effects, and adhesion stick-snap. On the one hand, when a vehicle traveling at a certain speed, the tire interacts with road surfaces, the friction force at the interface causes tangential strains on the tread block, thus causing the tread vibration in the longitudinal direction. On the other hand, the deformation of the

tread generated by road roughness causes radial vibration of tire belts, which contributes to radial vibration noise.

In addition, the deformed sidewall acts as a channel to propagate the sound from tread vibrations. Stick-slip effects are caused by the change of friction force at the tire-pavement interface, when the tire tread blocks stick and slip back and forth on the road surface. Adhesion stick-snap occurs as adhesion forces at the contact patch which push the air out and into tread ribs and grooves.

Table 2. 1 Generation Mechanisms of Tire-Pavement Noise (Sandberg and Ejsmont 2002)

Tire-pavement noise generation mechanism	**Vibrational (structure -borne)**	**Impact mechanism (mostly radial vibrations)**	Tread impact: radial or tangential vibrations caused by tread blocks, spreading to sidewalls
			Texture impact: radial or tangential vibrations caused by texture, spreading to sidewalls
			Running deflection of tire tread at leading and trailing edges, causing belt or carcass vibrations
		Adhesion mechanism (mostly tangential vibrations)	Stick-slip: tangential vibrations caused by tread element motions relative to road surface
			Adhesive effect: tangential or radial vibrations caused by rubber-to-road stick/snap
	Aerodynamic (air-borne)	**Air displacement mechanisms**	Air turbulence: turbulence around rolling tire due to tire displacing air, and air dragged around by the spinning tire/rim
			Air-pumping: air displaced into/out of cavities in or between tire tread and road surface
			Pipe resonances: air displacement in grooves in tread pattern amplified by resonances
			Helmholtz resonance: air displacement into/out of connected air cavities in tread pattern and surface amplified by resonances

Aerodynamic noise can be divided into noises caused by air turbulence, air-pumping, pipe resonance, and Helmholtz resonance. Air turbulences noise is mainly resulted from the turbulence around rolling tire due to tire displacing air. As the most common aerodynamic mechanism, air-pumping occurs when the entrapped air at the tire-pavement interface is compressed and pumped out. Both pipe resonances and Helmholtz resonances are a sound amplification mechanism. The sound is amplified when air is pushed into or out of the connected air cavities in tread ribs or grooves. The above-mentioned noise generation mechanisms are briefly summarized in Table 2.1.

2.1.2 Tire-Pavement Noise Measurement

There are a variety of methods to measure tire-pavement interaction noise in the field and in the laboratory, including the Coast-By (CB) method, the Close-Proximity (CPX) method, the laboratory drum (DR) method, and the Trailer Coast-By (TCB) method (Sandberg and Ejsmont 2002).

In the CB method, the test vehicle is equipped with text tires and roll past a roadside microphone with the engine shut off and the transmission disengaged (“coast by”). This method has the advantage of excluding engine and drive-train noise. The maximum A-weighted noise level and the frequency spectrum can be recorded during the test. This method is often used to identify the effect of road surface and tire on noise level.

In the CPX, the test tire is mounted on a trailer which is towed by a towing vehicle. The microphone (up to five microphones) are located within 0.1-0.5 range of the tire. The microphones are protected with sound absorbing materials to avoid noise from wind and

other traffic noise. Compared with CB method, the CPX method requires fewer test tires and it minimizes the influence from other traffic. The CPX method is also one of the most common noise level measurement techniques.

In the DR method, the test tire is mounted to roll against a drum facility. The microphones are put in a similar position as in the CPX method. The drum can be equipped with a molded replica of a road surface to take pavement surface characteristics into consideration. The drum method is often used in tire noise generation studies.

The TCB method is a hybrid of the CB method and CPX method. In this method, a trailer is towed by a vehicle along the test track and the microphones are placed as in the CB method. However, the noise level obtained is the maximum value when the trailer is passing by not the noise level when the entire vehicle pass-by.

2.1.3 Factors Affecting Tire-Pavement Noise

Vibrational and aerodynamic mechanisms play an important role in the generation of tire-pavement noise, and their impact could be influenced by many factors. These include tire configurations, tire material etc. from the tire aspects and pavement surface texture, sound absorption etc. from the pavement aspects. The knowledge of the interaction mechanism of these factors can better assist researchers find more effective methods to reduce tire-pavement noise. Evaluation of influential factors of tire-pavement interaction noise is discussed in this section.

Previous research studies have found that tire-pavement noise levels can be reduced by the optimization of tire dimensions. Walker and Wiliams (1979) tested the impact of

tire width on tire-pavement interaction noise. In their study, two passenger car tires are tested, and the results show a consistent increase of noise level with width, in the range of 0.2-0.8 dB per 10 mm width increase is obtained. However, later study by Sandberg (2002) found that truck tires seem to emit lower noise levels with wider tire width.

Several studies examined the influence of tire structures on tire-pavement noise (Ejsmont 1982; Kropp et al. 1998; Sandberg 2002). Ejsmont (1982) found that the increased tire belt stiffness reduces the tread vibration. Kropp et al. (1998) further indicated that both stiffness and mass of the belt should be modified when aiming for a reduction of tire noise.

Many studies have been done to study the mechanism of tire-pavement noise and related influential parameters and found that pavement texture and sound absorption are two leading factors in tire-pavement interaction noise generation and propagation (Sandberg et al. 2002; Sandberg 1980; Anfosso-Lédée 2002; Nelson 2008). Pavement texture cause time-varying contact forces at the tire-pavement interface and causes tire vibration noise. Porous asphalt pavement has been used as a promising approach to reduce traffic noise because some sound waves are absorbed by the porous layer due to its porosity.

Field testing have been conducted to study the effects of road surface texture and pavement porosity on tire-pavement interaction noise. The early studies by Sandberg (Sandberg 1987) showed that the noise levels at low frequencies are mainly influenced by higher macro-texture and International Roughness Index (IRI); while noise levels at higher frequencies are affected by the higher porosity. Field evaluation of the measured noise

levels of different mix types in California indicated a relationship between pavement characteristics and frequency-related acoustic impact (Ongel et al. 2011).

Liao et al. (2014) investigated the impact of pavement surface characteristics of individual and multiple road surfaces on noise based on the field data collected from the National Center of Asphalt Technology (NCAT) test track. It was found that mean profile depth (MPD) increased noise levels below frequency of 1600 Hz, especially on impervious asphalt pavement, but road surface porosity caused noise levels decreasing throughout the entire frequency range (except at 2500 Hz) on the open-graded asphalt pavement.

Li et al. (2014) carried out laboratory measurements to investigate the effects of mixture composition, surface texture and sound absorption on the noise of thin asphalt slab. The results demonstrated that tire-pavement noise level is determined by the combined effects of material properties and surface characteristics of surface materials.

2.1.4 Modeling Tire-pavement Noise

The modeling approach used in various researches to simulate tire-pavement noise can be divided into three categories, including statistical models, hybrid models and deterministic models. Statistical models have been developed using field measurements to predict tire noise considering tire type, road surface texture, load, and driving speed. The first generation of models established the direct relationship between the measured noise and texture spectrum parameters (Sandberg et al. 1980). Although the model formats are simple, it allows for comparison of approximate noise level of different road surfaces, the accuracy of models depends on the range of texture parameters included in the field testing.

It was found that these models cannot differentiate the effects of positive and negative textures.

One of disadvantages of statistical models is that these models have limited accuracy, due to the limitation of the test conditions. Therefore, hybrid models have been developed that could include large input parameter sets to achieve better accuracy. Two well-known hybrid models are the Statistical Physical Explanation of Rolling Noise model (SPERoN) and Hybrid Rolling Noise Estimation (HyRoNE). Both models combine statistical data with physical models to obtain the pass-by noise levels generated by passenger cars (Beckenbauer et al. 2008).

The SPERoN model uses driving speed, road surface texture, airflow resistance, and tire characteristics as inputs, and it is restricted to impervious, non-sound absorption pavement surfaces only, such as dense pavement surfaces. In contrast to the SPERoN model, the HyRoNE model is capable to be applied to sound absorption surfaces by including absorption properties and porous layer thickness. However, the HyRoNE model only fits for one specific tire.

Deterministic models are designed to study the process of noise generation and propagation, which requires tire parameters and air properties. Rustighi and Elliott (2005) adopted a 3D finite element approach to predict the interior and exterior tire noise under the stochastic tire vibration under the excitation of the spectral density a road profile.

Fujikawa and Koike (2005) studied the influence of pavement roughness on tire vibration noise and found that the height, radius, and spacing of surface asperities were important for tire vibration noise mitigation.

O'Boy and Dowling (2009) presented a method to determine the far-field radiated noise for a patterned tire on two rough road surfaces. These studies focused on tire vibration noise on dense-asphalt road surface and thus cannot consider the sound adsorption on porous road surface.

Zhang and Ong (2015) adopted a coupled finite element and boundary element numerical simulation model to examine tire-pavement interaction noise propagation and reduction under the effect of pavement texture.

All the models reviewed are focused on passenger car tires. In addition, most models focus on the noise caused by texture induced vibrations of the tire. The growing attention for porous surfaces necessitates improvement of the models in that direction.

2.2 Tire Hydroplaning

2.2.1 Hydroplaning Generation Mechanism

As one of the key issues for safe driving on a wet pavement, hydroplaning occurs when a tire loses contact with water-covered road surface by the actions of water pressures that build up with increasing vehicle speed (Ding and Wang 2018). At a critical speed, also called hydroplaning speed, the tire will lose contact with road surface. Partially hydroplaning occurs when the shear force at the contact patch is reduced but not completely lost, and thus leading to a part of the tire contact patch being separated by water. As the water continually penetrates the contact area, the shear force will be substantially reduced, which makes it impossible to control the vehicle, thus totally hydroplaning occurs (Martin

1966). This type of hydroplaning should be controlled accordingly, to improve driving safety.

Hydroplaning can be divided into three categories, depending on the different mechanism at tire-pavement contact patch, which including dynamic hydroplaning, viscous hydroplaning and reverted rubber hydroplaning (Horne 1963).

Dynamic hydroplaning results from the tire-fluid interaction which produces uplift forces on tire. At ordinary driving speed, or small water film thickness, since the water pressure is not high enough to uplift the tire, thus partial dynamic hydroplaning may occur. Generally, full dynamic occurs when the water film thickness exceeds 2.5 mm (Yager et al.1970).

In contrary to dynamic hydroplaning occurs at high tire speed and deeper water film, viscous hydroplaning usually happens at thin water film thickness (water film thickness less than 0.25 mm), and at low driving speed on damp or wet runways (Leland et al. 1968).

Horne (1968) found out that viscous hydroplaning may be easier to occur at smooth pavement where the texture is not enough to dissipate the thin viscous. Reverted rubber hydroplaning happens when a tire sliding on the road surface. In addition, poor pavement condition, high driving speed, wet or flooded pavement and deficient brake system can all contribute to this type of hydroplaning.

A study carried out in Florida by Gunaratne et al. (2012) reviewed the models for predicting hydroplaning risk and compared them against experimental study and wet weather crash statistics obtained from the Florida Department of Transportation (DOT).

The study developed an alternative set of hydroplaning models and investigated the impact pavement properties on hydroplaning.

More recent study conducted by Flintsch et al. (2014) defined critical precipitation as the minimum intensity of precipitation that puts enough water on the pavement to cause disturbing splash and spray. They found that the water film thickness is a function of rainfall intensity, the geometric properties of road surface, and infiltration rate.

2.2.2 Hydroplaning Measurement

Generally, wheel spin-down is often used in the field as the indicator of tire hydroplaning (Stocker 1974). Spin-down describes the loss of angular velocity of a wheel traveling over a flooded pavement as the speed of the vehicle remains constant or increases. Wheel spin-down is found to be caused by the generation of hydrodynamic pressure in the forward portion of the tire-pavement contact patch. This force acts to oppose the rotation of the tire and can cause the tire to stop completely. It has been assumed that when spin-down starts, some loss of tire-pavement contact will occur. When a part of the contact is lost, the friction at the contact patch is decreased.

The wheel spin-down test is usually conducted by towing a single test tire in a water trough which is 800 feet long and 30 inches wide. The trough can maintain uniform water depths up to 0.75 inches to allow test tires to be completely flooded. In the test, the trailer is can be loaded with one or two steel plates. A fifth wheel on the tow vehicle and an axle tachometer are used to monitor the towing speed and the test wheel speed, respectively. When the test tire reaches free rolling state, the spin-down generally stabilizes at around 2

mph below the tow speed. The hydroplaning is determined by an abrupt spin-up as the test tire exists onto dry road surface. The initial testing speed is at 45 mph and the tow speed is gradually increased during the test until hydroplaning occurs (Tielking 1992).

2.2.3 Factors Affecting Hydroplaning

The main factors affecting hydroplaning are pavement surface characteristics, pavement types, tire tread design, and tire operating condition.

Microtextured pavement surfaces has been found to have lower hydroplaning risk (Balmer and Gallaway 1983; Horne and Dreher 1963). Researcher found that pavement microtexture helps reduce viscous hydroplaning potential, while pavement macrotexture could postpone hydroplaning (Mosher 1969). Although the influence of pavement microtexture depth on hydroplaning risk is not yet quantified, but studies show that microtexture affect the relationship between coefficient of friction and the water film thickness (Pelloli 1977).

Besides microtexture, macrotexture also play a great role in the risk of hydroplaning. Macrotexture provides good friction in wet weather conditions to reduce hydroplaning risk at high vehicle speeds (Balmer and Gallaway 1983; Horne and Dreher 1963). Hibbs and Larsen studied the effect of macrotexture on hydroplaning, and they found that when vehicles speed reaches to 50 mph (80 km/h) or greater, it usually requires better macrotexture to help prevent hydroplaning (Hibbs and Larsen 1996).

Tire tread is designed to provide channels for water to flow out from the tire grooves. It has been found that smooth tires is more prone to hydroplane than grooved tires. Previous

researches (Horne and Dreher 1963; Gallaway et al. 1979) have found that tire treads help in expulsion of water from the contact patch by providing escape channels, which reduces hydroplaning risk. A tire with deeper tire depth provides a more efficient channel for the flow of water, and thus hydroplaning requires higher speed to occur since less water pressure is built up at the contact patch.

Previous researches indicated that the increase of tire pressure will reduce hydroplaning risk (Horne et al. 1963). The reason behind this principle is that higher inflation pressure will result in greater rigidity of tire, which will reduce tire inward bending under the impact of fluid inertial forces.

Browne (1975) found that the increase of tire pressure will increase the average pressure at the contact patch, which will reduce the degree of membrane penetration and reduce hydroplaning potential. Tire tread grooves serve a passage for discharging water from the tire contact patch to reduce hydroplaning potential. Yeager and Tuttle (1972) found that when the tire inflation pressure increases, the occurrence of tire tread groove closure is reduced.

Staughton (1970) studied the relationship between water film depth and hydroplaning and showed a higher water film depth increase hydroplaning potential. It is known that for smooth surfaces and tread tires, hydroplaning occurs at water film thickness as low as 0.5 mm (Harrin 1958).

It has been found by Gunaratne et al. (2012) that wider road sections are more prone to hydroplane and dense-graded pavements are more likely to induce hydroplaning than open-graded pavement surfaces.

2.2.4 Modeling Tire Hydroplaning

Martin (1966) combined potential flow theory with conformal mapping technique to study the total dynamic hydroplaning problem. A two-dimensional non-rotational flow problem with a rigid surface of arbitrary shape placed on an incompressible non-viscous fluid was solved. However, side flow and viscosity were completely ignored in the analysis.

Moore (1967) simulated a rubber block sliding on a 2D smooth sinusoidal asperity separated by a thin film of water. The 1D Reynolds equation was used to correlate load capacity, friction coefficient and minimum clearance. However, this study neglected the side flow and can only be applied in viscous hydroplaning.

Eshel (1967) built a three-region model in which different simplified assumptions were applied to the flow in each region. The solutions obtained from the three regions were coupled at the boundary of the region. A simple model of tire flexibility is coupled to form an elastoplastic fluid dynamic system. However, the model also cannot take the side flow in the inlet region under the tire into consideration. In addition, in the study the hydroplaning was analyzed as a 2D problem and a laminar parabolic velocity profile was assumed, which is inappropriate and inaccurate.

Daughaday and Tung (1969) introduced a 3D tire surface hydroplaning model by using a two-region model. The main drawback is that the planar footprint regions cannot produce the magnitude of the recovery factor when hydroplaning occurs. Therefore, it requires tire deformation for accurate prediction.

Later Browne (1971) proposed a 2D process for the 3D tire deformation model to study hydroplaning by solving the Navier-Stokes equations. In the model, the analysis was conducted with different fluids models including inviscid, laminar and turbulent models. In addition, the side flow was also considered in the analysis. The results showed that the inward bending of tire tread at contact patch was a major cause of hydroplaning. In addition, the results indicated that the viscosity effect is only significant for hydroplaning when the combined drainage capacity of the tread grooves and pavement macrotexture exceeds the amount of water flow at the tire contact patch.

Grogger and Weiss (1996) investigated the pressure distribution and velocity field of a deformable tire when hydroplaning. The 3D flow around the tire is described by the efficient free surface model and the Navier-Stokes equations. The tire deformation was calculated by finite element method. It confirms that the tire deformation has a strong influence on the resulting lift forces, as reported by Browne (1971).

Seta and Nakajima et al. (2000) employed FEM for tire and FVM for water to simulate tire hydroplaning. In the fluid-structure interaction analysis, a rolling tire with actual tread pattern was considered, however, the effect of fluid viscosity was ignored. The prediction of hydroplaning velocity was also not achieved.

Okano and Koishi (2001) predict the hydroplaning speed for tires with four different tread patterns by using used MSC.Dytran. However, the study has the disadvantage of modeling the fluid flow using the potential flow theory.

Oh et al. (2008) studied tire hydroplaning by using two separate mathematical models. In the analysis, the Navier-Stokes and continuity equations was solved by the finite

difference method (FDM) approach. The pressure distribution at the contact zone was obtained considering the inertia and viscous effects of water. The deformation of the FEM tire model was obtained under the vertical tire load and inflation pressure.

Recently, Ong and Fwa (2005; 2006a; 2006b; 2007; 2008; 2009) have developed a numerical hydroplaning model using Computational Fluid Dynamics (CFD) techniques to examine the impact of pavement grooving size on passenger car hydroplaning. In the study, only smooth tire is considered. The simulation results were validated against with previous experimental results and the NASA hydroplaning equation. Their study showed that the NASA equation underestimated hydroplaning speed for a passenger car tire on transverse and longitudinal pavement grooving designs.

Dong et al. (2013) used Finite Element Method (FEM) to get the tire deformed mesh and then imported the tire deformation into Fluent to solve the water flow with the use of the VOF model and the standard k-ε turbulence model. The method was further used to investigate hydroplaning risks under different tire operational conditions.

Similarly, Zhou et al. (2014) used the finite element method to extract the tire deformation with a wheel load of 4,000 N. After the combination of the extracted tire deformation and the whole computational domain, they applied the three-dimensional SST *k-ω* coupled with the VOF model to Fluent to simulate the hydroplaning velocity of the tire's circumferential grooves.

A few studies have focused on the potential safety issues under wet weather on PFCs. Zhang et al. (2013) present a numerical fluid-structure interaction model to investigate the wet skid resistance of porous and nonporous pavements.

Later on, Zhang et al. (2016) used the same numerical model to analyze the effect of roadway width on skid resistance of porous pavement. These studies considered the simplified tire geometry: a standard bias passenger car tire with smooth treads (no grooves). The skid resistance was determined under the locked wheel conditions at high rainfall rates. The water film thickness was computed by the PAVDRN software which requires the input of rain rates, roadway geometry, and hydraulic properties of porous pavement. However, the PAVDRN software ignores the subsurface flow in porous pavements.

The aforementioned studies focused on hydroplaning risk either under locked wheel conditions or free rolling conditions on impervious pavements. The water film thickness in these models is often arbitrarily assumed, which is not directly related to rainfall intensity and pavement geometric characteristics.

2.3 Tire Rolling Resistance

2.3.1 Mechanism of Rolling Resistance

Tire deformation at the tire-pavement contact zone, the aerodynamic drag of the rotating tire and the slip between tire and road surface or tire rim are three major contributions to tire rolling resistance. Tire deformation is the most influential part of tire rolling resistance due to the following phenomena, which result in deformation induced viscoelastic energy loss in tire structure:

1) tire crown bending at the contact patch under tire load;
2) tire sidewall bending under tire load;

3) tire tread compression at the tire-pavement contact zone;

4) tire tread and sidewall elements shearing.

The belt portion of the carcass is inelastic and has a fixed length. In the case where rubber is present under and above the belt, and also when the tread is bent at the leading and trailing edges of the contact zone, this means that the inner rubber layer is compressed, and the outer rubber layer is expanded. The change in edge radius and the friction of the layer will appear as hysteresis loss, which contributes to rolling resistance. (Sandberg et al. 2011).

The main contributing factors of rolling resistance are energy dissipation and aerodynamic drag during rolling. The energy dissipated in the heat is an indication of the hysteresis force caused by the radial deformation of the rolling tire. Hysteresis damping will cause a higher pressure in the front contact zone, thus creating a lower pressure in the latter half of the contact zone, which results in a center shift of the pressure at contact patch in the rolling direction.

The change in the pressure center creates a moment near the center of the tire. The shear force exists between the contact patch opposite to the longitudinal motion. This shearing torque counteracts the rolling moment. However, in order to balance the overall force of the system to cause the vehicle to maintain travelling at a constant speed, there will be a force resulted from the center of the hub that pushes the tire in the positive longitudinal direction and the value of the force should equal to the negative x direction shear force at contact patch.

2.3.2 Rolling Resistance Measurement

Tire rolling resistance can be measured both in the laboratory and in the field by the Drum test, the Trailer method, the Coast-down method and the Fuel consumption method.

The Drum test can be sued to measure the rolling resistance force of the tire. In the Drum test, the loaded tire is hold up against a rotating drum, and the tire rolling resistance force can be calculated from measuring the resistance the tire exerts on the rotating drum. The advantage of this methods is that it minimize the influence of other factors on tire rolling (Clark 1978).

The Trailer method measured the rolling resistance force of test tires which are towed by a vehicle. The trailer method has been used to assess tire rolling resistance and correlate it with pavement surface profiles spectra (Descornet 1990).

The Coast-down method identify all major influential factors related to tire driving resistance besides tire rolling resistance force. In the Coast-down method, the test vehicle roll freely in neutral gear or clutch down after accelerating to a specific speed (Evans and Zemroch 1984). Instead of measuring tire rolling resistance directly, the measured data must be fitted into mathematical models depending on the experimental settings and source of data.

Fuel consumption method is one of the most popular method to measure rolling resistance, which can include various factor affecting tire rolling resistance. However, this method requires complex fuel consumption models for data analysis and usually includes extra sub-models, such as engine model, powertrain model, and road surface model. In addition, the fuel consumption model might not be able to separate the rolling resistance

loss from other inflectional factors that contribute to energy loss of the test vehicle (Greenwood and Bennett 2001).

2.3.3 Factors Affecting Rolling Resistance

Rolling resistance is depending on a variety of factors, such as tire configuration, vehicle operational condition, and pavement surface characteristics. Over the years, rolling resistance data obtained from experimental study has been used for the analysis of vehicle fuel consumption. Many fuel consumption models are polynomial expressions, which have coefficients determined by curve fitting to experimental values (Grover 1998). The method only works for specific tire type and does not explain the mechanism or physical process of rolling resistance. Therefore, it is important to study the influential factors on tire rolling resistance.

Tire dimension is one of the key parameters affecting tire rolling resistance and fuel consumption. Wong (1978) conducted an experimental study to investigate the relationship between rolling resistance coefficient and tire diameter. The study found that the tire rolling resistance increases as the increasing of tire diameters depending on different road surfaces, with deformable surfaces is most obvious.

Nielsen (2002) developed a mode to include temperature variations with change in velocity to predict rolling resistance. The study confirmed that tire rolling resistance change cannot simply explained by the change of tire velocity which is accompanied by a change of the air temperature inside the tire.

Pavement properties such as surface texture, roughness and pavement stiffness have been found to play an important role in the overall rolling resistance. Pavement deflection has also been suggested as an influential factor of rolling resistance. The principle behind this theory is that when tire interacts with road surface, energy is lost due to pavement deflection (Schmidt 2010).

Velinsky and White (1979) experimentally studied the impact of pavement roughness on vehicle dissipated energy. The measure data were correlated with simulation data to build up models that includes tire pressure, vehicle speed, and pavement roughness as inputs. The results showed that the rolling resistance was increased by pavement roughness. Thus, pavement roughness plays a significant role in total energy consumption and dissipation.

Using the spectral density function, Lu (1985) simulated how rolling resistance is affected by road roughness with a quarter car model. Similar with other researches, this experiment focused merely on the effect of pavement roughness on rolling resistance. The study found that rolling resistance increases with the increase of the roughness.

Clapp and Eberhardt (1986) conducted numerical analysis to evaluate the effect of pavement texture on fuel consumption. The numerical model has a tire-induced contact, and they study found pavement texture affects fuel consumption by changing the contact patch area.

Delanne (1994) conducted field test at the Nantes Test Track to study fuel consumption of light vehicles under the effects of pavement smoothness and macrotexture.

The study showed that the fuel consumption exponentially increases with the increase of pavement texture and unevenness.

Taylor (2000) conducted an experimental study to evaluate how fuel consumption of heavy trucks was influenced by factors such as pavement structure, roughness. The study found that there was 11% higher fuel consumption on asphalt pavement compared to rigid road surface depending on vehicles speeds.

Soliman (2006) used a quarter car model combing rolling resistance model to study the rider comfort under the impact of pavement roughness. It was shown that the rolling resistance coefficient varies with the road roughness coefficient and the vehicle speed.

Some studies based on measured results reported there is no statistical difference of pavement deflection on rolling resistance, while some researchers have reported the differences could range from small to significant (Walter and Conant 1974; Bester 1984; Taylor and Patten 2006; Lu et al. 2010; Pouget et al. 2012).

Benbow et al. (2007) found that the average rolling resistance measured on rigid pavement surface was about 5% lower than that obtained on asphalt pavement. Studies by Sumitsawan et al. (2009) indicated the observed difference in fuel consumption rate was statistically significant at 10% level of significance with the rate for concrete pavement being lower.

More recent studies from other researcher further concluded that pavement stiffness should be considered as an important influential factor of tire rolling resistance (Sandberg 2011). However, uncertainties from field testing makes it difficult to separate and quantify

the pavement deflection effect on rolling resistance from other surface characteristics, such as pavement texture and roughness.

2.3.4 Modeling Rolling Resistance

Rolling resistance modeling has been considered to be very complicated due to the viscoelastic and dynamic hysteresis characteristics of rubber materials. In addition, the tire operating conditions such as tire load, inflation pressure, tire deflection and pavement surface conditions, make it even more complicate.

Williams and Dudek (1983) studied how the footprint load-deflection hysteresis affect tire rolling resistance drag force. They also investigated the percentage of rolling resistance due to tire tread and sidewall deforamtion.

Shida and Koishi et al. (1999) simulated tire rolling resistance using FEM. In the analysis, the tire stress and strained field were extracted from the tire static deflection analysis under vertical load and inflation pressure, which are used together with the loss factors of rubber components to estimate the energy loss of the tire.

Hysteresis losses result in heat energy, which will result in higher inflation pressure, which will lower tire rolling resistance and fuel consumption. A semi coupled representation have been sued to model the total behavior, which requires three sub models including the dissipation model, deformation model, and thermal model.

Park et al. (1997) calculated the temperature distribution of a rolling tire by using these models and viscoelastic theory. The prediction results were compared against the

measurement and comparisons were made between linear and quadratic finite element models.

Ebbott et al. (1999) used the FEM to predict tire rolling resistance and temperature distributions. The prediction results were also validated against the measured data, respectively for passenger car tires and radial medium truck tires.

Narasimha (2006) used a three-stage FE model to study characteristics for tires with different tread patterns. A sensitivity analysis was made with various operating conditions aspects (tire rolling speed, tread profile, tire loading and ambient temperature).

Ullidtz et al. (2010) found that the rolling resistance due to pavement deflection only account for about 4% of total rolling resistance. Akbarian et al. (2012) showed that pavement deflection resulted from material stiffness could affect fuel consumption by 4%.

Srirangam et al. (2015) developed a thermomechanical FEM model for the quantification of the influence of tire-pavement operating conditions on rolling resistance. Their study claimed that an asphalt surface with higher macrotexture result in higher rolling resistance.

Coleri and Harvey et al. (2016; 2017) found that different pavement structure and pavement temperature might be result in different excess fuel consumption.

Balzarini et al. (2017) studied the effect of structural response of concrete pavement on rolling resistance and vehicle fuel consumption based on FEM. Their study found the fuel consumption due to structural response is less than 0.1% of the total fuel consumption of the truck.

2.4 Summary

A review of modelling of tire-pavement interaction noise, tire hydroplaning, and tire rolling resistance was presented in this chapter. The review shows that numerical study has been widely used in studying tire-pavement interaction phenomena, and to some extent, pavement surface characteristics have been considered. Specifically, FEM have been shown to accurately predict the tire-pavement interaction, and experimental studies show that pavement surface characteristics play an important role in tire-pavement interaction.

However, the review also indicates most of tire-pavement interaction research ignores pavement surface characteristics. Most studies on tire pavement noise focus on dense-asphalt road surface, ignoring the sound absorption effect on noise.

Limited studies have focused on the potential safety issues under wet weather on PFCs. In addition, most numerical studies considered simplified tire geometry (bias passenger car tire with smooth treads), and the water film thickness ignored the subsurface flow in porous pavements.

For rolling resistance, most researchers focused on the energy dissipation due to pavement deformation instead of tire itself. Their studies provide important information about pavement structure on viscoelastic dissipation in asphalt layers related to fuel consumptions. However, the true tire rolling resistance due to pavement deformation needs to be captured.

CHAPTER 3 MODELING OF TIRE-PAVEMENT INTERACTION NOISE

3.1 Tire-Pavement Noise Prediction Model

3.1.1 Tire-Pavement Vibration Model with FEM

In this study, a continental 195/65R15 tire under the load of 4000 N with the inflation pressure of 200 kPa and tire speed of 70 km/h was used in the simulations. The following main characteristics of the tire model are considered:

(1) the composite material and the anisotropy resulted from the stiffness difference between rubber and reinforcement;

(2) the relatively large deformation due to the flexibility of tire carcass during tire-pavement interaction;

(3) the nearly incompressible and nonlinearity of rubber (Wong 1993). To capture the above-mentioned characteristics, different tire components were considered in the tire model having different material properties.

The tread and sidewall of tire were made of rubber, while the steel belts and radial ply were considered as steel reinforcement embedded in rubber components. The rubber is modelled as hyperelastic material to capture its incompressibility and nonlinearity (Hernandez and Al-Qadi 2016), while the belt reinforcement is modelled as linear elastic material with high modulus. On the other hand, the road surface is modelled as an analytical rigid body.

The simulation of FE tire model includes three steps. Firstly, an internal inflation pressure is applied on the axisymmetric tire model. Secondly, a full three-dimensional tire model is generated by using the symmetric results transfer and symmetric model generation. Finally, the static deformed shape of the pressurized tire under a vertical load was modelled (Wang et al. 2012, Wang et al. 2014). Two-dimensional tire mesh and three-dimensional tire-pavement interaction models are shown in Figure 3.1 (a) and (b), respectively.

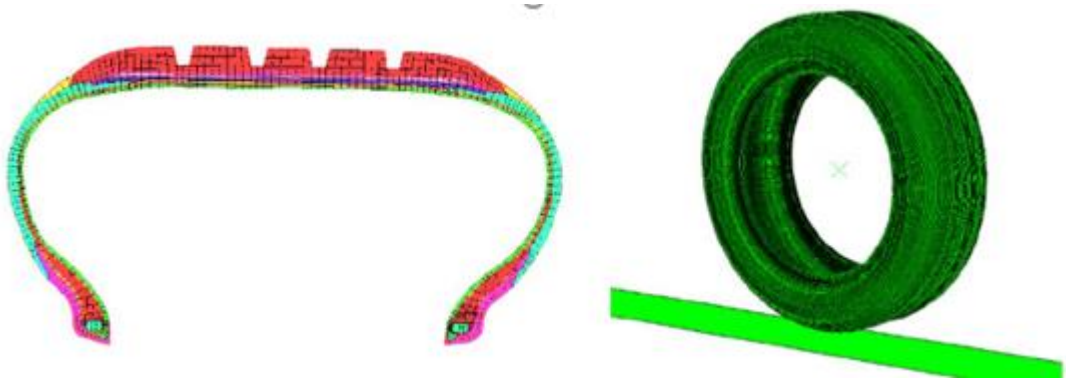

(a) (b)

Figure 3.1 (a) Two-dimensional and (b) three-dimensional tire-pavement interaction model

Modal analysis was conducted to identify the natural frequencies and mode shapes of the tire. The surface acceleration can be obtained from the modal characteristics of a tire. The eigenvalue problem for natural modes of small vibration using FEM is shown in Equation 3-1. Typically, for symmetric eigenproblems, $[K]$ is assumed positive semidefinite. In this case, u becomes an imaginary eigenvalue with $u = i\omega$ (where ω is the circular frequency) and the eigenvalue problem can be simplified (Equation 3-2).

$$\left(u^2[M]+u[C]+[K]\right)\{\phi\}=0 \tag{3-1}$$

$$\left(-\omega^2\left[M\right]+\left[K\right]\right)\{\varphi\}=0 \tag{3-2}$$

where,

$\left[M\right]$ is the mass matrix;

$\left[C\right]$ is the damping matrix;

$\left[K\right]$ is the stiffness matrix;

u is the eigenvalue;

$\{\phi\}$ is the eigenvector, the mode of vibration.

As discussed in Chapter 2, tire-pavement noise can be described as two mechanisms: the mechanical vibrations of the tire at the lower frequencies, and the aerodynamic phenomenon at the higher frequencies (Sandberg and Ejsmont 2002). The tire vibration noise was focused in this study because it is mostly related to pavement engineering application and human hearing sensitivity.

Steady state linear dynamic analysis predicts the linear response of a structure subjected to continuous harmonic excitation. The set of eigenmodes extracted in the previous eigenfrequency step were used to calculate the steady state solution as a function of frequency of the applied excitation. The structural dynamics equation for steady-state response under a harmonic excitation is shown in Equation 3-3. The acceleration response obtained in the FE analysis was used as a boundary condition for a BEM analysis of the transmitted noise field.

$$([K]+i\omega[C]-\omega^2[M]\{U\}=\{F\} \tag{3-3}$$

where,

{U} is the nodal displacement vector of structure;

[K] is the load vector of external excitation.

3.1.2 Tire-Pavement Noise Model with BEM

The mathematical formulations and practical applications of BEM have been discussed in detail in previous publications (Brebbia 1984; Shaw 1979; Copley 1967). The governing partial differential equation for linear acoustics in the frequency domain is the Helmholtz equation, as shown in Equation 3-4.

$$(\nabla^2 + k^2)p = 0 \tag{3-4}$$

where,

∇^2 is the Laplace operator;

p is the acoustic pressure;

$k = \omega/c$ is the wave number;

ω is the angular frequency;

c is the sound speed.

The boundary condition for vibro-acoustic problems is given in Equation 3-5.

$$\partial p/\partial n = -i\rho w v_n \tag{3-5}$$

where,

i is the imaginary unit;

ρ is the acoustic fluid density;

v_n is the normal velocity.

From the theory of Green's functions, Equation 3-4 can be recast into the Helmholtz integral for an exterior boundary value problem (Parlett 1989):

$$p(P) = \int_{\Gamma} \left(G \frac{\partial p}{\partial n} - p \frac{\partial G}{\partial n} \right) d\Gamma \tag{3-6}$$

where,

G is the singular fundamental solution;

Γ is the distance between the field point.

For a given acceleration field on the tire surface, an acoustic BEM direct frequency response analysis calculates pressure and normal acceleration values at all the boundary nodes and field points. The outer surface elements of the tire were selected to constitute the boundary element. To avoid sound leakage, additional elements were added to the rim. The boundary of the tire model in BEM is the same as the FE model of the tire, in this way the acceleration response of the tire could be transferred directly to the BEM.

In the field practice, the Close-Proximity Method (CPX) measures the noise emission from a standard passenger car tire when rolling over a road surface, as illustrated in Figure 3.2 (Schwanen 2007; ISO 2000). The five microphones in the CPX method are modeled with the corresponding five field points in BEM to calculate the sound pressure, as shown in Figure 3.3.

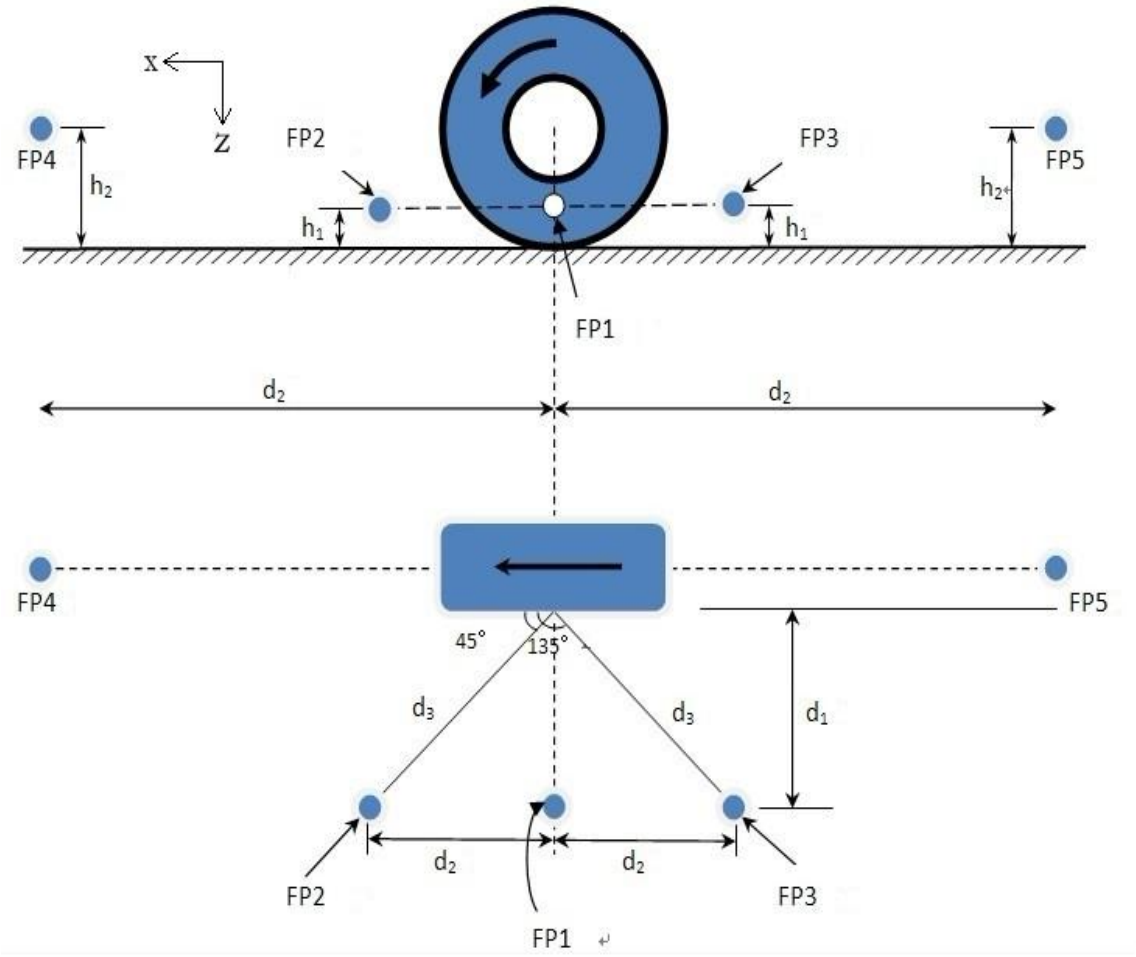

Figure 3.2 Boundary element model of tire-pavement interaction for noise prediction

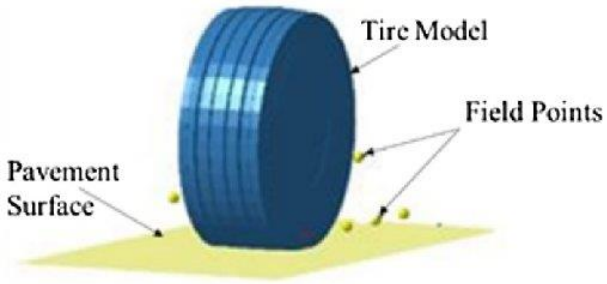

Figure 3.3 Boundary element model of tire-pavement system (CPX method)

3.2 Pavement Surface Characteristics

3.2.1 Pavement Surface Texture

Several thin-layer surfacing sections have been used in a study conducted in the Netherland to measure tire-pavement noise and analyze the influencing factors (such as surface characteristics and mixture type) (Li et al. 2013). Four pavement sections, including semi-dense surface layer (section 4), porous asphalt layers (sections 9, 15 and 24) were selected from the field-testing sections in the Netherland study to evaluate the effect of surface texture and sound absorption on tire-pavement noise. The asphalt mixture compositions and surface characteristics are shown in Table 3.1.

Table 3.1 Pavement Mixture Compositions and Surface Characteristics (Li 2013)

Section No.	**Max. Aggregate Size (mm)**	**Binder content (%)**	**Air void (%)**	**Thickness (mm)**	**Mean Texture Depth (MPD) (mm)**	**Max. Sound Absorption Coefficient**
4	6	7.5	12	25	0.71	0.35
9	8	6.0	>20	25	1.40	0.74
15	6	6.6	>20	25	0.75	0.70
24	8	6.0	>20	25	1.42	0.73

The profile of surface texture is described by the coordinate along the pavement surface plane, called distance (the “x” coordinate), and the coordinate in a direction normal to the surface plane, called amplitude (the “z” coordinate). The profile can be treated as a stationary, random function of the distance along the surface. Surface texture can be

represented by the texture level on wavelength spectrum. By means of Fourier transformation, the texture profile can be mathematically represented as an infinite series of sinusoidal components of various frequencies with given amplitude and initial phase. The profile level L_x at different frequencies is expressed in dB, as shown in Equation 3-7 (ISO 2002). In this study, third octave wavelength bands were considered. Figure 3.4 shows the texture level of four pavement sections that was used in the Netherlands study (Li 2013).

$$L_x = 20log_{10}(\frac{a_x}{a_{ref}}) \quad (3\text{-}7)$$

where,

L_x : profile level (dB);

a_x : profile root mean square (m);

a_{ref} : reference root mean square value ($a_{ref} = 10^{-6}m$);

x : subscript indicating a value obtained with a certain filter.

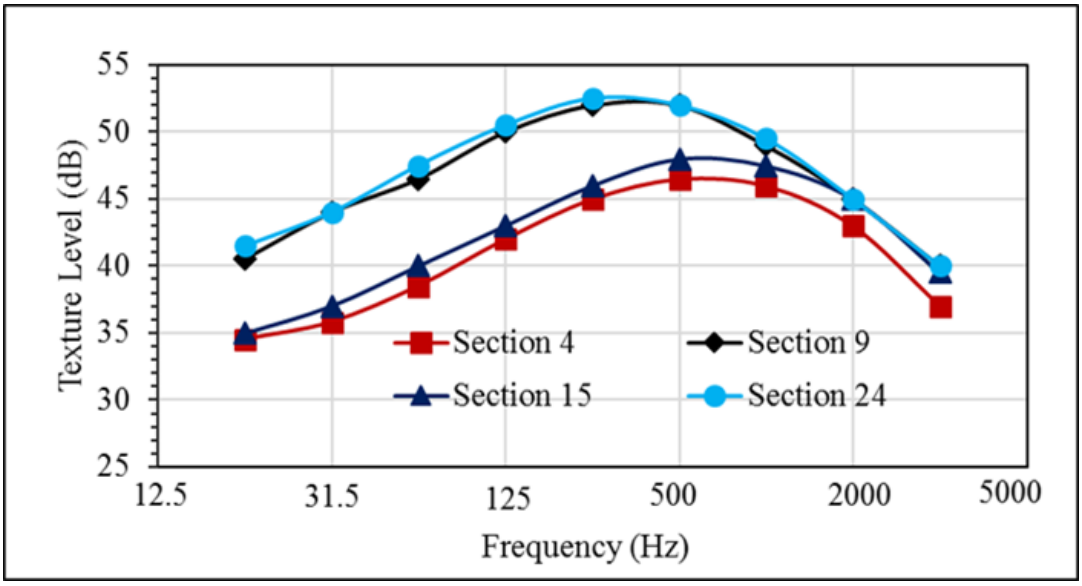

Figure 3.4 Pavement surface texture spectra for four pavement sections

Random response analysis was used to predict the tire responses subjected to a nondeterministic continuous excitation. The most widely used approach for random vibration analysis is using Power Spectral Density (PSD) functions to represent loading and response (Sun and Greenberg 2000; Sun 2003). In this study, to take into consideration of pavement texture excitation, PSD functions of texture profiles after Fourier transformation were used in tire-pavement interaction model. After the step of modal frequency analysis, the response of the system is used for random response analysis under excitation of surface texture spectrum in the contact patch.

3.2.2 Sound Absorption

Porous asphalt concrete has a typical density between 1,700 and 2,000 kg/m^3 (106 and 125 lb/ft^3) and is treated as rigid-framed porous material. By extending Kirchoff's theory for sound propagation in pores, Zwikker and Kosten (1949) derived expressions for

acoustic absorption of porous materials when air propagated in the pores with circular cross-sections, in which both thermal and viscous effects of wave propagation were considered.

In Zwikker and Kosten model, the macroscopic description of acoustic propagation and dissipation through a rigid-framed porous material can be considered as a layer of equivalent fluid with the frequency-dependent effective density (dependent on viscous interaction between the fluid and the frame) and compressibility (bulk modulus) (Allard 1993). The effective density depends on viscous interaction between the fluid and the frame; while the bulk modulus depends on thermal interaction. The Zwikker and Kosten model gives expressions for the effective density and the bulk modulus in Equations 3-8 and 3-9. The thermoelastic damping and viscous losses are significantly affected by the microstructure of porous material, such as porosity, shape, and size of pores, etc.

In the authors' previous work (Wang and Ding 2016), the Zwikker and Kosten model was implemented to investigate the influences of idealized pore structure parameters (porosity, pore radius, and pore length) on acoustic absorption and evaluate the optimum pore structure for achieving the maximum acoustic absorption capacity.

$$\rho(\omega) = \rho_0 \left[1 + \frac{1}{\sqrt{3^2 + \frac{4\omega\rho_0}{\sigma\phi}}} - j\frac{\sigma\phi}{\omega\rho_0}\sqrt{1 + \frac{\omega\rho_0}{4\sigma\phi}} \right] \tag{3-8}$$

$$K(\omega) = \frac{\gamma P_0}{\gamma - (\gamma - 1)(1 - \frac{Nu}{j8\omega\rho_0 \,\mathrm{Pr}/\sigma\phi + Nu})} \tag{3-9}$$

where,

σ is the air flow resistivity of porous material (a function of pore radius and porosity);

ϕ is the porosity;

P_r is Prandtl number;

γ is the ratio of specific heat;

Nu is Nusselt number;

$j^2 = -1$;

P_0 is air pressure;

ω is the angular frequency;

ρ_0 is air density.

The two key characteristics that describe acoustic behavior of a rigid-framed porous material are the complex wave number k and the characteristic acoustic impedance Z_c, as shown in Equations 3-10 and 3-11 (Allard 1993).

$$k = \sqrt{\frac{\rho(w)}{K(w)}} \tag{3-10}$$

$$Z_c = \sqrt{\rho(w)K(w)} \tag{3-11}$$

where,

ρ is the effective density;

K is bulk modulus of the air within the porous material.

The acoustic absorption coefficient for normal incidence (α) can be solved using Equation 3-12 (Allard 1993):

$$\alpha = 1 - \left| \frac{-jZ_c \cot kd - \phi Z_0}{-jZ_c \cot kd + \phi Z_0} \right|^2 \tag{3-12}$$

where,

Z_0 is characteristic impedance of air;

Z_c is characteristic acoustic impedance;

k is complex wave number of the porous material;

d is the thickness of thin layer surfacing (here it is assumed being equal to pore length);

ϕ is porosity.

Porous pavement is simulated by an absorbent panel where the acoustic impedance is defined to model sound absorption properties, whereas the non-porous surface is represented by a symmetry plane with total reflection. The sound absorption effect is achieved by adjusting each pore structure parameter (porosity, pore radius, and pore length) independently to fit the predicted maximum acoustic absorption and the frequency of the peak value with that of the measured values on four pavement sections. Once the peak absorption value and the frequency at which the peak values occur are fitted, the pore structure parameters are determined. Then, the frequency dependent sound velocity and mass density used for sound pressure calculation were deduced based on the corresponding pore structure parameters, which serve as the two input parameters for the absorbance panel in the BEM.

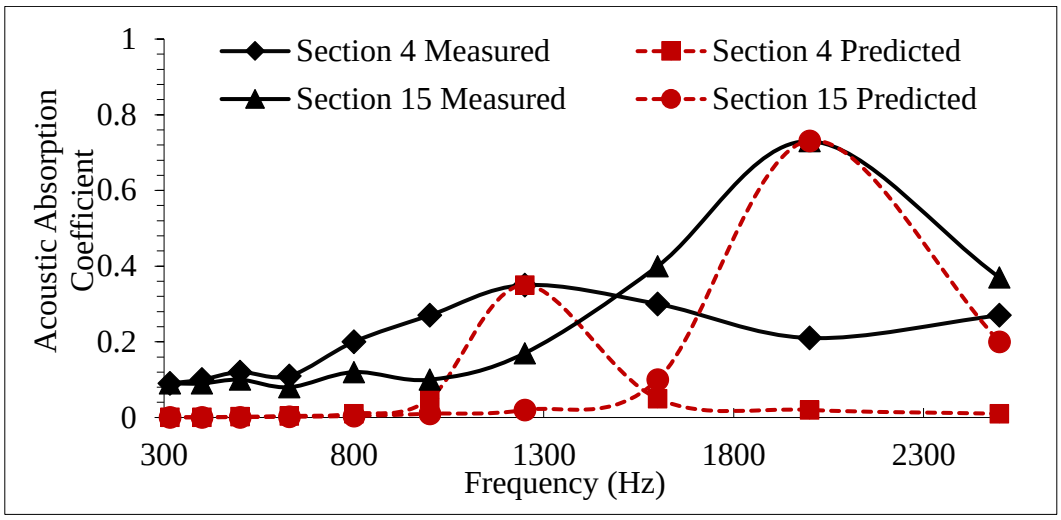

(a)

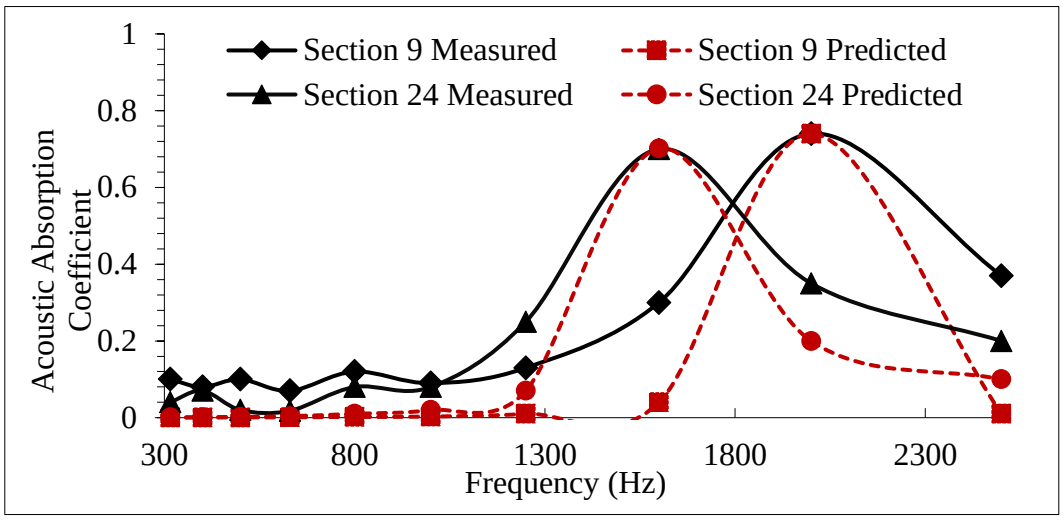

(b)

Figure 3.5 Acoustic absorption spectra for (a) sections 4 and 15; and (b) sections 9 and 24

Figure 3.5 compares the predicted and measured acoustic absorption spectra for four pavement sections. The measured data of acoustic absorption were extracted from the Netherlands study (Li 2013). As expected, there are large differences in the maximum sound absorption coefficients between non-porous and porous asphalt layers. It was found

that the first peak of sound absorption curve for section 4 was located between 1000 Hz and 1400 Hz, with the maximum absorption coefficient of around 0.35. For the sections 9, 15, and 24, the maximum sound absorption coefficient was found being greater than 0.7, and the corresponding peak frequency occurred between 1600 Hz and 2000 Hz.

3.3 Model Calibration and Validation

One effective procedure for calibrating the tire-pavement noise is to use an optimization process for scaling the tire mode shapes. The principal concept involved in this procedure is to find a set of scaling constants a_i for accordingly mode which minimize the difference between the simulated noise level and the measured data in the frequency range of interest (Anfosso-Lédée 2002). In this study, the noise measurements using the CPX method were extracted from the field study in the Netherlands (Li et al. 2014).

$$z = |L_s - L_m| \tag{3-13}$$

where,

L_s the simulated sound pressure level;

L_m the measured sound pressure level.

For each mode i, the mode shape vector $\{\emptyset_i\}$ is unique in shape, but not in amplitude. By scaling each mode with a scaling constant (a_i), the modal mass (m_i) can be interpreted as:

$$m_i = \frac{1}{a_i \omega_i} \tag{3-14}$$

where,

ω_i the natural frequency of mode i.

Model calibration was performed for pavements with low-texture and high-texture pavement sections, respectively. Figure 3.6 shows comparison between the calculated and measured sound pressure levels for sections 4 and 9, respectively. The selected frequency range of sound pressure is from 315 Hz to 2500 Hz, since noise at high frequency range are more likely to be generated from air pumping and frictional effect, other than from tire vibration due to texture excitation. The predicted noise level is in good agreement with the monitoring result, with all the error values being acceptable (±0.5 dB).

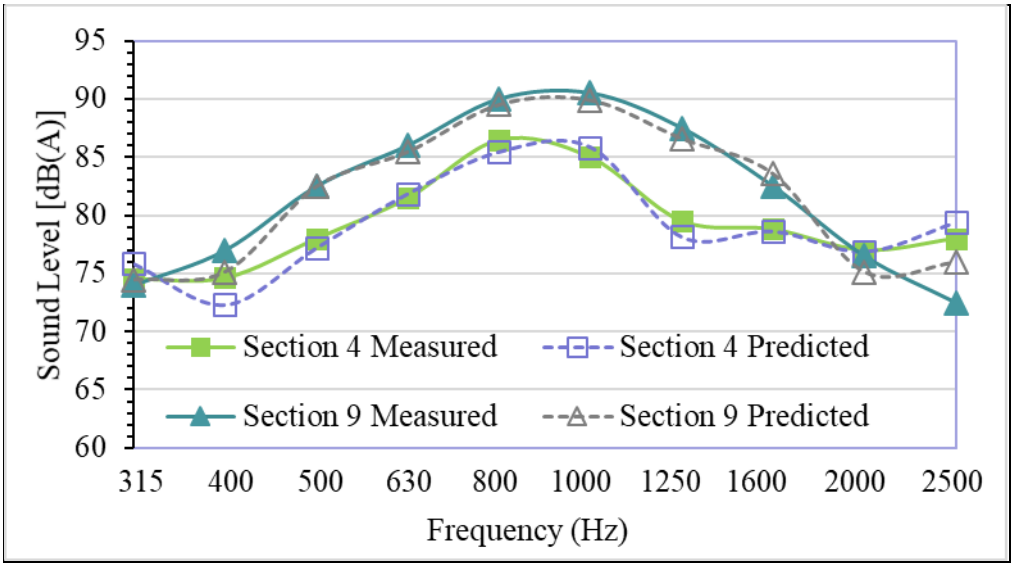

Figure 3.6 Comparisons of measured and predicted sound pressure levels for model calibration

After the model is calibrated, model validation was conducted for the other two sections. Figure 3.7 shows comparison between the calculated and measured sound pressure levels for sections 15 and 24, which have different texture levels but similar sound

absorption coefficients. It can be seen that the calculated and measured maximum sound pressure level and the corresponding frequencies show good agreements. The results show after the proper calibration, the proposed FEM-BEM model can predict the overall noise level considering the influence of both macro-texture and sound absorption characteristics of surface layer.

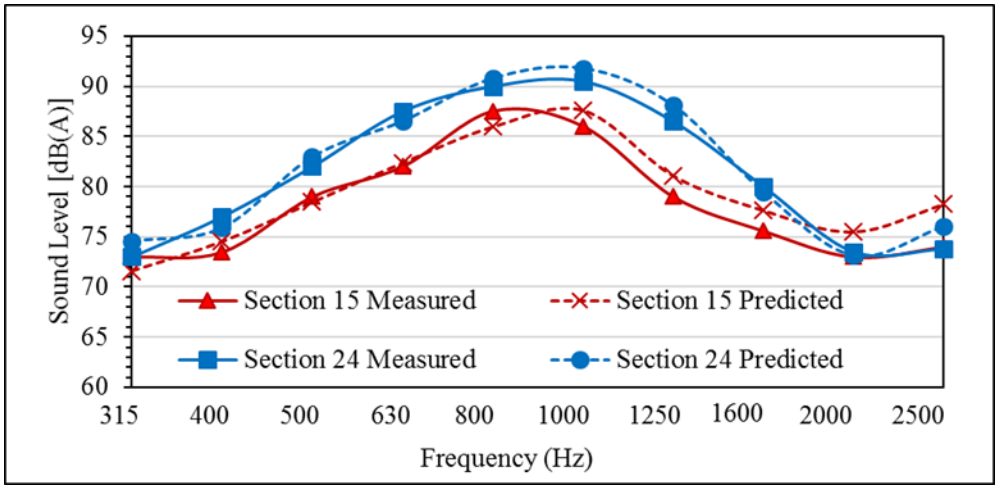

Figure 3.7 Comparisons of measured and predicted sound pressure levels for model validation

3. 4 Pavement Surface Characteristics Effects on Noise Level

3.4.1 Effects of Texture on Noise Level

To evaluate the effect of surface texture on tire-pavement noise level, four pavement sections with different texture levels but the same sound absorption spectra were selected. The texture levels of four sections (4, 9, 15, and 24) and the sound absorption spectra of section 9 were used in the analysis. The overall noise levels for the four sections with different textures levels are shown in Figure 3.8. It is apparent that the surface with highest

texture level is the nosiest while the surface with the lowest texture level is the quietest. The difference in overall noise levels can reach 2.6 dB(A) when the difference of MTD is around 0.7 mm. This is finding is consistent with field observations that the noise levels increase with the increasing of texture level (Aybike 2010).

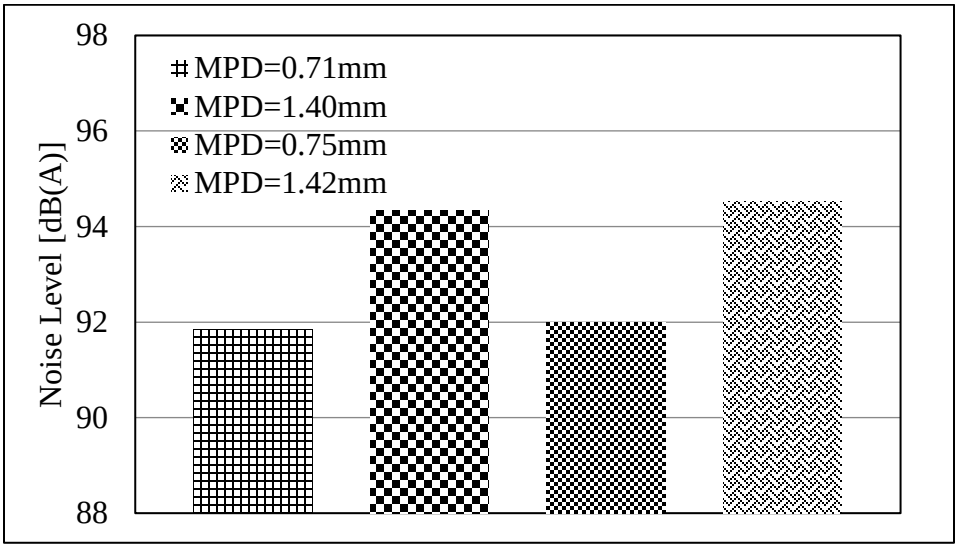

Figure 3.8 Effects of surface texture on overall noise level

3.4.2 Effect of Porosity on Noise Level

Figure 3.9 shows the variations of noise level for the porosity of 15% and 25%, respectively, on section 9 (high-texture) and section 15 (low-texture). It was found that the overall noise levels on section 15 were 86.9 dB(A) at 25% porosity and 88.8 dB(A) at 15% porosity; while the overall noise levels on section 9 were 89.3 dB(A) at 25% porosity and 91.0 dB(A) at 15% porosity. This indicates that the overall noise level decreases with the increase of porosity under the same texture level. However, the noise variation due to sound absorption performance of porous pavement is not as significant as the effect of surface texture on noise. The simulated results were compared with the field studies conducted in

Belgium (Descornet 2000). In their study, an equation was developed to quantify the influence of layer thickness and air voids on noise, as shown in Equation 3-15. The calculation results show that for a porous layer thickness of 25 mm, the increase of 15% to 25% in porosity would result in approximately 1.25 dB(A), which was consistent with the results obtained from the numerical model.

$$\Delta L = 0.005 * e * v \tag{3-15}$$

where,

ΔL is the difference of noise level in dB(A);

e is the thickness of surfacing layer (mm);

v is the air void.

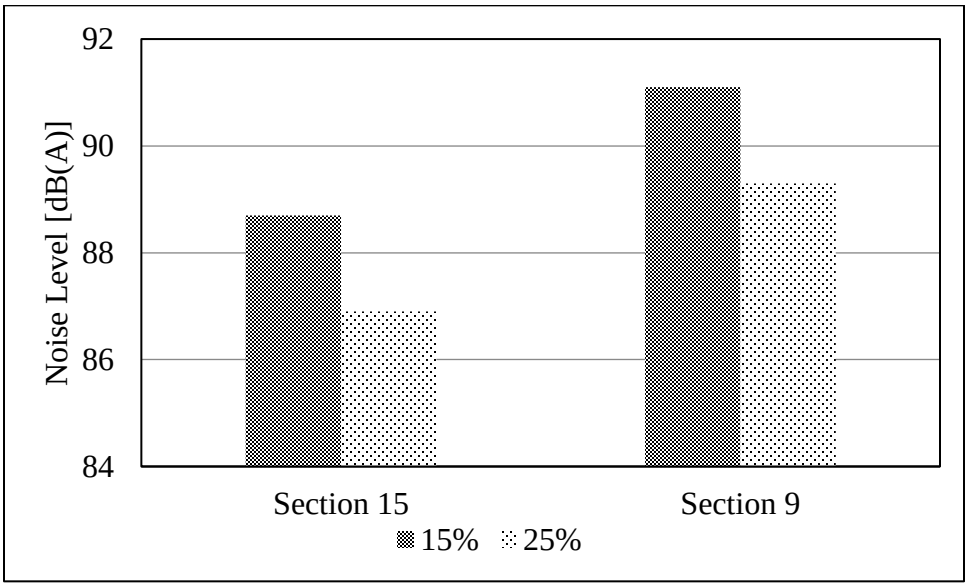

Figure 3.9 Overall noise level on porous surfaces with different porosities

3.4.3 Comparison between Porous and Non-porous Pavement Surface

To better understand the benefit of porous pavement, tire noise on non-porous and porous surfaces were compared. Four non-porous road surfaces were considered, which have the same texture levels as the four sections used in model calibration and validation. In the tire-pavement model with the non-porous surface, the injected sound wave is fully reflected on pavement surface and no sound absorption happens.

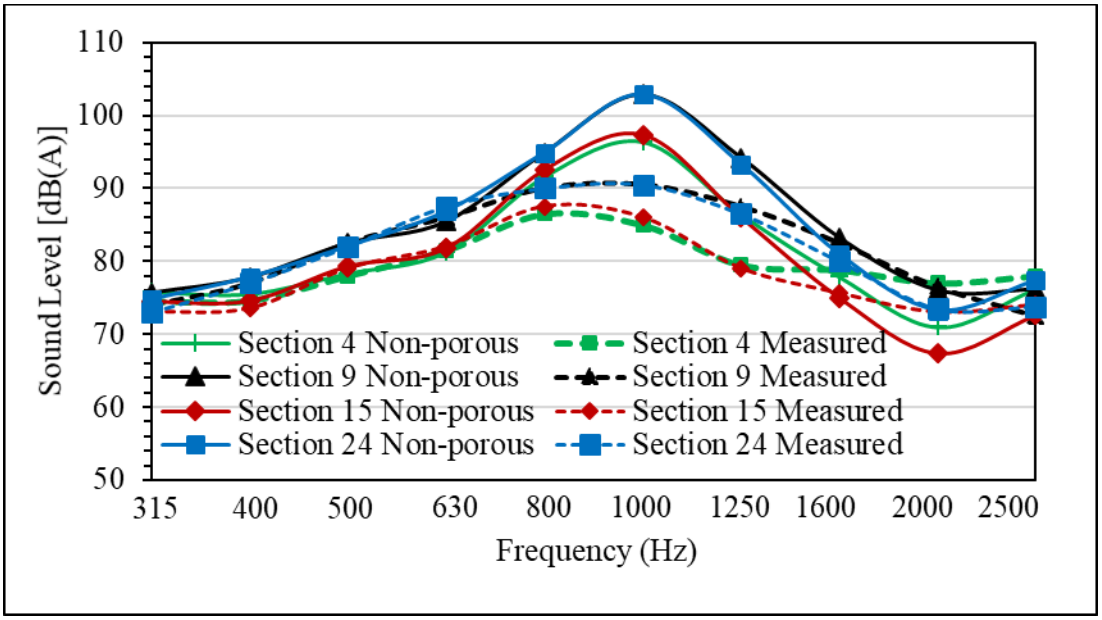

Figure 3.10 Comparisons of sound pressure levels between non-porous and porous pavement surfaces

Figure 3.10 compares the sound spectra between porous and non-porous surfaces. It can be seen that the benefit of noise reduction due to porous layer is from 7 dB(A) to 10 dB(A). Furthermore, the results also confirmed the finding from previous research that

porous pavement surface reduces tire/pavement interaction noise above 1000 Hz (Bernhard and Wayson 2005). The specific interpretation of the differences of the noise levels between porous and non-porous surfaces is mainly due to the sound absorption. The porosity effectively reduces the compression and expansion of air entrapped in tire-pavement interaction when tire rolls over the surface.

3.5 Summary

In this chapter, a passenger car tire (195/65R15) model was built and the vibrational noise level between tire and a non-deformable pavement surface was simulated. The radial tire model was built using the FEM and the tire surface accelerations under the excitation from pavement texture were obtained from modal analysis. The radiation sound fields caused by tire vibration were then solved using the BEM for noise prediction. Texture profiles and sound absorption of different pavement surface types were considered in the analysis for passenger car tire. The prediction results were calibrated and validated with the measurements reported in the literature.

The results show that with proper calibration and validation, the proposed numerical model can predict the overall noise level with the specific input of texture spectra and acoustic absorption spectra. In general, the surface type with higher texture levels usually generates higher noise level for both porous and non-porous surfaces. It was found that the overall noise level decreased with the increase of porosity under the same surface texture condition, although the noise variation due to porous pavement is not as significant as the effect of surface texture on noise.

CHAPTER 4 MODELING OF TIRE HYDROPLANING

4.1 Water Film on Permeable Friction Course

4.1.1 Mathematical Model of Sheet Flow

Sheet flow occurs when the subsurface of PFCs become saturated and runoff flow onto the pavement surface. Figure 4.1 presents the sketch of cross section along the flow path on roadway crown. The pavement has slope s, with the thickness of the PFC layer b in *cm*. The elevation of the bottom of the PFC layer with respect to a datum is $Z_0(x)$. The saturated thickness within PFC is $h_p(x)$, whereas the sheet flow depth on the surface is $h_s(x)$. The total head of water at any points is $H(x)$. In order to predict water film depths for hydroplaning simulation, the model proposed by Charbeneau and Barrett (Charbeneau and Barrett 2008) was used, as shown in Equation 4-1. The equation can be used to determine the sheet flow depth along the drainage length at any specific rainfall intensity, pavement slope, and hydraulic conductivity.

$$h_s(x) = \left[\frac{K_{DW} \nu (rx - Ts)}{8gs} \right]^{1/3} \tag{4-1}$$

where,

K_{DW} is the Darcy-Weisbach coefficient;

ν is the kinematic viscosity in cm^2/s;

r is rainfall intensity in *cm/h*;

T is transmissivity of PFC defined as $T = Kb$ in cm^2/s;

g is the acceleration due to gravity in cm/s^2;

K is hydraulic conductivity of PFC in *cm/s*;

x is measured from the roadway crown in *cm* (no-flow boundary);

s is slope.

Two critical steps are involved in using Equation 4-1 to estimate the sheet flow depth of PFC:

1) Determine the value of Darcy-Weisbach coefficient (also called Darcy friction factor) K_{DW}, which is a purely numerical factor dependent only on channel shape. For laminar flow in smooth channels, the value of K_{DW} is approximately 24 for rectangular channels (Chow 1959). However, for the flow in PFC, due to the roughness of PFCs and rainfall effect, the value of K_{DW} is much larger (Charbeneau and Barrett 2008). In this study, the recommended value (K_{DW}=900) used in Charbeneau and Barrett's model was used;

2) Determine the boundary of the upstream edge of PFC. Depending on the conditions near the upstream edge of PFC, the boundary can be no-flow boundary or drainage boundary. In the no-flow boundary, the origin of χ axis is roadway crown; whereas in the drainage boundary, the coordinate system in the sheet flow model of PFC is located at the drainage divide. In this study, no-flow boundary is used to calculate the maximum sheet flow depth along the drainage length.

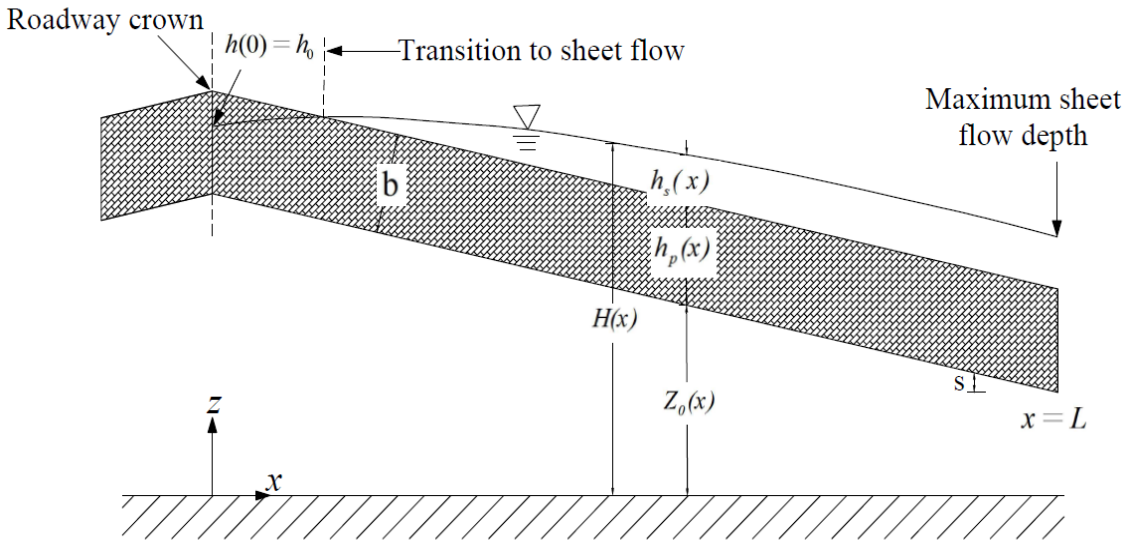

Figure 4.1 Cross section along flow path of PFC with no flow boundary

4.1.2 Water Film Depth on Different Traffic Lanes

Roadway geometry design deals with the number of traffic lanes, lane width, cross slope, and other roadway features. According to AASHTO guideline (2011), the cross slopes of 1.5% to 4% are recommended for public roadways in the United States. Most public roads have at least two lanes, one in each direction. For rural and urban arterials, typical lane widths may range from 3.05 to 3.66 m (10 to 12 ft) and the wider lanes should be used on roads with higher speed limits, higher traffic volumes, or significant numbers of trucks and other large vehicles. In this study, the lane width is assumed as 3.66 m (12 ft), and the inner and outer wheel path are defined as having the centerline 0.76 m (2.5 ft) away from the lane edges (Miller 2003). The typical thickness of PFCs falls in the range of 2-6 cm (1-2 in).

The water film depths along the drainage length were calculated under the following conditions: hydraulic conductivity of PFC $K = 1\ cm/s$, kinematic viscosity $v = 0.01 cm^2/s$, Darcy-Weisbach coefficient K_{DW} =900 (as recommended in Charbeneau and Barrett's model). The water film thickness is presented as a function of different road factors, as shown in Figure 4.2.

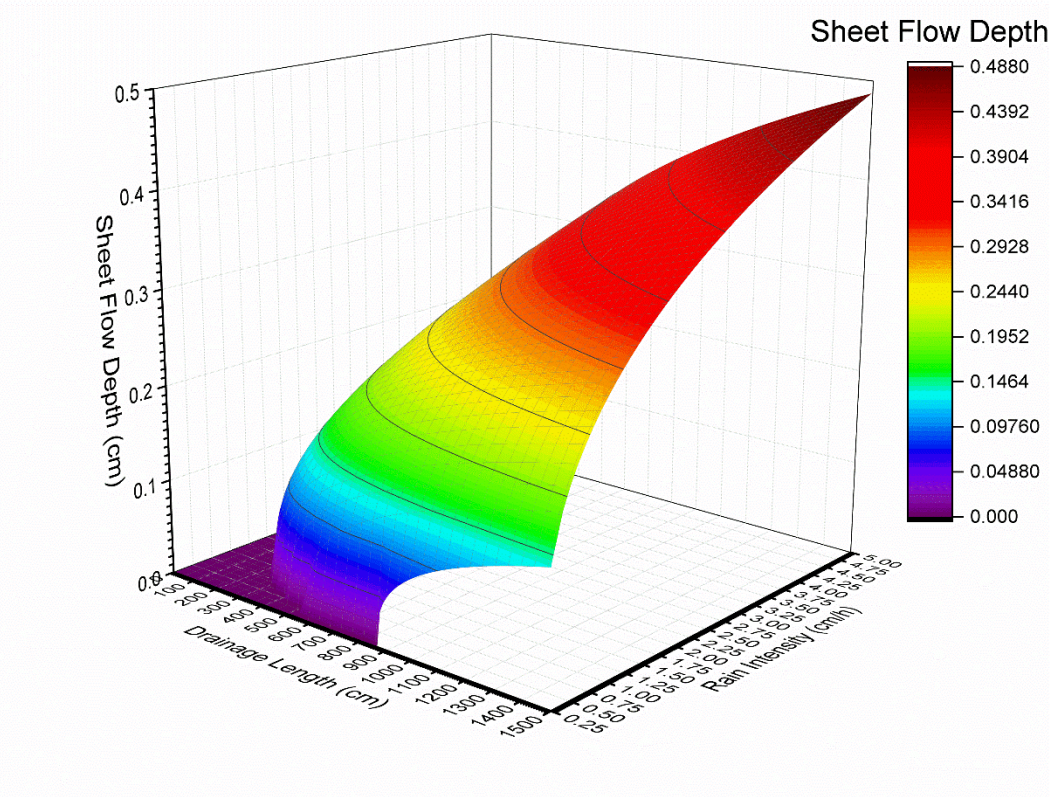

(a)

It is obvious from Figure 4.2(a) that the water flow depth increases along the drainage path. For example, at the rainfall rate of 1cm/h, there is no sheet flow on the first lane. However, there is about 2.6 mm water flow depth on the fourth lane. At the rainfall rate of

5 cm/h, the water flow depth on the first lane is around 2.8 mm; whereas the water flow depth on the fourth lane is about 4.8mm.

In addition, Figure 4.2(b) and (c) show that the water film depth on the road surface varies with the variation of cross slope and pavement thickness. The above analysis findings demonstrate that the hydroplaning risk on the same roadway may vary under different rain rates, or due to the change of cross slopes, such as on pavement sections with superelevation. Thus, it is necessary to study the effect of different roadway factors on hydroplaning potential.

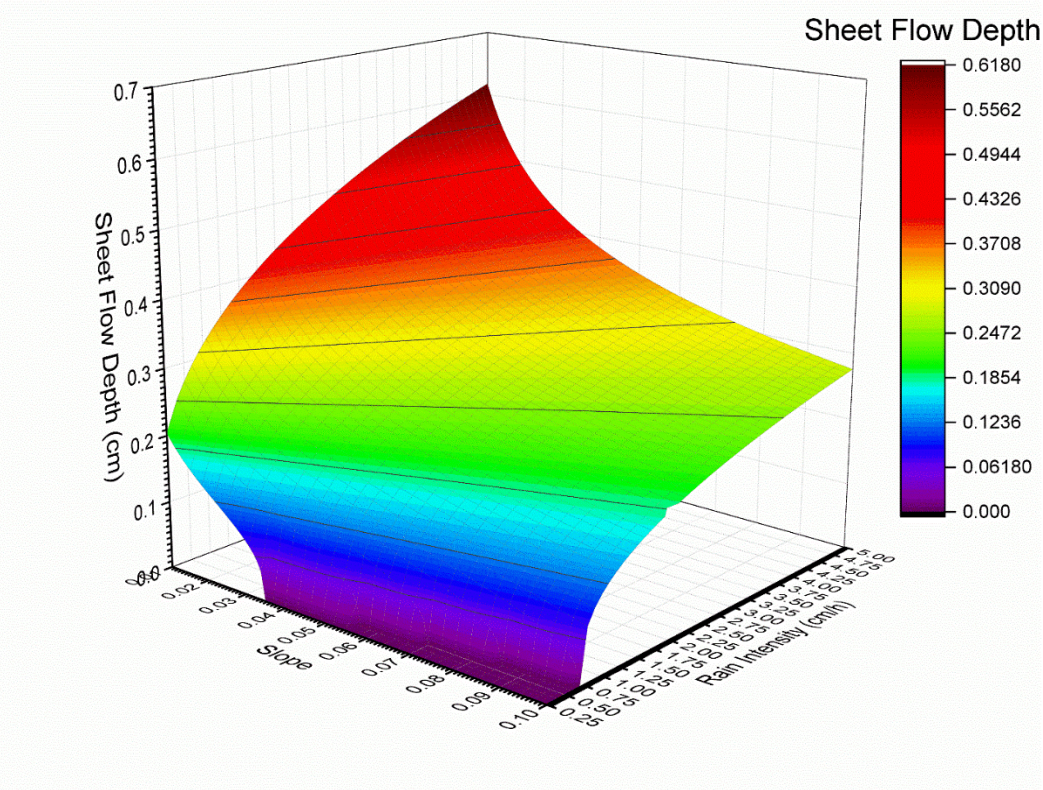

(b)

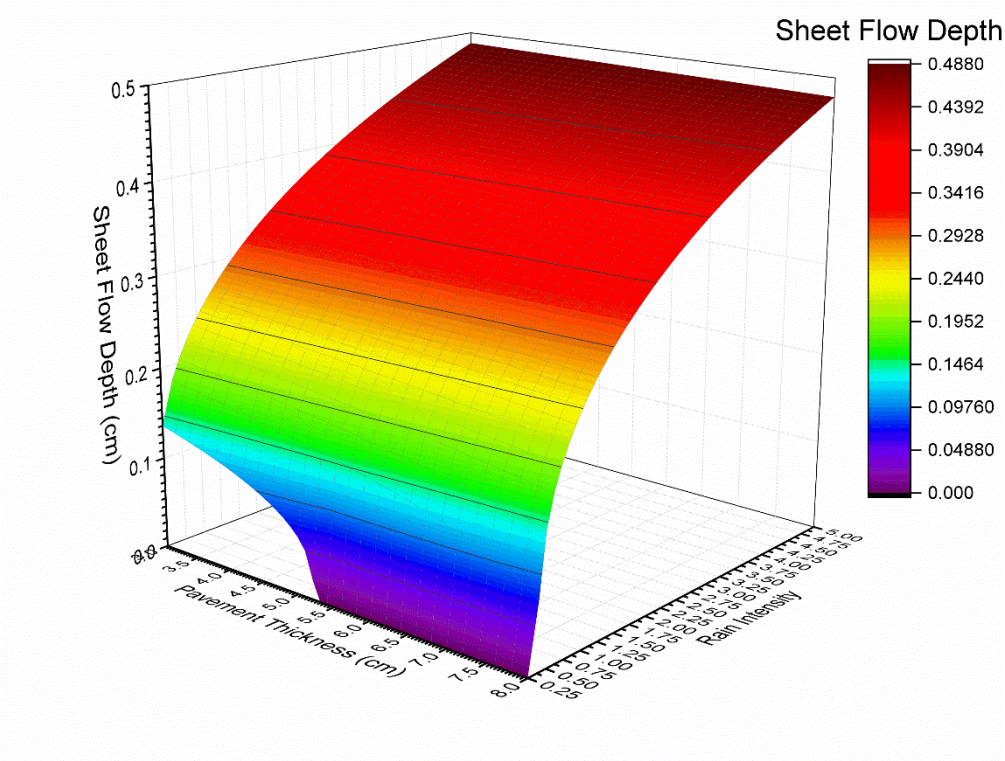

(c)

Figure 4.2 Water film thickness as a function of different roadway design factors (a) drainage length (2% cross slope, 5 cm PFC layer thickness); (b) cross slope (15 m drainage length, 5 cm PFC layer thickness*)*; and (c) PFC layer thickness (15 m drainage length, 2% cross slope)

4.2 Fluid-Structure Interaction Model

4.2.1 Hydroplaning Phenomenon

When a vehicle drives into thick water films at high speeds, the tire is subjected to pressure from the flowing fluid which causes deformation in the tire. As a return, the deformed tire alters the fluid field. The interaction between rolling tire and flowing fluid

repeats until the entire fluid-structure reaches steady state. This kind of interaction is called fluid-structure interaction. Depending on the reference frame, the tire mesh can move with the material or be fixed in space. The vertical load of tire is transferred to the fluid through the interaction between tire and fluid. As the load transfer goes on, part of water volume will flow into tire grooves; at the same time, due to the hydrodynamic pressure against the deformable tire structure, lift force arises and increase which will result in the penetration of water under the tire contact patch, therefore reducing contact area at tire-pavement interface. At a specified tire speed, the lift force reaches to a certain level, causing the tire to lose contact with the road surface, full dynamic hydroplaning occurs.

4.2.2 Tire Finite Element Model

A passenger car tire model P205/45R16 with four 9.9 *mm* wide grooves is considered for hydroplaning simulation. The tire has inflation pressure of 187 kPa and vertical load of 3,767 N. The choice of tire model parameters depends on balancing the type of behavior desired in the model with the information available. In the analysis of tire hydroplaning, the focus is on rainwater flow and global contact forces, not aiming at local tire deformation. The water flow and the resulting contact forces are more sensitive to the tread block geometry and the total kinetic energy of tire (Rugonyi 2001). In this case, the fiber-reinforced rubber part is modeled using solid rebar elements. The steel bead cords in underlying rubber matrix are modeled as elastic elements. The tread and sidewalls constructed from pure rubber are modeled by the Neo-Hookean model (Ding 2016).

The tire model was validated using the predicted tire deflections against the measurements from static loading test, as shown in Figure 4.3(a). As presented in Figure 4.3(b), the predicted tire deflections match well with the measured data. The simulated tire contact area was found within 5% error of the measured one. This indicates that the constructed tire model is suitable for finite element analysis.

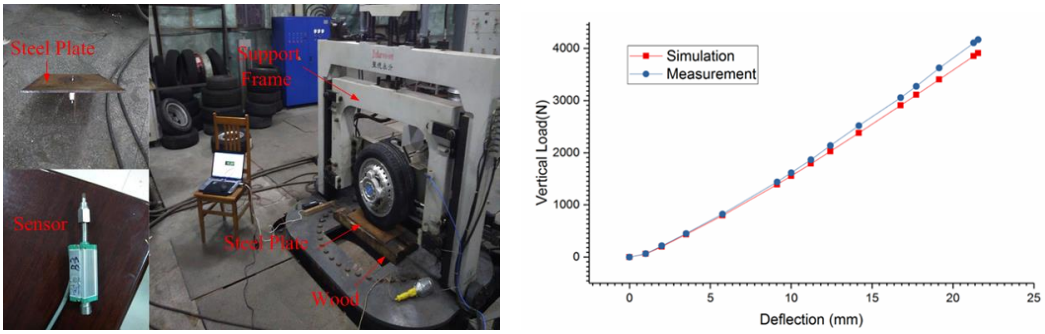

(a) (b)

Figure 4.3 Tire deflection test (a) test setup; and (b) calculated and measured tire deflections

The simulation of FE tire model includes five steps. In the first step, an internal inflation pressure is applied on the axisymmetric tire model. The second step is generation of 3-D wedges with tire structure and tread. The third step is generation of a 3-D full treaded tire. In the fourth step, the tire rim is mounted under inflation pressure. In the last step, the inflated tire reaches a stationary rolling condition under a vertical load at a constant travelling speed. The rolling tire is then imported to the non-stationary fluid-structure interaction model for hydroplaning analysis. Figure 4.4(a) presents the assembling process of grooved tire model.

4.2.3 Fluid Model

In this study, the Coupled Eulerian-Lagrangian (CEL) method is used to capture hydroplaning phenomenon. With CEL, the flowing fluid can be modeled effectively using Eulerian analysis and the tire structure can be treated using traditional nonlinear Lagrangian analyses. In the CEL method, material is tracked as it flows through the mesh by computing its Eulerian volume fraction within each element (Rugonyi 2001; ABAQUS 2010). In the current study, the volume fraction $F(x;t) \in [0,1]$ of water is used to track the flow boundary,

$$\frac{\partial F}{\partial t} + V \cdot \nabla F = 0 \tag{4-2}$$

By definition, if the element is fully filled with water, its volume fraction $F = 1$; if no water is present in an element, then the volume fraction $F = 0$. In the simulation of tire hydroplaning, both water and air voids are treated as Eulerian elements. If the sum of all material volume fractions in an element is less than one, i.e. $0 < F < 1$, the air void will automatically fill the remainder of the element.

The Eulerian mesh of fluid (water and air) is presented in Figure 4.4(b). The dimension of fluid domain should be large enough to enclose the entire trajectory of interest, for example, the tire contact patch. In this study, the fluid domain has a width of 300 *mm*, length of 320 *mm*, and the depth of air space above water film is fixed at 50 *mm*.

4.2.4 Hydroplaning Model

Modern cars are equipped with anti-lock braking (ABS) to prevent tire from locking

up and skidding on the roadway. The concept of ABS is such that during braking, each tire continues to turn, thus reaching maximum braking force. Full braking or traction occurs when all the contact points at the tire contact patch are slipping. When hydroplaning occurs, a tire equipped with ABS will continue to rotate with an angular velocity. In this study, the ABS is realized by applying an exponential decay friction model with a slip ratio of 18% at a given angular velocity (Wang et al. 2014, Zhou et al. 2015).

In the analysis, water is treated as incompressible, isotropic, and Newtonian fluid with a constant viscosity. The only body force considered in the simulation is gravity and the temperature change of fluid and its influence on tire is negligible. The hydroplaning analysis is conducted in a moving frame of reference, in which the water and road surface are moving toward the tire structure at a given speed, and the tire rolls at a fixed location with angular velocity. Figure 4.4(c) shows the fluid-structure interaction model for hydroplaning simulation.

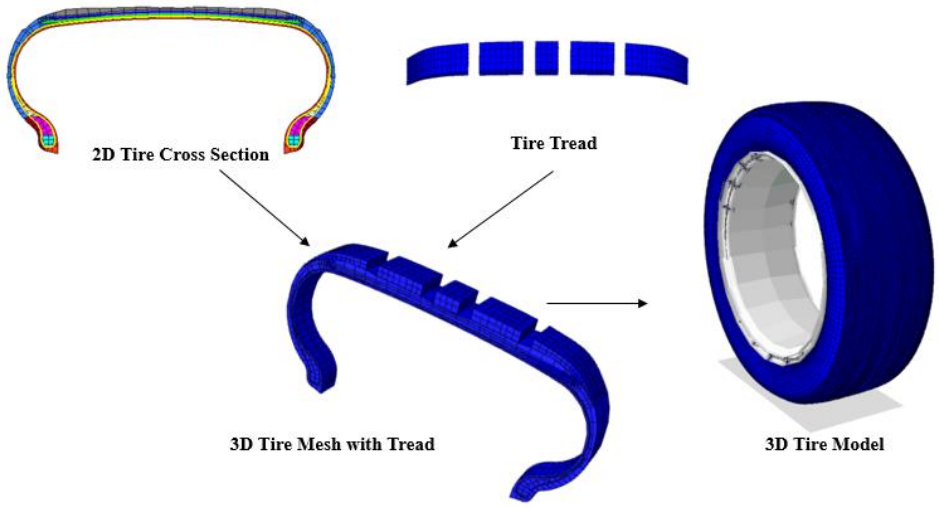

(a)

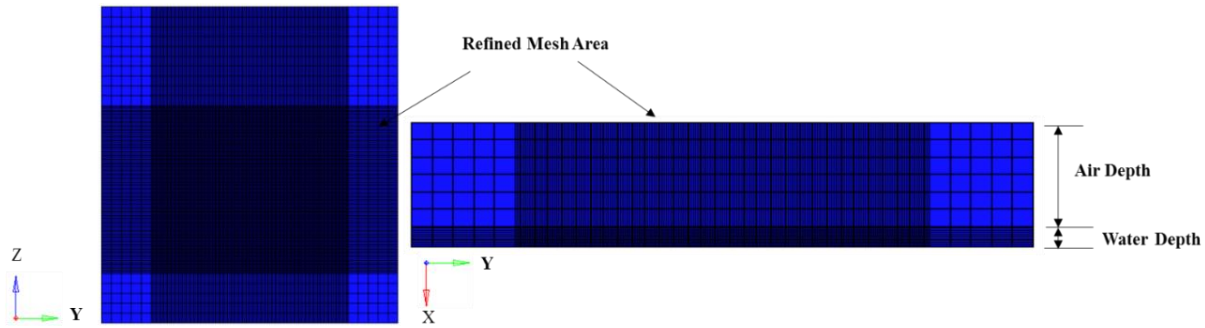

(b)

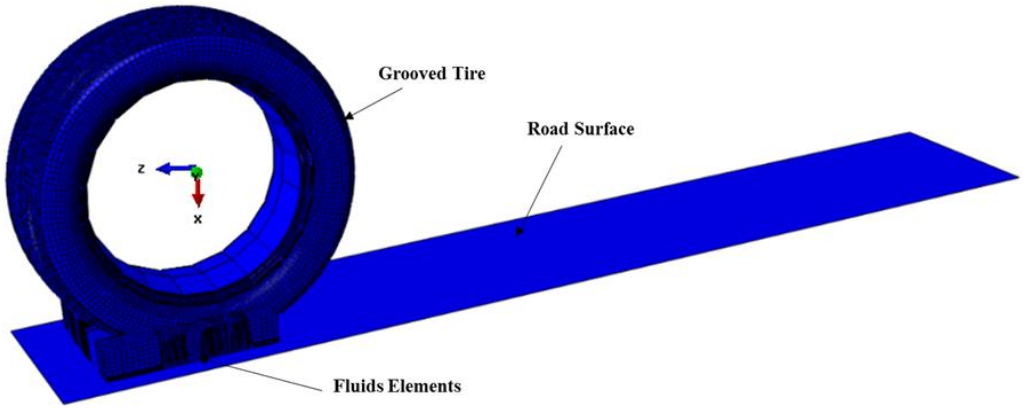

(c)

Figure 4.4 Illustration of (a) 3-D grooved tire model; (b) fluid model; and (c) Fluid-structure interaction model for hydroplaning analysis

Figure 4.5 shows the contour plots of tire contact patches at hydroplaning speed of 72 km/h on water film depth of 10 *mm*. The EVF_WATER shown in the plot denotes the volume fraction for water, where the areas occupied by water (EVF=1) appear as a uniform color form the top of contour spectrum, while the areas unoccupied by water presents as a different color from the bottom of contour spectrum. The boundary of water appears in a range of colors as EVF transitions from one to zero. The white area in Figure 4.5 indicates the contact patch of tire ribs at tire-pavement interface. At t=0, the tire has full contact with

road surface. At t=0.008 *s*, when rainwater interacts with the tire, water begins to occupy the tire contact patch. The contact patch gets smaller as water flow into tire grooves and becomes prominent. At t =0.01 *s*, rainwater starts to drain from the left and right sides of tire in addition to drain through the grooves. As time goes on, at a certain time (t=0.03 *s*), the hydrodynamic force reaches to a certain level which is high enough to lift up the tire, and the tire loses contact with road surface.

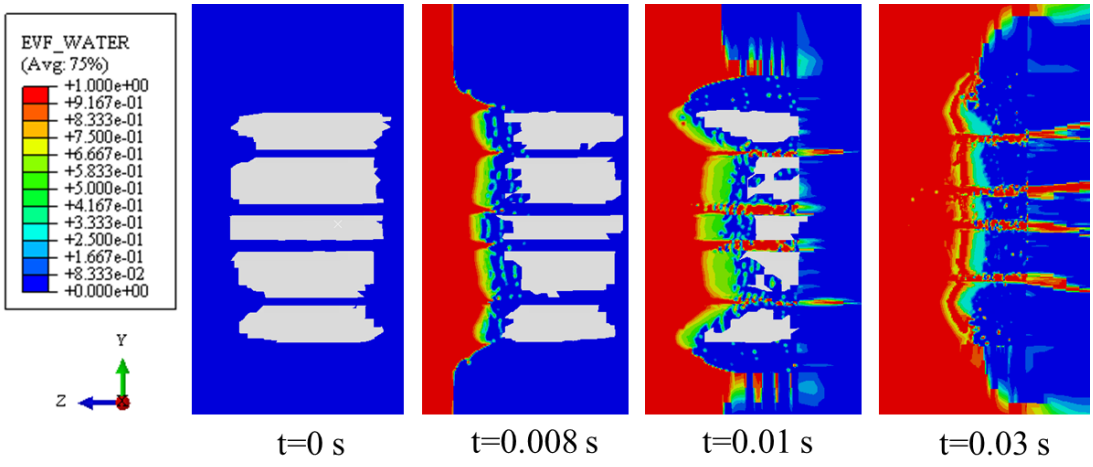

Figure 4.5 Evolution of water penetration into tire contact patch with time

4.2.5 Model Validation

There are many empirical equations that have been developed to predict hydroplaning speed. However, these existing empirical models are often limited to a certain type of tire or water film depth. For example, the NASA equation does not take into account of water film depth (Horne 1963). The Gallaway equations are based on specific tire profiles (Gallaway 1971, 1979). To validate the hydroplaning model proposed in this study, the predicted hydroplaning speeds were compared to the analytical results from previous work

and experimental measurements reported in the literature.

To validate the numerical method of hydroplaning, the predicted hydroplaning speeds of 195/65R15 tires were compared with experimental data measured in the study of Okano and Koishi (2001). Three different tread patterns of 195/65R15 tires were considered in the analysis, including smooth tread (no groove), narrow groove (groove width is 9 mm), and wide groove (groove width is 18 mm). The groove depth is 8mm and groove spacing is 50 mm. The vertical load applied on the tire is 4 kN and the tire inflation pressure is 200 kPa.

Table 4.1 Comparison of Hydroplaning Speeds with Experiment

Tire Model	Hydroplaning Speed (km/h)		Difference (%)
	Experiment (Koishi 2001)	Current Simulation	
Smooth tire (no grooves)	77.0	75.6	-1.8
9-mm groove width	82.6	80.0	-3.1
18-mm groove width	87.0	85.0	-2.3

Table 4.2 Comparison of Hydroplaning Speeds with Previous Model

Water Film Depth (mm)	Hydroplaning Speed (km/h)		Difference (%)
	Previous work (Oh, 2008)	Current Simulation	
5	82.2	85.5	4
10	70.3	72.0	2.8
15	65.2	68.0	4.3
20	62.2	63.7	2.4

The water film depth is kept at 10 mm. In the experiment, the hydroplaning phenomenon were captured by the visual images of water flow around the contact area when tires run on a water film. The comparisons of hydroplaning speeds obtained from the developed models and experimental measurements were summarized in Table 4.1.

To validate the hydroplaning model, the comparisons of hydroplaning speeds obtained

from the developed model and previous work are summarized in Table 4.2. A good agreement is observed between the predicted hydroplaning speed from the proposed model and the prediction from previous work. The validations indicate the proposed fluid-structure interaction model properly captures the hydroplaning phenomenon.

4.3 Hydroplaning Risk Analysis

4.3.1 Hydroplaning Risk on Different Traffic Lanes

This subsection evaluates the hydroplaning risk of each traffic lane under different rainfall intensities. The maximum water film depths along drainage length is calculated under the following conditions: slope $s = 0.02$, thickness of PFC $b = 3$ cm, hydraulic conductivity of PFC $K = 1$ *cm/s*, and kinematic viscosity $\nu = 0.01$ cm^2/s. The hydroplaning simulations were performed for 205/45R16 tire with a constant inflation pressure of 187 kPa and a vertical load of 3,767 N.

Table 4.3 Maximum Sheet Flow Depths (mm) at Different Lanes

Rain rate (cm/h)	**Type**	**2 Lanes**	**4 Lanes**		**6 Lanes**			**8 Lanes**			
			1st	2nd	1st	2nd	3rd	1st	2nd	3rd	4th
Light Rain <0.25	Impervious	1.1	1.1	1.4	1.1	1.4	1.6	1.1	1.4	1.6	1.8
	Permeable	-	-	-	-	-	0.9	-	-	0.9	1.3
Moderate Rain 0.25-1	Impervious	1.7	1.7	2.2	1.7	2.2	2.6	1.7	2.2	2.6	2.9
	Permeable	1.2	1.2	2.0	1.2	2.0	2.4	1.2	2.0	2.4	2.7
Heavy Rain 1-5	Impervious	3.0	3.0	3.8	3.0	3.8	4.4	3.0	3.8	4.4	4.9
	Permeable	2.8	2.8	3.7	2.8	3.7	4.3	2.8	3.7	4.3	4.8

From the maximum water depth presented in Table 4.3, the hydroplaning speeds under

different water depths can be computed by the developed fluid-structure interaction model. Figure 4.6 compares the hydroplaning speeds at different traffic lanes on permeable pavements. It is can be seen that since water film depth increases with drainage length along the traffic lane under a given rainfall rate, the hydroplaning risk increases with the increase of lane numbers. For example, under light rain rate, the runoff enters the pores of PFC, and there is no sheet flow on the cross sections with 2 lanes and 4 lanes. However, there is still hydroplaning potential on the 3rd lane and 4th lane on the cross sections with 6 lanes and 8 lanes. In addition, it is obvious that the hydroplaning risk increases with the increase of rainfall intensity. At light to moderate rainfall intensities, the hydroplaning risk for a 2-lane cross section is relatively low, however, at heavy rainfall intensity, the hydroplaning risk increases dramatically, especially for roadway cross sections with a greater number of lanes.

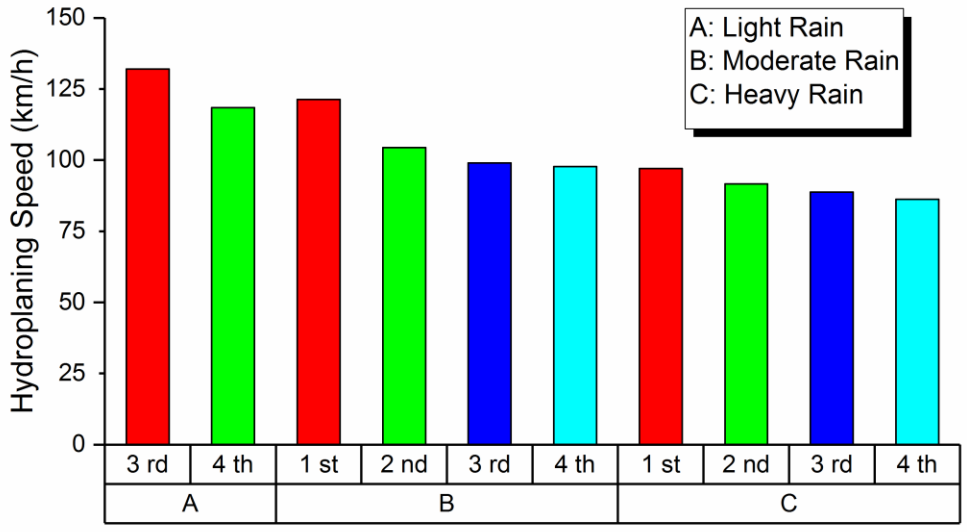

Figure 4.6 Hydroplaning speeds at each traffic lane under different rain rates

The results show that PFC provides better road safety for 2-lane and 4-lane cross sections at the same rain rates. The simulation results provide significant safe driving guidance for both drivers and transportation agencies. For example, during wet weather, it is advised for the drivers to travel at the innermost lane and avoid frequent changing of traffic lanes, especially driving from an inner lane to an outer lane which will increase the risk of hydroplaning. For transportation agencies, the roadway locations prone to hydroplaning can be treated with reduced speed limits and slippery pavement warning signs as low-cost interim counterplans to improve road safety. For example, at light rain rate, roadways with 8 lanes should be operated at speeds no higher than 118 km/h; but the same roadway should be operated at speeds no high than 97 km/h and 86 km/h, respectively, during moderate rain and heavy rain rates.

4.3.2 Comparison between Permeable and Impervious Pavements

This section compares hydroplaning risk between permeable and impervious asphalt pavements. For conventional impervious asphalt pavement, the hydraulic conductivity ranges from 8.5×10^{-7} to 10^{-4} *cm/s* (Kanitpong 2003). In this paper, the hydraulic conductivity of 5.04×10^{-5} *cm/s* is assumed for impervious asphalt pavement. The maximum sheet flow depths at different lanes for permeable and impervious asphalt pavements were also compared in Table 4.3.

Table 4.4 shows the comparison of critical hydroplaning speeds at different rain rates for permeable and impervious pavements at 8-lane roadway cross section. The model results show that PFC layer has reduced potential for hydroplaning during light rain and

moderate rain conditions as compared to impervious pavement surface, especially at the inner most traffic lane. For example, at light rain rate, there is no sheet flow on the first two lanes for an 8-lane cross section, however, the sheet flow on impervious pavement surface still has hydroplaning potential; at moderate rain rate, the hydroplaning speed for the inner most lane is 121 km/h, which is 11% higher than that on impervious pavement surface. However, it is worth noting that the anti-hydroplaning potential of PFC is not significant at heavy rain event, showing that in areas with frequent heavy rain rate, caution is still needed for drivers travelling on PFC.

Table 4.4 Hydroplaning Speeds for Permeable and Impervious Pavements at 8-Lane Roadway Cross Section

Rain rate (cm/h)		**Permeable**	**Impervious**
		Hydroplaning Speed Range (km/h)	
Light Rain	<0.25	≤118	≤107
Moderate Rain	0.25-1	98~121	96~109
Heavy Rain	1-5	86~97	86~95

4.4 Incorporating Hydroplaning Risk Consideration in Roadway Design and Maintenance

4.4.1 Effects of PFC Thickness on Hydroplaning Risk

This section evaluates the effect of PFC layer thickness on hydroplaning risk under different rainfall intensities. The maximum water film depths on the cross section with eight-lanes were calculated under the following conditions: slope $s = 0.02$, hydraulic

conductivity of PFC K=1 *cm/s*, and kinematic viscosity $v = 0.01$ cm^2/s. As presented in Table 4.5, the effect of PFC layer thickness on water film depth was within a certain range and its influence was affected by the rain rate. At light rain, the increase of PFC layer thickness could effectively reduce the water flow depth on pavement surface. However, when the PFC layer thickness increased beyond 5 cm, the PFC layer thickness had little contribution to the surface water drainage.

Table 4.5 Maximum Sheet Flow Depths (mm) on 4th Lane

Rain rate (cm/h)	**Thickness (cm)**					
	3	4	5	6	7	8
Light Rain (<0.25)	1.3	1.0	-	-	-	-
Moderate Rain (0.25-1)	2.8	2.6	2.6	2.5	2.4	2.4
Heavy Rain (1-5)	4.8	4.8	4.8	4.7	4.7	4.7

Figure 4.7 shows the effect of PFC layer thickness on hydroplaning speed under different rain rates. It shows that the PFCs with the thickness range of 2-4 cm can provide safe driving in light rain condition. In moderate and heavy rain conditions, the thickness of PFCs has little effect on hydroplaning risk. Thus, it is not recommended to increase the layer thickness of PFC at this case for the purpose of reducing hydroplaning risk. However, under such circumstances, the roadway locations prone to hydroplaning can be treated with reduced speed limits and warning signs of slippery pavement as low-cost interim counterplans to improve road safety. For example, at light rain, the roadways with eight lanes with PFC thickness of 3 to 4 cm can be operated at the speeds not higher than 118

km/h; but the same roadway should be operated at the speeds not higher than 97 km/h and 86 km/h, respectively, during moderate rain and heavy rain conditions.

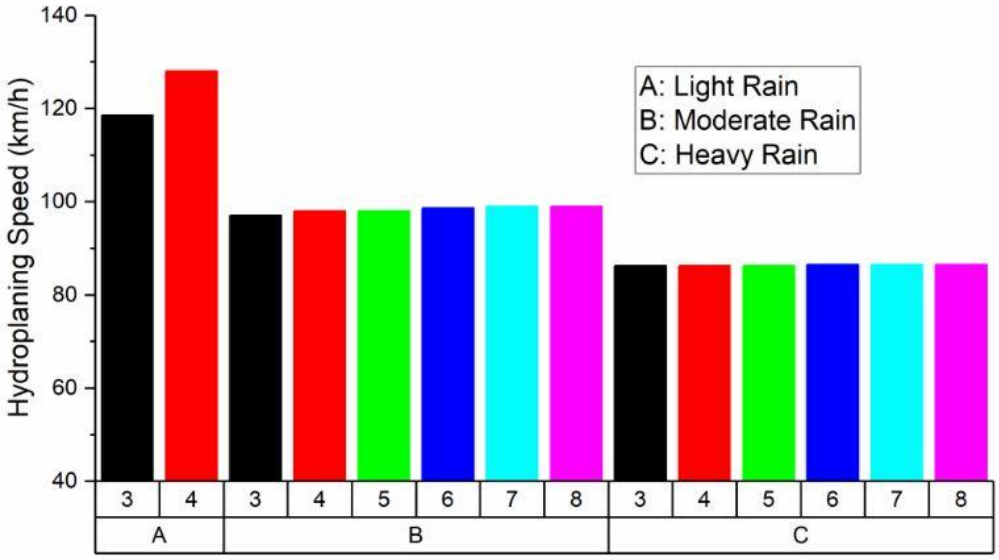

Figure 4.7 Hydroplaning speeds at different pavement thickness under different rain rates

4.4.2 Effect of Hydraulic Conductivity of PFC on Hydroplaning

The PFCs on road surface need be permeable enough to provide subsurface drainage. Previous studies have reported the influence of aggregate sizes, and binder material type and porosity on hydraulic conductivity of PFCs (Praticò 2007; Ball 2008; Putman 2012). Laboratory studies have shown that the higher air void content usually created the higher permeability. The hydraulic conductivity of PFC is typically between 0.2 and 0.8 cm/s but can also reach 2.1 cm/s at high voids (Fwa et al. 2015). In order to analyze the effect of hydraulic conductivity on hydroplaning risk, the following conditions were given in this section. The maximum water film depths on the cross section with eight lanes were calculated under the following conditions: slope $s = 0.02$, thickness of PFC $b = 5$ *cm*, and

kinematic viscosity $v = 0.01\ cm^2/s$. Table 4.6 presents the maximum water flow depth on eight lanes with various values of hydraulic conductivity for PFCs.

The results suggest that the increase of hydraulic conductivity has positive effect on the reduction of water flow depth on road surface. For example, in light rain condition, the corresponding water film depth was 1.7 mm when the hydraulic conductivity of PFC was 0.2 *cm/s*. However, at the same rain rate, when the hydraulic conductivity increased to 0.8 cm/s, the water film depth decreased by 41%. When the hydraulic conductivity increased to 1.0 cm/s, there was no water accumulation on road surface. Similar to the effect of pavement thickness, the positive effect of hydraulic conductivity on the reduction of water film depth decreased in moderate to heavy rain conditions.

Table 4.6 Maximum Sheet Flow Depths (mm) on 4th Lane

Rain rate (cm/h)	**Hydraulic Conductivity (cm/s)**					
	0.2	0.4	0.6	0.8	1.0	1.2
Light Rain (<0.25)	1.7	1.5	1.3	1.0	-	-
Moderate Rain (0.25-1)	2.8	2.7	2.7	2.6	2.6	2.5
Heavy Rain (1-5)	4.8	4.8	4.8	4.8	4.8	4.7

In Figure 4.8, the hydroplaning speeds on PFC layers with different values of hydraulic conductivity at different rain rates are presented for the roadway with eight lanes. The hydroplaning speed increases with the increase of hydraulic conductivity under light rain. This suggests that the hydraulic conductivity plays a significant role in road safety during light rain condition. For example, when the hydraulic conductivity decreased from 0.8 cm/s to 0.2 cm/s, the hydroplaning speed decreased by 15%, from 128 km/h to 109 km/h.

Therefore, the lower limit of hydraulic conductivity should not below 1.0cm/s to prevent hydroplaning under light rain rate. While under moderate rain to heavy rain rates, hydroplaning speed was not affected by the PFC layer properties (layer thickness and hydraulic conductivity). Therefore, speed control should be implemented for road safety. At these scenarios, drivers are advised to drive below 80km/h to avoid hydroplaning.

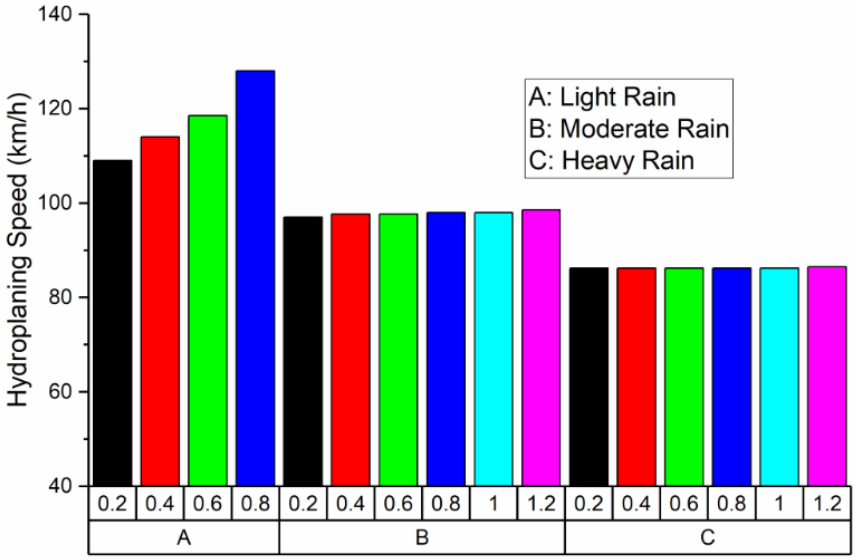

Figure 4.8 Hydroplaning speeds at various hydraulic conductivity under different rain rates

4.4.3 Effect of Pore Clogging on Hydroplaning Risk

As discussed previously, one of the main concerns about the use of PFCs is the reduction of drainage capacity due to the progressive clogging, including deformation-related clogging and particle related clogging. Deformation-related clogging results from the reduction in air void content of PFCs due to the accumulation of permanent rutting deformation (Hamzah et al. 2012; Coleri et al. 2013); while particle-related clogging occurs

when the air voids are clogged by dirt and pollutants (Suresha 2010). Previous researches have investigated the anisotropy of permeability in horizontal and vertical directions and measured the permeability loss due to deformation-related clogging and particle-related clogging under different load levels and cycles (Chen et al. 2015; 2017). Their studies found the average permeability loss due to deformation-related clogging was from 16% to 48% when the loading time increased from 10 min (420 cycles) to 60 min (2520 cycles) with the loading pressure of 700 kPa (60 ºC). The permeability loss due to particle-related clogging was from 10% to 41% after 1-6 clogging cycles (application of suspension including 500 g liquid and 5 g fine particles at one cycle).

Table 4.7 Water Flow Depths (mm) on 4th Lane after Deformation-Related Clogging

Rain rate (cm/h)	**Rutting Test Cycles**						
	0	420	840	1260	1680	2100	2520
Light Rain (<0.25)	-	1.0	1.2	1.3	1.3	1.4	1.4
Moderate Rain (0.25-1)	2.5	2.6	2.7	2.7	2.7	2.7	2.7
Heavy Rain (1-5)	4.7	4.8	4.8	4.8	4.8	4.8	4.8

Table 4.8 Water Flow Depths (mm) on 4th Lane after Particle-Related Clogging

Rain rate (cm/h)	**Clogging Cycles with Suspension**						
	0	1	2	3	4	5	6
Light Rain (<0.25)	-	0.8	1.0	1.2	1.2	1.3	1.3
Moderate Rain (0.25-1)	2.5	2.6	2.7	2.7	2.7	2.7	2.7
Heavy Rain (1-5)	4.7	4.8	4.8	4.8	4.8	4.8	4.8

Based on clogging test results reported in the literature, the maximum water flow depths after clogging on the roadway with eight-lanes can be calculated, which are presented in Tables 4.7 and 4.8. The maximum water film depths were calculated under the following conditions: slope s=0.02, thickness of PFC b=5 cm, kinematic viscosity $v = 0.01\ cm^2/s$, and initial hydraulic conductivity is 1 cm/s .

Figure 4.9 shows the variation of hydroplaning speed with different clogging rates of hydraulic conductivity for the roadway with eight lanes at different rain rates. The clogging rate of hydraulic conductivity was calculated as the loss percent of hydraulic conductivity due to deformation-related or particle-related clogging. The results show that although pore clogging has negative effect on hydraulic conductivity, the effect on hydroplaning was only significant at light rain. At moderate to heavy rain rates, the effect of clogging on hydroplaning is very limited. This is similar to the effect of hydraulic conductivity of PFC.

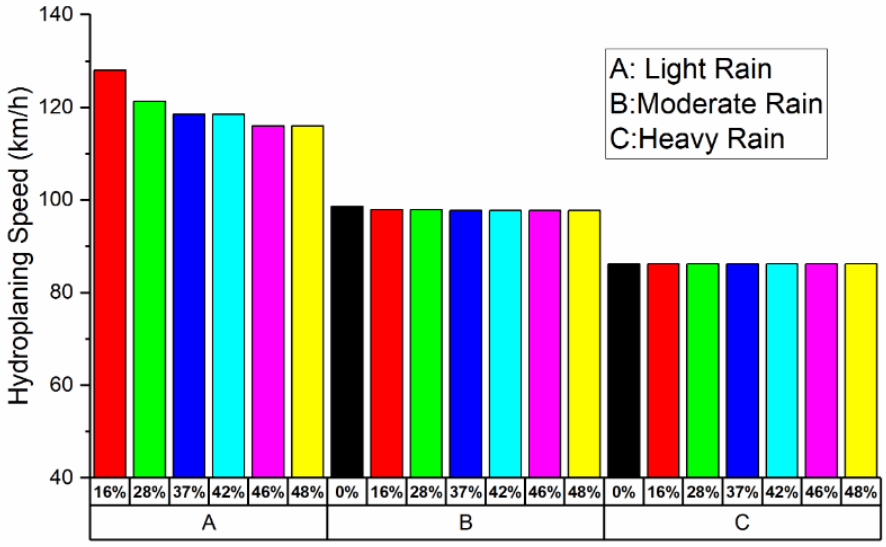

(a)

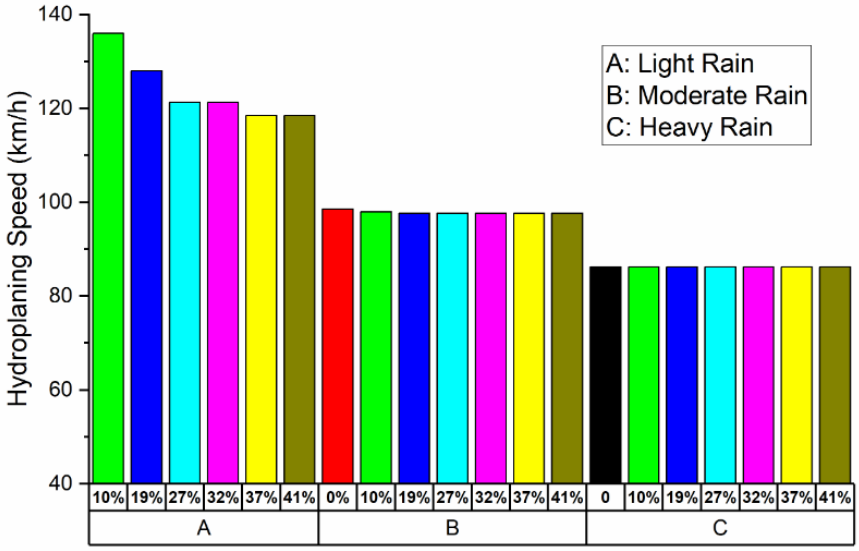

(b)

Figure 4.9 Hydroplaning speeds due to clogging: (a) deformation-related clogging; (b) particle-related clogging

4.4.4 Effects of Cross Slope on Hydroplaning Risk

The effect of cross slope on hydroplaning risk is discussed in the subsection. The maximum water film depths on the cross section with eight lanes were calculated under the following conditions: thickness of PFC $b = 5\,cm$, hydraulic conductivity of PFC $K = 1$ *cm/s*, and kinematic viscosity $v = 0.01$ cm^2/s.

Table 4.9 presents the maximum sheet flow depths on different lanes., The results that for cross section with six or less than six lanes, there was no water flow accumulated on road surface in light rain. When the cross slope increased to 2% in light rain, there was no water flow on the 4th lane in the roadway with 8 lanes. In moderate to heavy rain rates, the increase of cross slope can also significantly improve the drainage performance of

roadway. For example, the water film depth reduced from 2.9 mm to 1.8 mm and from 5.3 mm to 3.7 mm in moderate rain and heavy rain, respectively.

Table 4.9 Maximum Water Flow Depths (mm) on Different Lanes

Rain rate (cm/h)	Lane number	**Cross Slope (%)**					
		1.5	2	2.5	3	3.5	4
Light Rain (<0.25)	1	-	-	-	-	-	-
	2	-	-	-	-	-	-
	3	-	-	-	-	-	-
	4	1.2	-	-	-	-	-
Moderate Rain (0.25-1)	1	1.1	-	-	-	-	-
	2	2.1	1.7	1.4	1.2	0.8	-
	3	2.6	2.2	2.0	1.8	1.6	1.4
	4	2.9	2.6	2.3	2.1	1.9	1.8
Heavy Rain (1-5)	1	3.1	2.7	2.5	2.3	2.1	1.9
	2	4.1	3.7	3.4	3.1	3.0	2.8
	3	4.7	4.3	4.0	3.7	3.5	3.3
	4	5.3	4.8	4.4	4.1	3.9	3.7

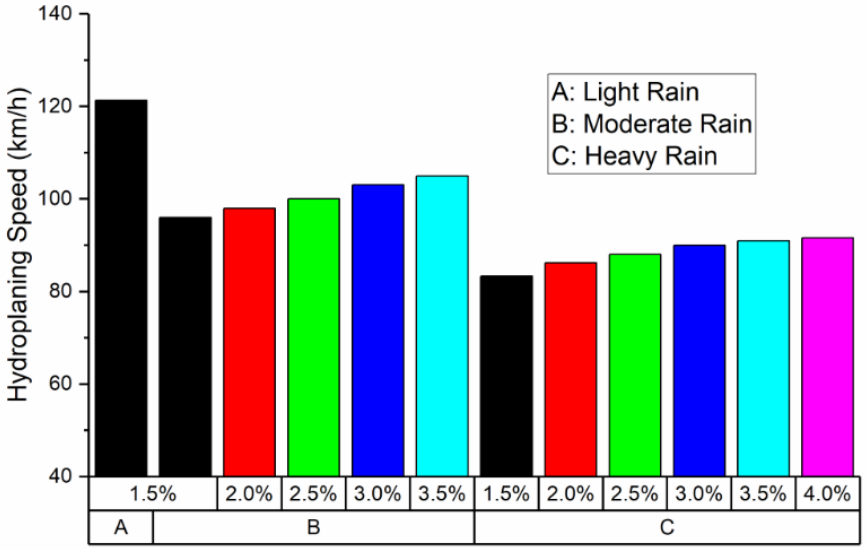

Figure 4.10 Hydroplaning speeds at different cross slopes

Figure 4.10 shows the hydroplaning speeds on the fourth lane at different rain rates, which has the highest hydroplaning potential among different lanes. The results indicate that the increase of cross slope significantly improves driving safety at rainy condition. For the roadway with eight traffic lanes, the preferred cross slope to fully prevent hydroplaning was found 2% in light rain 4% in moderate rain since there was no water flow under these conditions. In heavy rain, when the cross slope increased from 1.5% to 4.0%, the hydroplaning speed increased by 10%.

The analysis findings here can help identify potential hydroplaning risk at superelevation transition sections. Typically, at curved sections, the cross slopes of traffic lanes between the centerline and the inside edge are higher than the ones in the straight section to counteract centrifuge force (Wolhuter 2015). However, transition section is needed between straight and circular sections to convert the crown shaped road cross section to one-directional cross section with superelevation. At certain locations in the transition sections the cross slope between the centerline and the outside edge becomes horizontal (zero cross slope), which would drastically increase hydroplaning potential at these locations. Therefore, warning signs are needed to indicate the reduced speed limit in the transition segment before curved sections.

4.4.5 Critical Rut Depth for PFCs

It has been widely recognized that pavement rutting can lead to wet weather accidents due to hydroplaning. Currently, there is no clear guideline on what rut depths will result in critical water depth for hydroplaning. In this section, the rut depth threshold on PFCs was

analysed based on hydroplaning risk. According to Glennon (2015), the maximum amount of water that the rut can hold can be calculated using Equation 4-3.

$$WFD = d - Ls \tag{4-3}$$

where,

WFD is water film depth (in);

d is measured rut depth (in);

L is the measurement from the lower side of rut to the position of the maximum depth (in);

s is cross slope.

It is obvious from Equation 4-3 that the critical rut depth can be calculated from the critical water film depth at a given cross slope and rut width; while the critical water film thickness can be determined at the specific speed limit range using the developed hydroplaning model and from Equation 4-1 considering sheet flow.

Figure 4.11 presents the critical rut depths at the given critical water film depth on the fourth lane for various cross slopes with pavement thickness of 5 cm and hydraulic conductivity of 1 *cm/s*. The width of rutting was assumed three feet with the maximum depth at the centerline. It is generally thought that the slight rutting (< 8 mm deep) can be left untreated. However, the results show that the maximum allowed vehicle speed to avoid hydroplaning differs among different road sections, in which the critical rut depths would vary accordingly. In addition, the analysis findings illustrate that the road section with higher cross slopes tend to be less sensitive to hydroplaning risk due to pavement rutting. Therefore, the lower thresholds of rutting depths for maintenance treatments should be

given to the road sections with relatively flat cross slopes from the aspect of roadway safety.

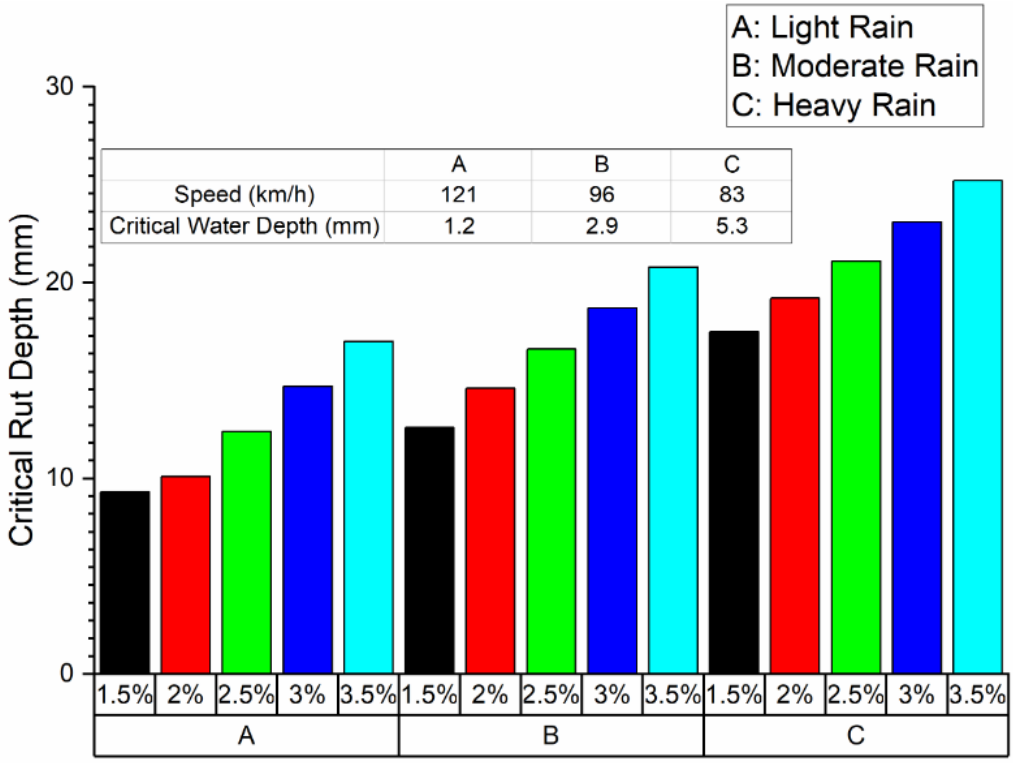

Figure 4.11 Critical rut depths at the given critical water film depths (speed limits) for various cross slopes

4.5 Braking Distance Analysis

4.5.1 Braking Distance and Skid Number

The previous sections focus on hydroplaning analysis. However, for safe driving on the road surface, the minimum stopping sight distance, which is computed as the sum of reaction distance and braking distance, need be considered in geometric design of roadway (AASHTO 2011). Reaction distance is defined as being the distance travelled during the

driver's perception reaction time, while braking distance is the distance that the braking action requires to make the vehicle come to a complete stop.

According to the AASHTO's Policy on Geometric Design of Highways and Streets ("Green Book") (AASHTO 2011), the approximate braking distance for a vehicle travelling on a level road can be determined by Equation 4-4.

$$d = 0.039 \cdot \frac{V^2}{a} \tag{4-4}$$

where,

d is braking distance (m);

V is vehicle speed (km/h);

a is deceleration (m/s^2).

Braking studies indicates that approximately 90% of all drivers brake with a deceleration rate of more than 3.4 m/s^2 which prevents the motorist from losing control when braking (AASHTO 2011). Thus, 3.4 m/s^2 is used as the recommended deceleration value in the AASHTO Green Book. However, previous studies have found that the deceleration rate depends on the braking system as well as tire/pavement skid resistance. The skid resistance depends on vehicle speed, tire type, tire inflation pressure, tire vertical load, pavement texture, and water film thickness etc. (Rose 1977; Anderson et al. 1998). Skid resistance is defined as the force developed when a tire prevented from rotating slides along the road surface (Highway Research Board 1972). During the braking process, as the vehicle speed decreases, the skid resistance (as shown in Equation 4-5) changes

accordingly. In highway engineering practice, skid number (SN) can be related to tire-pavement coefficient of friction (u) by Equation 4-6.

$$SN_v = 100 \times \frac{F_x}{F_z} \tag{4-5}$$

$$u = 0.01(SN) \tag{4-6}$$

where,

F_x is the horizontal resistance force to motion on the tire;

F_z is the vertical wheel load.

4.5.2 Computation of Braking Distance

As stated in previous section, the AASHTO Green Book uses a constant deceleration rate to represent an overall operating condition considered to be safe for road geometric design, which is contradicting to practicality. In this section, we calculate braking distance based on the mechanism and principle of vehicle braking, which can capture the variation of deceleration rate with vehicle speed and water film depths. Figure 4.12 illustrates the methodology of computing braking distance on road surface.

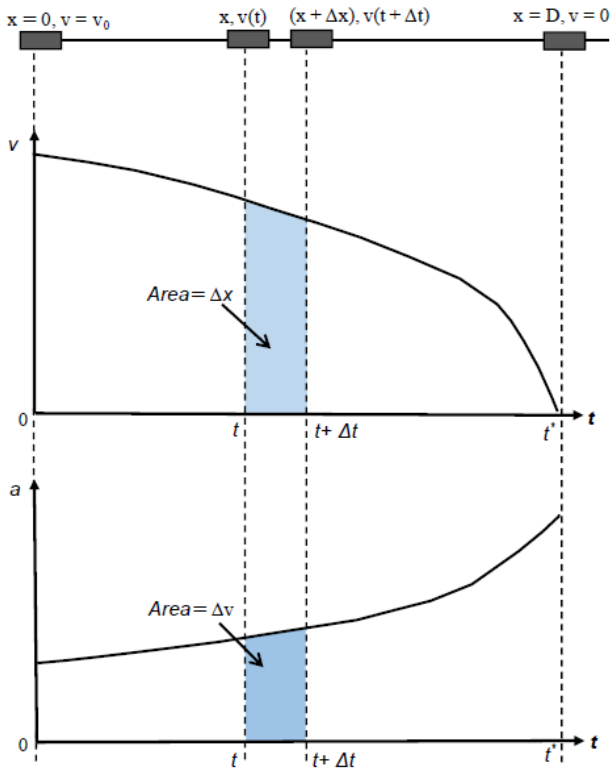

Figure 4.12 Mathematical representation of vehicle braking distance (adapted from Ong and Fwa 2010)

The braking distance of a specific vehicle travelling on a given road surface is a function of the vehicle initial speed and the skid resistance on the pavement surface. Equation 4-7 presents the general equation of braking distance computation.

$$D = \int_0^T v(t)dt = \sum_i (\Delta x)_i \tag{4-7}$$

where,

D is braking distance in m;

$v(t)$ is vehicle speed at time t;

$t = 0$ is time when the brake is first applied;

$t = T$ is time when the vehicle comes to full stop;

Δx is the distance travelled over a time period Δt.

The vehicle speed at given time t_1, can be obtained by Equation 4-8:

$$v(t_1) = v(t = 0) - \int_0^{t_1} a(t)dt \tag{4-8}$$

where,

$a(t)$ is the deceleration rate at given time t.

From Newton's second law of motion, the deceleration rate can be interpreted by the pavement coefficient of friction and the grade of road surface, as shown in Equation 4-9.

$$a(t) = [u(t) + G]g \tag{4-9}$$

where,

$u(t)$ is coefficient of friction between tire and wet road surface;

G is pavement grade; g is gravitational acceleration.

4.5.3 Validation of Skid Resistance

According to Equations 4-7 to 4-9, the computation of braking distance requires the determination of skid number or coefficient of pavement friction as vehicle speed decreases in the braking process. Many past experimental studies (Horne and Tanner 1969; Agrawal and Henry 1977; Rose and Gallaway 1977) have been conducted to test the skid resistance number on wet pavement state in ASTM E274 (ASTM 2005a) using the ASTM E524 smooth tire (ASTM 2005b).

In order to predict the skid resistance number, the skid resistance predicting method was first validated against the experimental data with an ASTM standard E524 smooth tire (Agrawal and Henry (1977)). The test method measures the steady-state friction force on a locked wheel when it is dragged over road surface with specific water film depths under constant load and at constant speed (ASTM 2005a).

Figure 4.13 (a) shows the cross section of the ASTM standard E524 smooth tire profile. The tire tread width shall be 148.6 mm. and the radius of the cross-sectional is 393.7 ± 50.8 mm. The tread depth is 9.8 mm and the under tread depth is 2.5 mm. The recommended cross-section width of the tire is 212.1 mm and the height should be 161.0 mm when mounted on a rim. The cured crown angles for the body plies and belt plies are $33 \pm 2^{\circ}$ and $27 \pm 2^{\circ}$, respectively. Based on the cross section dimensions, the 3D tire model of ASTM standard E524 smooth tire was built presented in Figure 4.13 (b).

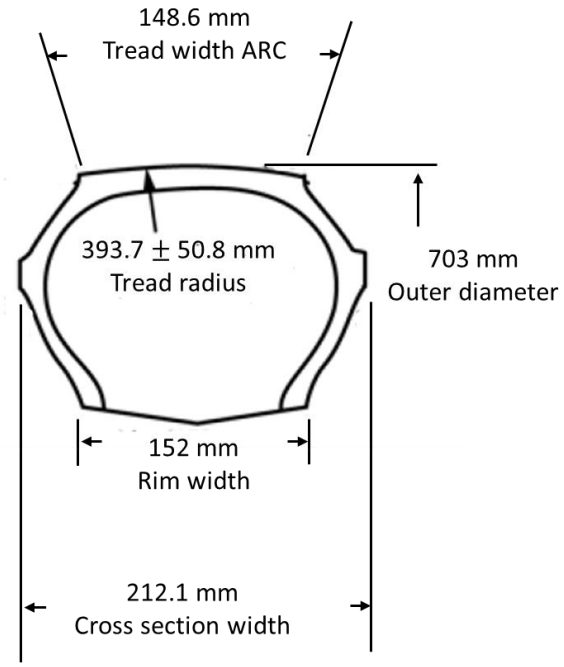

(a)

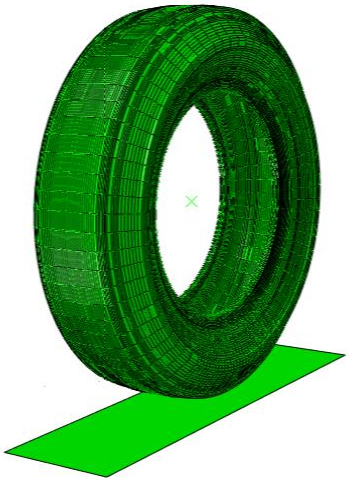

(b)

Figure 4.13 ASTM standard E524 smooth tire: (a) tire section (ASTM 2005b); (b) 3D tire -pavement interaction model

An unknown parameter required for the simulation is the initial frictional coefficient, which represents the friction at tire-pavement interface at close-to-dry condition without water film. The initial frictional coefficient was assumed 0.35 in the measurement, which fell within the lower end of the range of common friction coefficient (0.3-0.7) on pavement surface (Lee et al. 2005). This is because the smooth tread surface (no groove) of test tire has the least friction on wet surface and the test tire is locked at full sliding.

Table 4.10 presents the comparison of skid resistance between the experimental data from Agrawal and Henry (1977) and the predicted values. The analysis was conducted for ASTM E524 smooth tire (ASTM 2005b) with inflation pressure of 165.5 kPa and

vertical load of 2861 N. The validation results show that the percentage differences of skid resistance between measurements and predictions are smaller than 5%, which demonstrates the proposed method is valid for prediction of skid resistance.

Table 4.10 Skid Resistance Validation at Water Film Thickness of 1.47 mm

Test Speed (km/h)	Measured SN_v	Predicted SN_v	Percentage Difference (%)
48	30	30.8	2.7
64	20	20.9	4.5
72	15	15.7	4.6
80	12	12.5	4.2

4.5.4 Determination of Braking Distance on Wet Pavement

Once the skid resistance prediction method is validated, the approach was applied to 205 tire skid resistance and braking distance analysis. The skid number at various vehicle speeds can be obtained from the fluid structure interaction model. Unlike in the hydroplaning analysis we are finding the hydroplaning speed (when skid resistance equals zero), in the skid resistance analysis, the vehicle speed is selected no greater than the hydroplaning speed.

Table 4.11 Skid Number and Coefficient of Friction at Various Vehicle Speed and Water Film Depths

Speed (km/h)	Water Film Depth (mm)	Skid Number	Coefficient of Friction
16	0.5	67	0.67
	5	48	0.48
32	0.5	58	0.58
	5	34	0.34
48	0.5	54	0.54
	5	29	0.29
64	0.5	48	0.48
	5	21	0.21
80	0.5	29	0.29
	5	10	0.10
96	0.5	15	0.15
	5	0	0.00

The skid number were calculated under two water film depths, 0.5 mm and 5 mm, which respectively represents a typical water film depth at low rain rate and heavy rain rate. The vehicle speed is increased from 16 km/h to 96 km /h with an interval of 16 km/h. The tire is loaded with inflation pressure of 187 kPa and vertical load of 3,767 N. The initial dry friction coefficient was assumed 0.70 for the P 205 tire with tread grooves at 18% slip ratio. Table 4-11 presents the skid numbers at different speeds and water film depths.

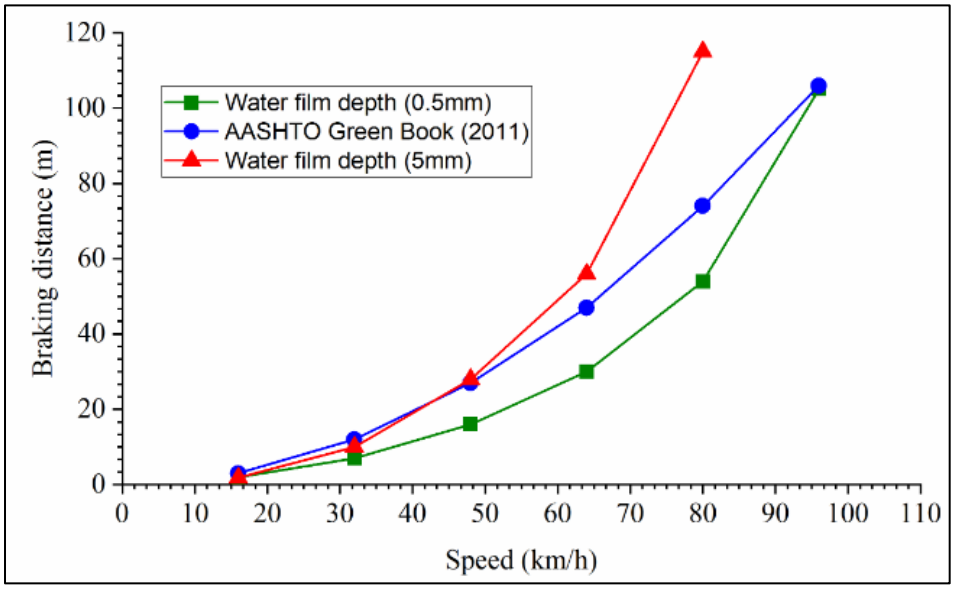

Figure 4.14 Comparison of the braking distance between the AASHTO standard and the predicted values

Figure 4.14 shows the braking distances calculated with varying coefficients of friction and water film depths as compared the one calculated using AASHTO equation. As expected, the vehicle braking distance increased with the increase of water film depths, since the skid resistance decreased with the increase of water film thickness. For example, for a vehicle speed of 48 km/h, the braking distance increased by 75% when water film depth is increased from 0.5 to 5 mm. In addition, it was also observed that the braking distance increased with the increase of vehicle speed. For example, the braking distance increased by 95% at water film depth of 0.5 mm when the vehicle speed increased from 80 to 96 km/h. This slope of increasing braking distance with initial speed is more significant as the water film thickness is greater.

The importance of considering water film thickness in braking distance analysis can be observed from the figure. It is obvious that the braking distance calculated using AASHTO equation may underestimate safety risk in wet weather at certain conditions of water film depth and vehicle speed. For example, the braking distance required by AASHTO is 47 m at vehicle speed of 64 km/h, which satisfies the requirement of braking distance on road sections with 0.5 mm water film depth. However, it has safety risk at the same vehicle speed when the water film depth is 5 mm, which requires braking distance of 56 m.

4.6 Proposed Framework and Design Procedure

The above analysis demonstrates proper design of PFC layer and cross section may reduce hydroplaning risk. The application of PFCs can improve wet weather safety by providing subsurface drainage, especially in areas exposed to light rain rates. However, the safety benefit can vary depending on and the cross-section slope of roadway design and the layer thickness and hydraulic conductivity of PFCs. In addition, since PFCs may gradually be clogged and partially lose hydraulic conductivity, frequent cleaning of clogged PFCs is necessary to extend the safety performance of PFCs. All these factors will affect the accumulated water film depth on pavement surface, which is the key parameter for hydroplaning for the specific tire loading condition. Figure 4.15 shows an example of quantitative relationship between hydroplaning speed and water film depths for the tire loading condition considered in this study. The results show that the hydroplaning speed decreases as water film depth increase in an exponential relationship.

The hydroplaning risks will increase with the increase of number of traffic lanes (drainage length). When multi lanes are present, the negative impact of longer drainage path lengths can be mitigated through appropriate application of PFC layer properties and/or cross slope. Special attention should be given to roadway sections prone to rutting, where the water film depth increases due to ponding water on the road surface.

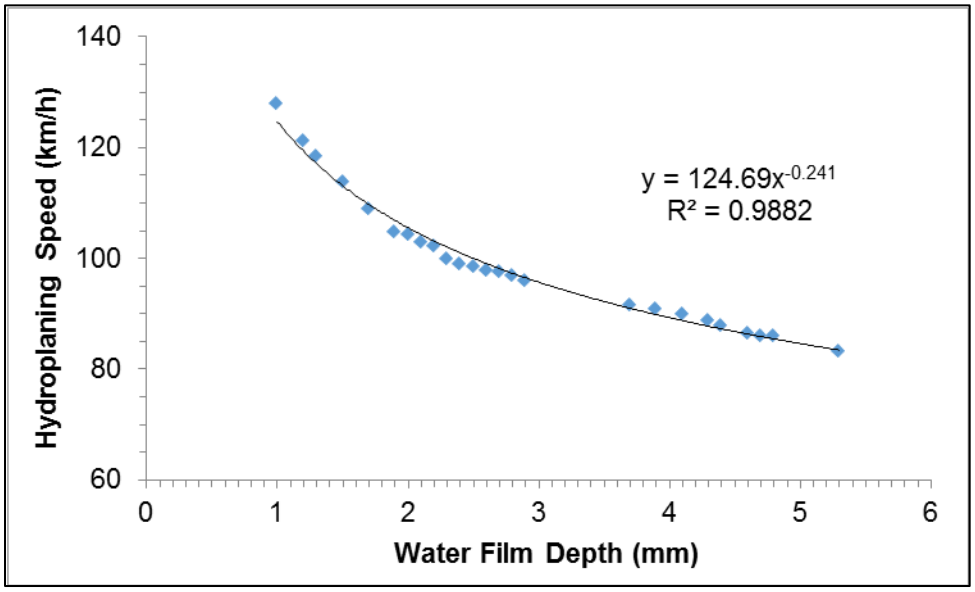

Figure 4.15 Hydroplaning speed at various water film depths

Based on the foregoing analysis and discussions**,** the framework of incorporating hydroplaning in pavement and cross section design is shown Figure 4.16. The framework can be extended to consider braking distance requirements. The proposed framework consists of the following main steps:

1) Step 1: Determination of design parameters of PFC and roadway cross section, including the thickness, porosity, hydraulic conductivity of PFC, the number of traffic lanes, lane width, and cross slope.

2) Step 2: Selection of the rain rates based on climate records, which can be the design value used in roadway design.

3) Sep 3: Determination of water film thickness at each traffic lane along the drainage path according to the selected rain rates and roadway design parameters.

4) Step 4: Determination of tire loading condition for hydroplaning analysis. This is usually passenger car since the lighter load has the higher hydroplaning potential.

5) Step 5: Determination of the desired hydroplaning speed. After determining the critical tire loading condition and the predicted maximum water film depths at each traffic lane, the hydroplaning speed can be calculated using the 3D fluid-structure interaction model or the pre-estimated relationship between water film depth and hydroplaning speed (such as Figure 4.15).

6) Step 6: Comparison of hydroplaning speed, skid resistance and braking distance with requirements. The critical hydroplaning speed should be selected from the minimum hydroplaning speed on the outer lane.

7) Step 7: Revision of design parameters or adaptation of risk mitigation methods (such as reducing speed limits, setting warning signs, implementing vehicle restriction, etc.).

8) Step 8: Finalization of design parameters.

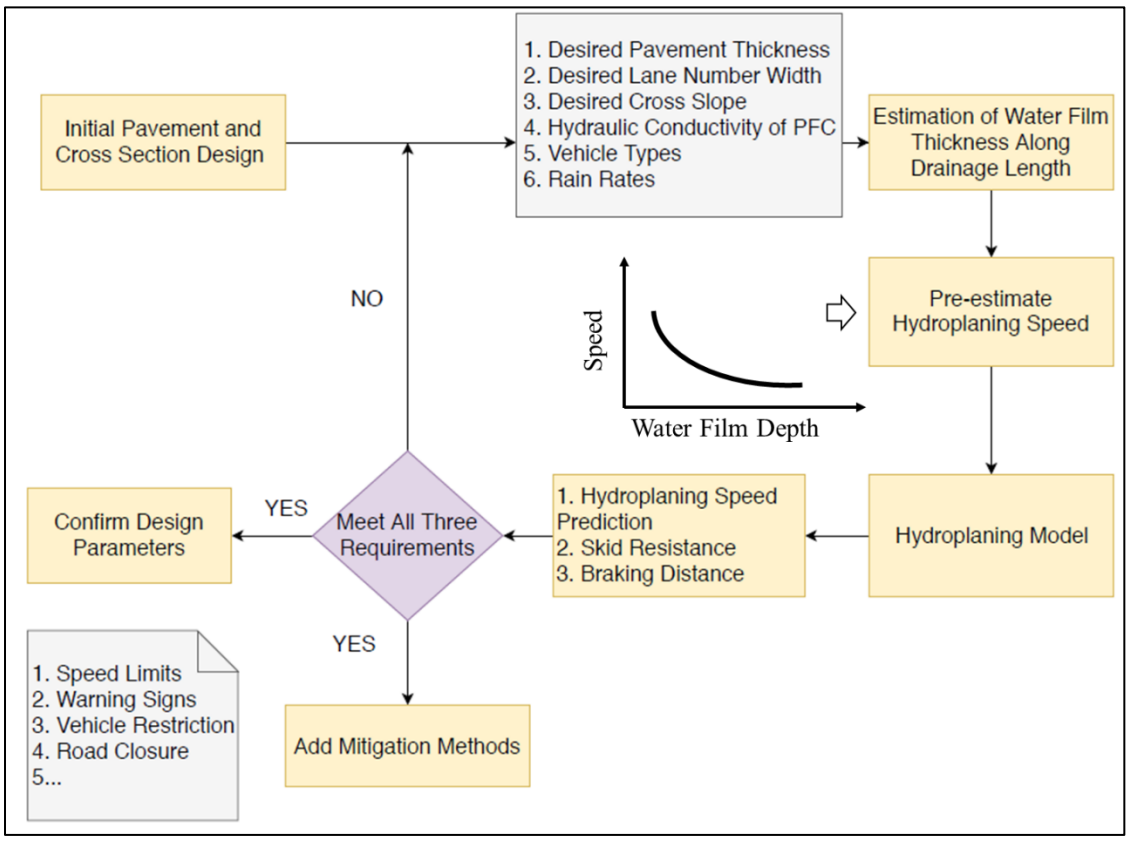

Figure 4.16 Framework of incorporating hydroplaning in pavement and cross section design

4.7 Summary

This chapter presented an analytical framework to evaluate hydroplaning risk of multi-lane roadway with PFC using a fluid-structure interaction model. For this purpose, the water film depths along the drainage length were predicted from a mathematical model which combines sheet flow and flow inside PFC. The hydroplaning speed was calculated using the developed grooved tire-water-pavement interaction model. The hydroplaning model can successfully identify the locations on multi-lane roadway that has high

susceptibility to hydroplaning.

The results demonstrate that PFC can effectively reduce hydroplaning risk for 2-lane roadway under light to moderate rain rates as compared to impervious pavements. The findings show that hydroplaning risk becomes more apparent as the number of traffic lanes increase or with the presence of pavement rutting. Therefore, hydroplaning risk on roadway with more than 6 traffic lanes under heavy rainfall intensity, can still exists on PFC.

The quantification of hydroplaning speed using the developed model can help transportation agencies reduce wet-weather safety risk by setting counter plans depending on rain rates and cross section design. The study findings can guide the project selection of PFCs at the locations having high hydroplaning risk. It is apparent, according to this study, roadways with 2-lane to 4-lane cross sections under light to moderate rain rates can benefit most from the implementation of PFC.

The braking distance was calculated using the integral of vehicle speed versus time during the vehicle braking process. The coefficients of friction or skid numbers were calculated using the tire-pavement contact forces at different water film depths and vehicle speeds. The analysis results demonstrate that the vehicle braking distance increases with the increase of water film depths, since the skid resistance decreases. It was found that the braking distance requirements calculated using AASHTO equation has safety risk at the condition of thick water film and high vehicle speed.

The proposed framework enables highway agencies to evaluate the safety performance of roadway design in terms of hydroplaning potential and braking distance. The safety countermeasures can be implemented based on the predicted hydroplaning speed as

compared to the speed limit. In addition, the critical rut depth threshold of PFCs can be used for triggering pavement maintenance to prevent hydroplaning due to ponding water. This enables highway agencies to consider safety performance in the decision-making process for roadway design and management.

CHAPTER 5 NUMERICAL EVALUATION OF TIRE ROLLING RESISTANCE

5.1 Hysteretic Loss of Tire

Rubber components of a rolling tire experiences a cyclic variation in the dynamic deformation, strain and stress fields, producing the severe hysteretic loss owing to the inherent phase difference between stress-and strain-time histories. The hysteretic loss of a rolling tire becomes a crucial factor causing the dissipation of power supplied to the tire axes (Clark 1978; Whicker 1981), and the tire hysteretic loss per revolution is interpreted as pseudo force resisting the tire rolling. This pseudo force is commonly called the rolling resistance (Pacejka 2002). Generally, rolling resistance from material energy dissipation is identified as RR_e , whereas the mechanical manifestation of rolling resistance as a horizontal force is interpreted as RR_f .

To better understand tire rolling resistance, consider a viscoelastic tire illustrated in Figure 5.1(a). The tire is subjected to vertical sinusoidal displacement excitation at the tire pavement contact patch. Take a random point within the tire, the sinusoidal time histories of the axial strain and stress at this point is depicted in Figure 5.1 (b), with the phase lag δ . Then, the resulting hysteretic loss ΔW per unit volume during a period $T_c = 2\pi/\omega$ is calculated by Equation 5-3:

$$\varepsilon(t) = \varepsilon_0 \sin(\omega t) \tag{5-1}$$

$$\sigma(t) = \sigma_0 \sin(\omega t + \delta) \tag{5-2}$$

$$\Delta W = \int_0^{T_c} \sigma(\tau) \frac{d\varepsilon(t)}{d\tau} d\tau = \int_0^{T_c} \sigma_0 \varepsilon_0 \sin(\omega t + \delta) \cos(\omega t) d\tau = \pi \sigma_0 \varepsilon_0 \sin\delta \quad (5\text{-}3)$$

where,

σ_0 being the stress;

ε_0 being the strain amplitudes;

ω being the excitation frequency.

The total hysteretic loss of the viscoelastic tire during a cycle becomes the sum of the point-wise hysteretic losses given in Equation 5.3 over the entire tire material domain (Cho 2013).

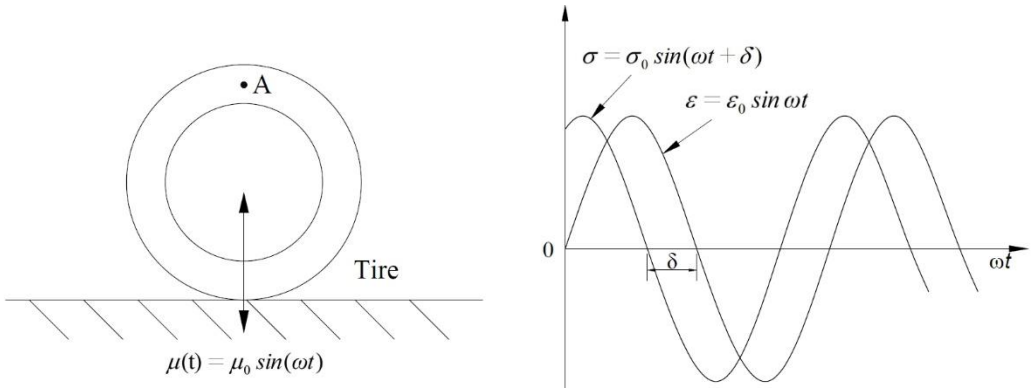

(a) (b)

Figure 5.1 Illustration of (a) viscoelastic tire subject to a sinusoidal displacement excitation; and (b) time histories of strain and stress at point A of tire

However, in most engineering applications, the 3-D viscoelastic bodies are subjected to more complicated multi-axial cyclic excitations, so the time histories of strains and stressed are not perfectly one-dimensional or sinusoidal (Mars 2001). Thus, in such cases, the hysteretic loss in Equation 5.3 is expressed in a generalized from given by

$$\Delta W = \int_0^{T_c} \sigma_{ij}(t) \frac{d\varepsilon_{ij}(t)}{dt} dt \tag{5-4}$$

The rubber components of the rolling tire exhibit the complicated 3-D dynamic viscoelastic deformation, and their dynamic viscoelastic properties are usually characterized by responses to the sinusoidal strains and stresses which are presented in terms of the complex modulus:

$$G^* = G' + iG'' \tag{5-5}$$

where,

G' is the storage (in-phase) modulus;

G'' is the loss (out-of-phase) modulus;

The complex modulus is a function of the strain amplitude ε_0, frequency f, and temperature T (Kramer and Ferry 1994). The storage and loss moduli are correlated in term of the phase difference δ is given in Equation 5-6:

$$\tan\delta = \frac{G''}{G'} \tag{5-6}$$

To predict the hysteretic loss of a rolling tire exhibiting the multi-axial state of strain and stress caused by a non-sinusoidal periodic excitation in steady state free rolling, the following Fourier decomposition equations (Equations 5-7 and 5-8) were used to obtain stress-strain amplitude at different frequencies,

$$\bar{\varepsilon} = \sum_{m=0}^{M} \bar{\varepsilon}_m \cos\left(2\pi m t / T\right) \tag{5-7}$$

$$\bar{\sigma} = \sum_{m=0}^{M} \bar{\sigma}_m \cos\left(2\pi mt/T + \delta\right) \tag{5-8}$$

where,

$\bar{\varepsilon}$ is the equivalent strain;

$\bar{\sigma}$ is the equivalent stress;

$\bar{\varepsilon}_m$ is the amplitude of equivalent strain;

$\bar{\sigma}_m$ is the amplitude of equivalent stress;

T is time period;

δ is phase lag.

Then the energy loss in one revolution can be obtained by Equation 5-9

$$W = \int_0^T V_i \bar{\sigma} d\bar{\varepsilon} \tag{5-9}$$

where,

V_i is the volume of the circumferential element i.

Substitute Equations 5-7 and 5-8 into Equation 5-9, the energy loss in one revolution

$$W_L = \pi \sin\delta \sum_{i=1}^{J} \sum_{m=1}^{N} m V_i \bar{\sigma}_{m,i} \bar{\varepsilon}_{m,i} \tag{5-10}$$

where,

N is the Fourier Series expansion number;

J is the number of elements in a rubber component;

As can been seen from Equation 5-10, once the amplitude of equivalent strain and stress, and phase lag δ are obtained, the energy loss is determined. Meanwhile, the rolling resistance (F_{RR}) caused by the hysteretic loss is calculated by dividing the total hysteretic

loss (W_{Loss}) of the rolling tire during one revolution by the traveling distance of tire during the same period, as shown in Equations 5-11 and 5-12 (Cho et al. 2006).

$$F_{RR} = \frac{W_{Loss}}{2\pi r_e} \tag{5-11}$$

$$C_{rr} = \frac{F_{RR}}{F_v} \tag{5-12}$$

where,

r_e denotes the effective radius and the volume of rubber material;

F_v is tire vertical load;

C_{rr} is rolling resistance coefficient.

5.2 Numerical Modeling and Validation

5.2.1 Tire Finite Element Model Generation

Base on the actual profile of a 205/60R16 radial patterned passenger car tire, and considering tread, sidewall, carcass, belts, apex, bead, etc., the structure and boundaries about various tire components are set up. The following main characteristics of tire model are considered: (1) the composite material and the anisotropy resulted from the stiffness difference between rubber and reinforcement; (2) the relatively large deformation due to the flexibility of tire carcass during tire-pavement interaction; and (3) the nearly incompressible and nonlinearity of rubber (Wong 2018). The rubber component is modeled as an incompressible hyperelastic material, and this behavior is described by the Neo-Hookean material formulation (Equation 5-13) while the fiber reinforcement is modeled as

a linear elastic material (Ding 2016; 2017; 2018).

$$U = C_{10}(\overline{I}_1 - 3) + \frac{1}{D_1}(J^{el} - 1)^2 \tag{5-13}$$

where,

U is the strain energy per unit of reference volume;

C_{10} and D_1 are temperature-dependent material parameters;

$\overline{I}_1$ is the first deviatoric strain invariant defined as $\overline{I}_1 = \overline{\lambda}_1^2 + \overline{\lambda}_2^2 + \overline{\lambda}_3^2$, $\overline{\lambda}_i = J^{-\frac{1}{3}}\lambda_i$;

J is the total volume ratio;

J^{el} is the elastic volume ratio;

λ_i are the principal stretches.

The initial shear modulus and bulk modulus are given by $\mu_0 = 2C_{10}$ and $K_0 = 2/D_1$. The simulation of FE tire/pavement interaction model includes four steps. In the first step, an internal inflation pressure was applied on the axisymmetric tire model. Next, the 3-D wedges with tire structure were generated by revolving the axisymmetric model about its axis of revolution. In the third step, the inflation pressure and vertical load were applied to the model. In the last step, the inflated tire reached a stationary rolling condition at a constant travelling speed.

Figure 5.2(a) presents the tire cross-section, which includes 1,552 nodes, 1,408 elements, and 14 components. Figure 5.2(b) shows the three-dimensional tire model on a flat surface. The tire had inflation pressure of 220 kPa and vertical load of 3,767 N. The validation process of the FE modeling of tire can be found in Chapter 4.

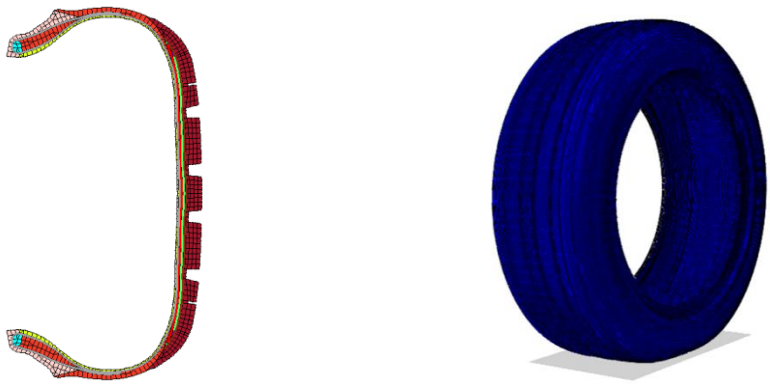

(a) (b)

Figure 5.2 Tire finite element models (a) tire cross-section; and (b) 3-D tire model

5.2.2 Tire Rolling Resistance Data Collection

Rubber material shows strong viscoelastic effects during cyclic deformation, and the viscoelastic properties can be described by a combination of springs (representing elastic component) and dashpots (representing viscous component) as represented by Maxwell-element. Elastic material does not show any energy dissipation and therefore pure elastic tire simulation does not provide energy loss. In rolling resistance simulation, the dissipation can be described by Eq. 5-6, which is the ratio of loss modulus (dissipated energy) to storage modulus (elastic energy) in a harmonic loading resulted from rubber process analyzer (RPA) test.

Figure 5.3 presents the loss factor of the RPA 2000 test result for an example of rubber component conducted at different temperatures and strain levels. The testing frequency was fixed at 11 Hz, and the temperature ranged from 37 to 70 ºC with interval of 3 ºC. The testing strain level was set at 1%, 5%, 10%, 15%, 20%, 30% and 40% considering typical

tire loading conditions. As can be seen from the figure, the loss factor of rubber material generally decreased with the increase of temperature, whereas it showed nonlinear variation with the strain level.

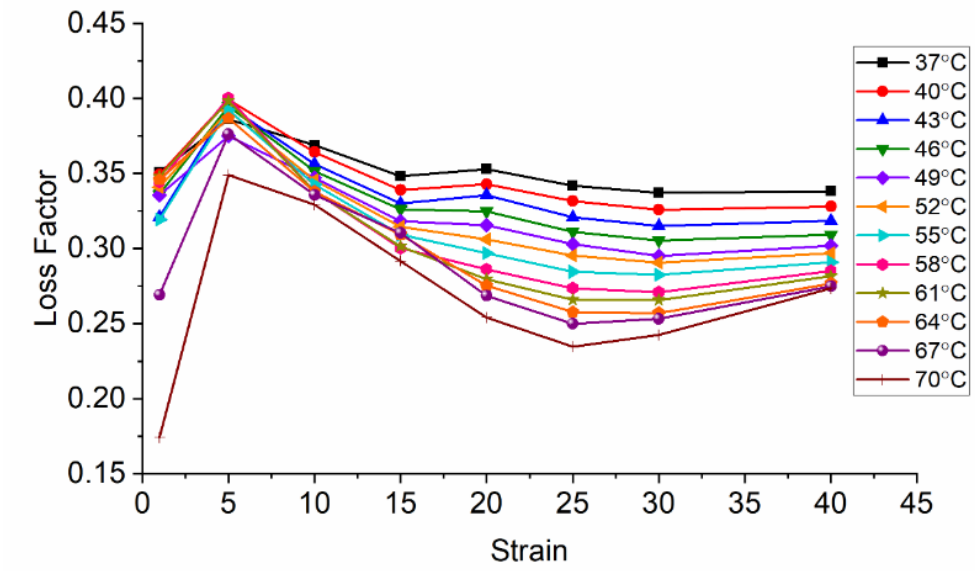

Figure 5.3 Sample of loss factor of one rubber component under different temperature and strain levels

Based on the engineering judgement and regression analysis, the following fitting function (Equation 5-14) was selected to predict the loss factor at broader temperature and strain levels through the nonlinear least squares fitting.

$$\text{Tan}\,\delta = Ax^2y^2 + Bx^2y + Cx^2 + Dxy^2 + Exy + Fx + Gy^2 + Hy + I \qquad (5\text{-}14)$$

where,

$\text{Tan}\,\delta$ is loss factor of each rubber components;

x is testing temperature (°C);

y is testing strain level;

A, B, C, D, E, F, G, H, I, are the fitting polynomial coefficient respectively.

Table 5.1 presents the summary of the fitting coefficients. In the FE model, every rubber element is determined by several material points called integration points and the dissipated energy was calculated at these integration points. As shown in Eq.5-9, the integration of the dissipated energy was multiplied with material volume and summed over integration point of all rubber elements to obtain the total dissipation energy. The extracted element volume (EVOL), mises stress distribution and logarithmic strain (LE) of one rubber component sample are presented in Figure 5.4, which were further processed in MATLAB to calculate tire rolling resistance.

Table 5.1 Summary of Fitting Coefficients for Loss Factors of Rubber Components

Rubber components	**Polynomial coefficients**									
	A	**B**	**C**	**D**	**E**	**F**	**G**	**H**	**I**	**Residual**
Inner	-2.2E-8	4.5E-6	-2.2E-4	2.4E-6	-4.7E-4	2.4E-2	-7.7E-5	1.5E-2	-0.487	0.0037
Carcass	-1.1E-8	1.5E-6	-5.7E-5	9.6E-7	-8.8E-5	4.4E-3	-2.1E-5	2.9E-3	0.059	0.0027
Belt	-1.4E-9	7.9E-7	-9.0E-5	2.1E-7	-5.3E-5	8.7E-3	-1.1E-7	1.2E-3	-0.071	0.0129
Cap ply	-2.2E-8	3.9E-6	-1.8E-4	2.1E-6	-3.4E-4	1.7E-2	-5.3E-5	1.0E-2	-0.295	0.0044
Apex	4.3E-9	-1.4E-6	6.2E-5	-9.3E-7	2.5E-4	-8.3E-3	1.3E-5	-3.3E-3	0.475	0.0005
Abrasion	3.6E-9	-1.3E-6	6.2E-5	-5.8E-7	1.9E-4	-7.4E-3	-1.8E-6	-4.0E-4	0.292	0.0015
Sidewall	-1.3E-8	2.6E-6	-1.5E-4	1.5E-6	-2.7E-4	1.8E-2	-5.5E-5	1.1E-2	-0.350	0.0025
Tread	-2.4E-9	3.7E-8	-4.1E-6	9.2E-8	5.1E-5	-1.5E-3	1.3E-6	-4.0E-4	0.260	0.0123

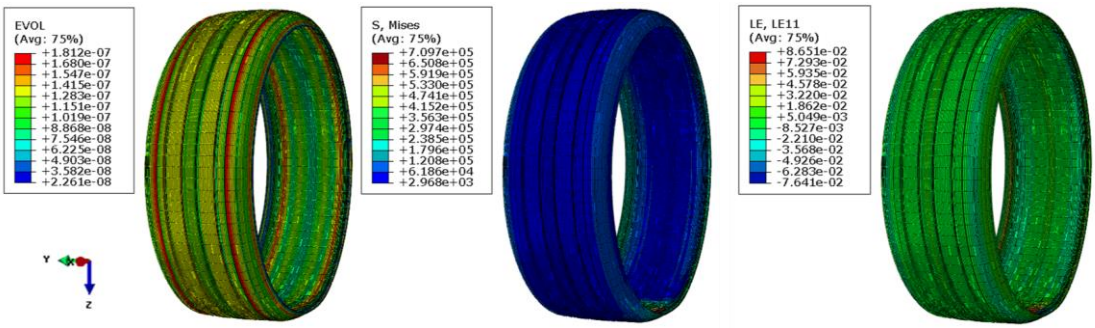

(a) (b) (c)

Figure 5.4 Data extraction for rolling resistance calculation (a) element volume; (b) mises stress; and (c) logarithmic strain

5.2.3 Tire Rolling Resistance Validation

The rolling resistance simulation results were compared with the experimental measurement carried out at R&D Center of Kumho Tire Co. according to the constant velocity method regulated at ISO 28580 (Lee et al. 2014). In the study, the experimental tire was inflated with the same internal pressure as in the simulation study. The tire was in contact with the drum rolling with constant angular velocity under the normal contact force between the drum and testing tire at room temperature of 25 ºC. The tire was rolling at constant speed of 80 km/h.

Table 5.2 Comparison of Rolling Resistance with Experiment

Item	**Experiment** (Lee et al. 2014)	**Current Simulation**	**Difference (%)**
Hysteretic loss (W)	936.04	967.68	3.4
F_{RR} **(N)**	42.10	43.55	

The comparisons of rolling resistance obtained from the developed model and experimental measurements were summarized in Table 5.2. A good agreement was

observed between the predicted rolling resistance and hysteretic loss from the proposed model and the experiment measurements. The validations indicate that the proposed tire-pavement interaction model properly predicts tire rolling resistance.

5.2.4 Three-Dimensional Coupled Tire-Pavement Interaction Model

After the predicted tire rolling resistance on drum test was validated, a coupled tire-pavement interaction model was developed to calculate tire rolling resistance on real pavement surface. Figure 5.5 illustrates the 3-D coupled tire-pavement interaction model with elastic asphalt layer as road surface layer. The free rolling equilibrium solution of tire traveling at a specific velocity on road surface was realized by steady-state transport analysis.

This analysis uses mixed Eulerian/Lagrangian approach in which, to an observer in the moving reference frame, the material appears to flow through a stationary mesh (ABAQUS 2010). This kinematic description has advantage of converting steady moving contact problem into pure spatially dependent simulation. Therefore, only the mesh in the contact region the needs be refined; the steady motion transports the material through the mesh.

For the 3-D coupled tire-pavement interaction model, the horizontal dimensions of elements around the vehicle loading area were dictated by tire rib and groove geometries. Thus, the length of elements within the loading area was selected at 10 mm in the transverse direction and 17 mm in the longitudinal (travel) direction to have good aspect ratios (Wang and Li 2016). The element thicknesses were selected to be 5 mm for asphalt surface layer 8 mm for other layers to have enough accuracy and smooth stress transitions along

pavement depth (Li et al. 2017).

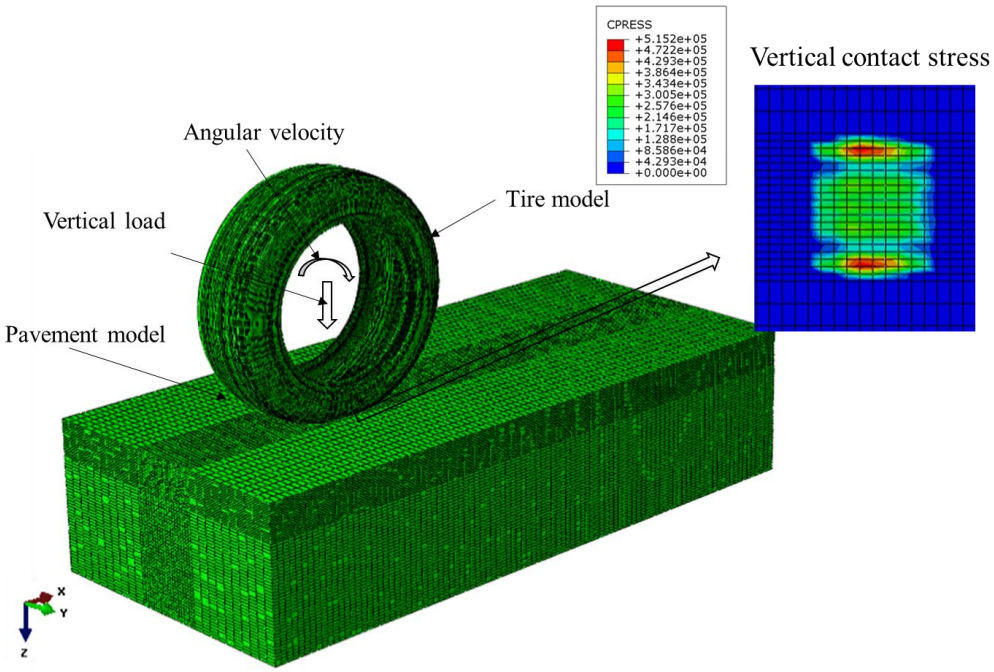

Figure 5.5 Rolling resistance model with 3-D road surface

A linear viscoelastic constitutive model was applied to characterize asphalt surface layer, which can be represented by a generalized Maxwell solid model (Wang 2017). The relaxation modulus of asphalt layer was interconverted from dynamic modulus for material inputs in the FEM as shown in Equation 5-15 and Equation 5-16 (Ferry 1980). The relaxation modulus and relaxation times were determined by minimizing the sum of squares of the errors between the measured and calculated dynamic modulus as indicated in Equation 5-17. The conversion was based on linear viscoelastic theory (Roylance 2001). A constant Poisson's ratio was assumed for the calculation of bulk and shear relaxation moduli.

$$E^{'}(w) = E_{\infty} + \sum_{i=1}^{n} \frac{w^2 \tau_i^2 E_i}{1 + w^2 \tau_i^2} \tag{5-15}$$

$$E^{''}(w) = \sum_{i=1}^{n} \frac{w \tau_i E_i}{1 + w^2 \tau_i^2} \tag{5-16}$$

$$\min \sum_{j=1}^{k} \left[\left(\frac{E^{'}(w)_{calculated}}{E^{'}(w)_{measured}} - 1 \right)^2 + \left(\frac{E^{''}(w)_{calculated}}{E^{''}(w)_{measured}} - 1 \right)^2 \right] \tag{5-17}$$

where,

$E^{'}$ is the real part of the dynamic modulus;

$E^{''}$ is the imaginary part of the dynamic modulus;

E_{∞} is equilibrium relaxation modulus at infinite time;

w is angular frequency;

E_i and τ_i are Prony series parameters for relaxation modulus;

n is number of Maxwell elements;

k is number of data points from the measurements.

The mechanical behavior of viscoelastic materials has strong dependence on temperature. In this study, the temperature dependency of asphalt concrete modulus is presented by time-temperature superposition principle since asphalt concrete has been defined as being thermorheologically simple material. Thus, the temperature effect within asphalt layers can be considered using reduced time (or frequency). This behavior allows for horizontal shifting (along time or frequency axis) of dynamic modulus to establish the single characteristic master curve as a function of reduced time (or frequency) at a specific reference temperature, as shown in Equations 5-18 and 5-19. The value of horizontal shit

can be determined from the time-temperature shift factor. The relationship between the shift factor and the temperature is approximated by Williams-Landel-Ferry (WLF) equation, given in Equation 5-20 (Ferry 1980). The viscoelastic parameter of asphalt pavement layers is presented in Table 5.3.

$$E(t,T) = E(\xi) \tag{5-18}$$

$$\xi = t / a_T \tag{5-19}$$

$$\log(a_T) = -\frac{C_1(T - T_0)}{C_2 + (T - T_0)} \tag{5-20}$$

where,

t is the time before shifting at an actual temperature T;

a_T is shift factor at temperature T;

T_0 is reference temperature;

C_1, C_2 are regression parameters.

Table 5.3 Viscoelastic Parameters of Asphalt Concrete at 25 ºC (Wang 2011)

i	**Surface course**		**WLF**	
	E_i	τ_i		
1	6.31E-01	2.06E-02		
2	2.51E-01	1.73E-01	C_1	18.1
3	8.47E-02	1.29E+00		
4	2.67E-02	5.35E+00		
5	6.66E-03	1.06E+02	C_2	164.7

5.3 Rolling Resistance of Different Pavement Types

This subsection evaluates the effects of pavement types on rolling resistance. Two different types of road surface are considered in the analysis: concrete surface and asphalt pavement surface. The concrete surface was model with smooth flat rigid road surface ignoring pavement thickness. Two asphalt pavement sections were considered in the simulation with asphalt layer thickness of 102 mm and 254 mm, representing thin and thick pavement respectively. The asphalt layers were laid directly on 300 mm lime-modified subgrade. These pavement structure mimics the pavement sections used in the accelerated pavement testing before (Wang 2011; Yoo and Al-Qadi 2008). The simulations of tire rolling resistance were performed for P205/60R16 tire with tire inflation pressure of 187 kPa and vertical load of 3,767 N. The tire was assumed rolling at constant speed of 80 km/h at 25 ºC.

Figure 5.6 shows the calculated tire rolling resistance results on different types of pavement surface. The simulation results show that concrete pavement caused less tire rolling resistance than asphalt pavements. There were 3.0% to 4.4% differences in rolling resistance between asphalt and concrete pavements, depending on asphalt pavement thickness.

To be more specific, the tire rolling resistance on asphalt pavements with asphalt layer thickness of 254 mm and 104 mm were 45.45 N and 44.85 N, respectively, as compared to that on rigid pavement (43.55 N). This indicates that driving on rigid concrete surface can provide better fuel economy and less CO_2 emission. It is worth noting that the asphalt

pavement thickness might not be an influential factor on tire rolling resistance, with less than 1.5% significance between 104 mm and 254 mm asphalt layers. This suggests that increasing pavement thickness may not be an effective approach to reduce tire rolling resistance.

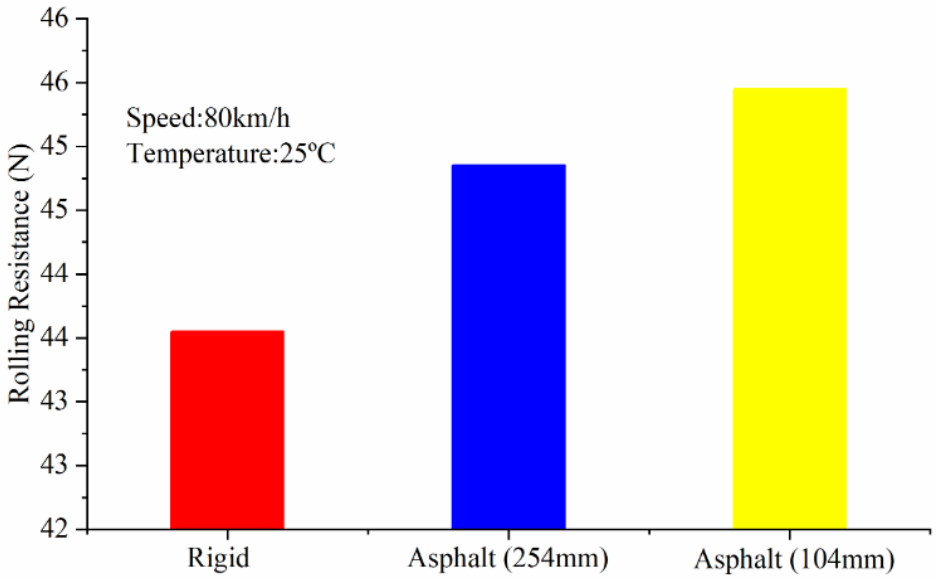

Figure 5.6 Rolling resistance on different pavement types and thicknesses

When tire rotates, the contact patch is constantly experiencing deformation which occurs between tread blocks and road surface. In other words, when the tire crown reaches the contact patch, its circumferential curvature is modified. The tire crown first bends, then flattens, and finally returning to its initial shape. When driving on the flexible pavement, since the surface deflection is larger than that on rigid pavement under the same level of tire load, the tire tread blocks subject to more server deformation, thus more energy is required to maintain vehicle movement.

Figure 5.7 shows that the vertical contact stress and contact area are different when

the same tire travels on different pavement types (the contact stress is shown from the tire aspect, since rigid surface is not deformable). It was observed that due to the deflection of flexible pavement, the tire-pavement contact stress was slightly greater than those on rigid pavement surface, which indicated that more rubber was in contact with rigid pavement surface, thus more energy was dissipated.

The slight difference of rolling resistance between different asphalt pavement thicknesses might be explained from Figure 5.8. At the same vehicle loading level, the thicker asphalt layers result in less vertical displacement, which will in turn lead to less rubber deformation.

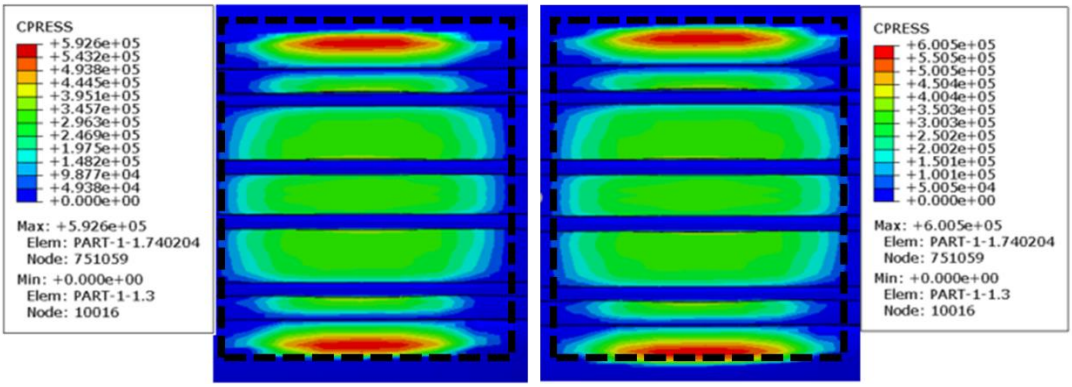

(a) (b)

Figure 5.7 Vertical contact stress and contact area: (a) rigid pavement surface; and (b) asphalt pavement surface (104 mm)

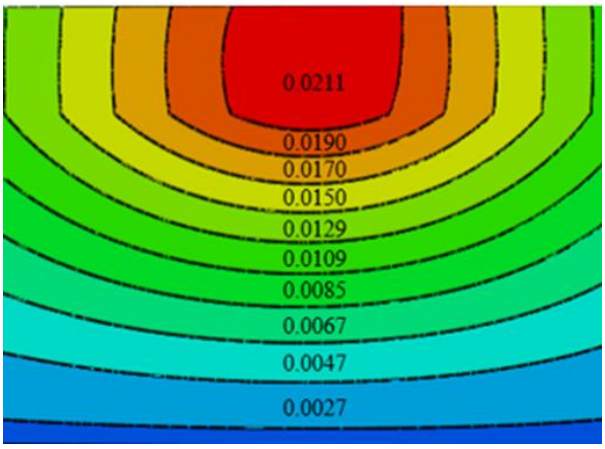

(a)

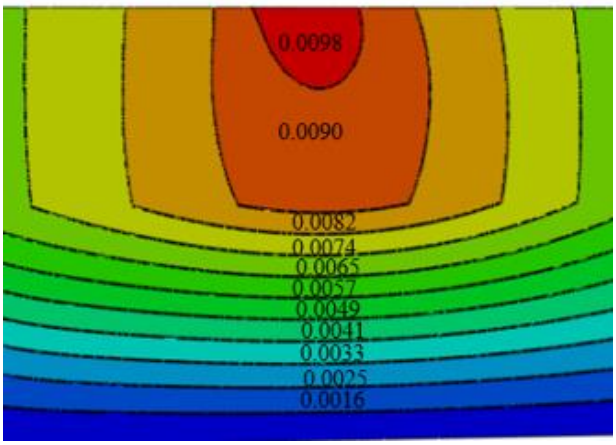

(b)

Figure 5.8 Vertical displacement (mm) in asphalt pavement: (a) 104mm thickness; and (b) 254mm thickness

5.4 Effects of Temperature on Rolling Resistance

Both rubber and asphalt are viscoelastic materials, which mean their material properties are temperature dependent. Tire temperature is dependent on factors such as air temperature, solar radiation, road temperature etc. At the same time, pavement

temperatures are affected by air temperature, solar radiation, wind speed, precipitation and thermal properties of pavement materials (Chen et al. 2017). Leaving aside emergency braking, the internal temperature of rolling tire usually falls within the range of 20 to 60 ºC, depending on the type of vehicle, and environmental temperature. However, it is impossible to describe tire temperature by single value, as each tire component has its own specific temperature different during warm-up and steady state operation (Golbakhshi 2014).

To study the effect of temperature on rolling resistance, the following assumptions were made:

1) the tire temperature and pavement temperature reached steady state, which meant there was no heat transfer between tire and road surface;

2) the temperature within each tire component was evenly distributed. Based on these assumptions, the temperature effect of rubber material could be characterized by the change of loss factor, while the temperature influence of asphalt layer was presented by the change of dynamic modulus due to viscoelasticity.

The tire rolling resistance was calculated under the following conditions: tire inflation pressure of 187 kPa and vertical load of 3,767 N. The tire was rolling at constant speed of 80 km/h at 25 ºC and 50 ºC. Figure 5.9 presents the temperature effect on tire rolling resistance, which considers both pavement temperature and tire temperature.

Results showed that 19% reduction of rolling resistance was found when temperature increased from 25 ºC to 50 ºC. This finding can be supported by the recent field study conducted by Ejsmont et al. (2018), which demonstrated that rolling resistance decreased

drastically with the increase of tire temperature. Within the tire operating range, the amount of energy dissipated by rubber blocks subject to repeated deformation decreased as temperature increased. Thus, the tire rolling resistance was lower when ambient temperature became higher.

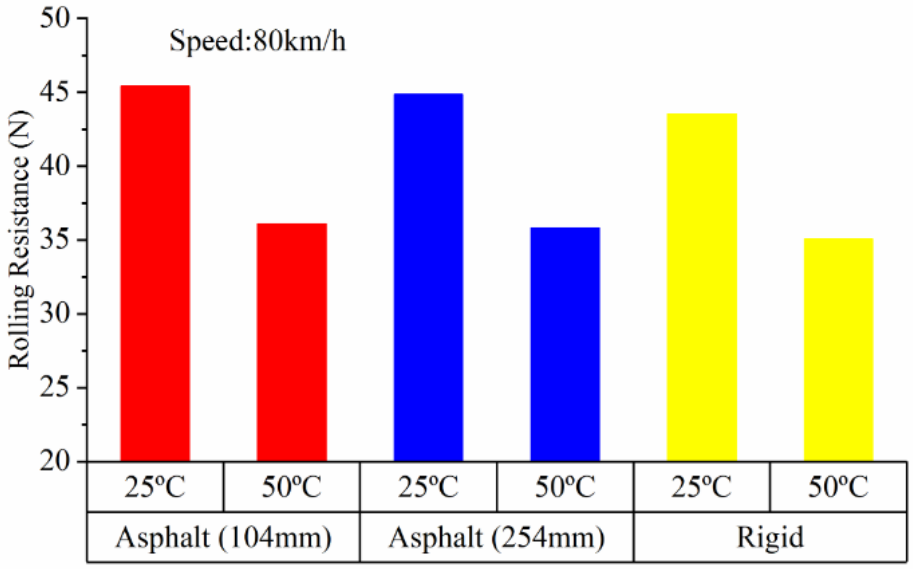

Figure 5.9 Effects of temperature on rolling resistance

To differentiate the temperature effect of pavement from that of tire, another analysis was conducted, in which the loss factor variation of rubber components with temperature was not taken into consideration. In other words, the loss factor of each rubber component was fixed using the value at 25 ºC, even though the pavement temperature increased from 25 to 50 ºC.

The results demonstrate that the change of pavement temperature solely had little influence on tire rolling resistance of passenger car within the temperature range considered in the simulation. For example, the increase of temperature from 25 ºC to 50ºC,

the tire rolling resistance fluctuates around 0.02%.

However, it should be noted, some researchers found that pavement temperature has great impact on pavement structure-induced rolling resistance. For example, Shakiba and Ozer et al. (2016) found that when pavement surface temperature increases from 21 ºC to 40 ºC, there is 22.98% increase of pavement structure-induced rolling resistance (tire load 35.5 kN, tire speed 65 km/h). This may be due to the change of energy dissipation in the pavement due to temperature fluctuation is more significant than the energy dissipation in the tire caused by pavement deformation (without considering energy loss behavior of rubber). Another reason causing the discrepancy could be the load level between passenger car tire and truck tire. The heavy load of truck can cause much greater pavement deformation and may intensify its effect on the energy dissipation in tire, which will be studied in the future work.

The overall results from Figure 5.9 indicate that tire temperature has great impact on tire rolling resistance. Within the tire operating range, the amount of energy dissipated by rubber blocks subject to repeated deformation decreased as temperature increased. Thus, the tire rolling resistance was lower when ambient temperature became higher.

5.5 Fuel Consumption and CO_2 Emission

Low rolling resistance tires are important for both economy and environment. In this section, we specify the contribution of rolling resistance to fuel consumption and CO_2 emission. When driving on a flat road surface, the vehicle's fuel consumption depends on the resistive force (F_{RM}) applying to it, including inertia forces when accelerating ($F_{inertia}$),

aerodynamic drag force (F_{aero}), internal friction $F_{internal}$, total rolling resistance (F_{TR}), which can be obtained from Equations 5-21, 5-22 and 5-23. The Willans line method gives engine a simple relationship between power consumed ($P_{consumed}$) and power required ($P_{consumed}$).

$$F_{RM} = F_{inertia} + F_{aero} + F_{internal} + F_{TR} \tag{5-21}$$

$$F_{aero} = \frac{1}{2}\rho \cdot A \cdot C_D \cdot V^2 \tag{5-22}$$

$$P_{consumed} = a \cdot P_{required} + b \cdot N \tag{5-23}$$

where,

ρ is the air density (1.3 kg/m^3);

A is the vehicle's frontal area in m^2;

C_D is the drag coefficient;

V is tire speed in m/s;

The average value of A and C_D for passenger cars are 2.5 m^2, and 0.32, respectively. $P_{consumed}$ and $P_{required}$ are expressed in W and N is the engine speed in rpm. For a 51 kW petrol engine, a=2.23, b=6.82 (U.S. DOT 2006). Consider a passenger car (engine power: 51 kW, internal friction: 50 N) travelling at a steady speed of 80 km/h on a rigid surface (25 ºC, rolling resistance is presented in Figure 5.6).

According to Equations 5-21 to 5-23, the total resistive force exerted on the vehicle is 481 N. The power required is $P_{required} = F_{RM} \cdot V$ =10,687.82 W. Therefore, at 80 km/h, the vehicle consumes 10,687.82 Wh in one hour. Petrol has an energy value around 9,120

Wh per liter. Thus, for a constant 80 km/h the engine speed is 3,000 rpm, the power consumed is 44,293.84 W. The fuel consumption is 6.07 liters/100 km on rigid surface. Similarly, the fuel consumption on asphalt pavement (thickness: 104 mm) is 6.13 liters/100 km. Assuming that each liter of petrol consumed produces 2.35 kg of CO_2. The total fuel savings and reduction of CO_2 emission due to pavement type and temperature change is presented in Table 5.4.

Table 5.4 Savings of Fuel Consumption and CO_2 Emission

	Fuel consumption (litres)		**CO_2 emissions (kg)**	
	Rigid vs. asphalt pavement	50 ºC vs. 25 ºC	Rigid vs. asphalt pavement	50 ºC vs. 25 ºC
Savings per 100 km	0.06	0.23	0.141	0.541
Annual savings for a car (averaging 21,600 km a year) *(U.S. DOT 2018)*	12.96	49.68	30.456	116.856
Savings during tire lifetime (40,000 km) *(U.S. DOT 2006)*	24	92	57	216
Annual savings for all passenger cars in U.S. (135 million) (*Statista 2018*)	1.750×10^9	6.706×10^9	4.111×10^9	1.576×10^{10}

The results indicate 4.4% reduction of rolling resistance (due to pavement deflection) will lead to fuel savings of 0.07 liters per 100 km. A reduction of rolling resistance of 19% (due to tire temperature increase) will result in fuel savings of 0.23 liters per 100 km. It is

obvious that the fuel consumption is more sensitive to tire temperature change. The overall results show, vehicle fuel consumption and CO_2 emissions are dependent on the vehicle type (such as tire types, engine power, engine speed etc.). There, when studying fuel economy and green gas emission, such factors cannot be ignored.

5.6 Summary

This chapter presented a comprehensive numerical model to quantify the effect of pavement deflection/stiffness, pavement thickness and temperature on rolling resistance, fuel consumption and CO_2 emission. For this purpose, the linear viscoelasticity theory-related concepts were applied to presents the viscoelastic behavior of bituminous pavement. The stress and strain profiles of all tire element groups were obtained, and the hysteresis loops are computed by introducing a viscoelastic phase lag between the stress and strain profiles. The rolling resistance model can successfully quantify the pavement conditions on rolling resistance, fuel consumption and CO_2 emission.

The results demonstrate that rigid road surface can reduce rolling resistance by 3.0% to 4.4% as compared to asphalt pavement. The results also reveal that 4.4% reduction of rolling resistance (due to pavement deflection) will lead to fuel savings of 0.07 litres per 100 km. A reduction of rolling resistance of 19% (due to tire temperature increase) will result in fuel savings of 0.23 liters per 100 km. The study suggests that tire temperature cannot be ignored when studying the effect of pavement conditions on rolling resistance.

The overall results indicate the difference of fuel consumption and CO_2 emission between pavement deflection, pavement thickness and pavement temperature are not

significant. This finding suggests that optimal maintenance of roads with good surface characteristics, such as texture and roughness might be a better way to provide the driving public with greatest possible fuel economy from the pavement infrastructure.

CHAPTER 6 CONCLUSIONS AND RECOMMENDATIONS

6.1 Summary of Research Work

This study built different tire-pavement interaction models to analyze, tire vibration noise, hydroplaning, braking distance, and rolling resistance, respectively, taking into consideration of different pavement surface characteristics.

Tire-pavement noise simulation and prediction

This study developed a coupled FEM/BEM analysis approach for tire-pavement interaction noise simulation and quantified the effects of pavement surface characteristics on the generation and propagation of tire vibration noise. To be more specific, this study analyzed the influence of pavement surface texture and sound absorption on the tire-pavement interaction noise level.

First, a radial tire model was built using FEM. Tire sur-face accelerations under excitation from pavement texture were obtained from the modal analysis. Then, the radiation sound fields caused by tire vibration were calculated using BEM to predict noise levels. The sound absorption effect of porous sur-face layer was considered using a theoretical sound absorption model.

The FEM/BEM model was used to predict the sound pressure level on various pavement surfaces under different surface texture levels and sound absorption coefficients. Numerical prediction results were compared with existing experimental observations and showed consistent trends.

Hydroplaning and braking distance simulation

This research evaluated the hydroplaning risk of multi-lane roadway with PFCs at different rainfall intensities. A comprehensive three-dimensional (3D) fluid-structure interaction numerical model was developed to predict hydroplaning speeds at different water film depths. The grooved tire profile with anti-lock braking (ABS) reflects the real braking conditions of modern passenger car tires.

The water film depths along the traffic lanes were computed from a hydrologic model that couples the surface and subsurface flow of PFCs. The hydroplaning risk was compared between permeable and impervious asphalt pavement surfaces.

The effect of rutting on hydroplaning speeds was investigated. In addition, this study investigated the influencing factors of PFCs related to hydroplaning risk and proposed a design framework and procedure to incorporate hydroplaning risk consideration in roadway design. Finally, this study investigated the braking distance at two different water film depth and compared the value obtained from the AASHTO.

Rolling resistance simulation and prediction

This research investigated tire rolling resistance from the perspective of pavement, considering energy loss in the tire contributed by pavement structure factors. These are pavement types (rigid, flexible) and surface layer thickness. The impact of pavement stiffness on rolling resistance was quantified, taking into account that the aforementioned factors.

The underlying practical question is whether the choice of flexible pavement with asphalt surface or rigid pavement result in the same rolling resistance to passenger cars. To tackle this problem, numerical simulation approach was used, which makes it possible to

eliminate easily all possible sources of energy dissipation other than pavement stiffness/deflection and to avoid experimental difficulties in doing so.

In addition, the numerical approach has the advantages of considering the deformable tire profile under any tire loading condition. In particular, tire rolling resistance resulted from energy dissipation of tire on pavement surface was calculated. The viscoelastic behavior of rubber and the interaction between tire and pavement surface were both considered, which are important factors affecting tire rolling resistance.

6.2 Findings

The findings and conclusions of this research can be summarized as follows:

6.2.1 Tire-pavement Interaction Noise

1) The surface with highest texture level is the nosiest, while the surface with the lowest texture level is the quietest. The difference in overall noise can reach 2.6 dB(A) when the difference of MPD is around 0.7 mm. This finding is consistent with field observations reported in the literature that tire-pavement noise increases with the increasing texture level.

2) The overall noise decreases with the increase of porosity under the same texture level. However, the noise variation due to sound absorption variations of porous pavement is not as significant as the effect of surface texture on noise. For example, the results showed that the overall noise on section 15 was 86.9 dB(A) at 25% porosity and 88.8 dB(A)

at 15% porosity, while the overall noise on section 9 was 89.3 dB(A) at 25% porosity and 91.0 dB(A) at 15% porosity.

3) The porous pavement surface mainly reduces tire-pavement noise at high frequencies.

4) The differences of noise levels at specific frequencies between porous and non-porous surfaces are mainly due to sound absorption spectra of porous surface. If the overall noise is calculated, the benefit of noise reduction on porous surface is around 7 to 10 dB(A).

6.2.2 Hydroplaning and Braking distance

1) The hydroplaning risk increases with the increase of lane numbers, since water film depth increases with drainage length along the traffic lane under a given rainfall rate. For example, under light rain rate, the runoff enters the pores of PFC, and there is no sheet flow on the cross sections with 2 lanes and 4 lanes. However, there is still hydroplaning potential on the 3rd lane and 4th lane on the cross sections with 6 lanes and 8 lanes.

2) In addition, it is obvious that the hydroplaning risk increases with the increase of rainfall intensity. At light to moderate rainfall intensities, the hydroplaning risk for a 2-lane cross section is relatively low, however, at heavy rainfall intensity, the hydroplaning risk increases dramatically, especially for roadway cross sections with a greater number of lanes.

3) The results show that PFC provides better road safety for 2-lane and 4-lane cross sections at the same rain rates. The simulation results provide significant safe driving guidance for both drivers and transportation agencies. For example, during wet weather, it is advised for the drivers to travel at the innermost lane and avoid frequent changing of

traffic lanes, especially driving from an inner lane to an outer lane which will increase the risk of hydroplaning.

4) For transportation agencies, the roadway locations prone to hydroplaning can be treated with reduced speed limits and slippery pavement warning signs as low-cost interim counterplans to improve road safety. For example, at light rain rate, roadways with 8 lanes should be operated at speeds no higher than 118 km/h; but the same roadway should be operated at speeds no high than 97 km/h and 86 km/h, respectively, during moderate rain and heavy rain rates.

5) PFC layer has reduced potential for hydroplaning during light rain and moderate rain conditions as compared to impervious pavement surface, especially at the inner most traffic lane. For example, at light rain rate, there is no sheet flow on the first two lanes for an 8-lane cross section, however, the sheet flow on impervious pavement surface still has hydroplaning potential; at moderate rain rate, the hydroplaning speed for the inner most lane is 121 km/h, which is 11% higher than that on impervious pavement surface. However, it is worth noting that the anti-hydroplaning potential of PFC is not significant at heavy rain event, showing that in areas with frequent heavy rain rate, caution is still needed for drivers travelling on PFC.

6) Pavement rutting significantly increases hydroplaning risk on both permeable and impervious pavements. For example, the hydroplaning speeds on impervious pavements with moderate and severe rutting decrease by 26% and 30%, from 70.9 km/h and 67.3 km/h, respectively, as compared to those on pavements without rutting, which is 96 km/h. This

indicates that pavement with moderate to severe rutting should be given special attention, especially during wet weather conditions.

7) The effect of PFC layer thickness on water film depth was within a certain range and its influence was affected by the rain rate. At light rain, the increase of PFC layer thickness could effectively reduce the water flow depth on pavement surface. However, when the PFC layer thickness increased beyond 5 cm, the PFC layer thickness had little contribution to the surface water drainage.

8) The increase of hydraulic conductivity has positive effect on the reduction of water flow depth on road surface. For example, in light rain condition, the corresponding water film depth was 1.7 mm when the hydraulic conductivity of PFC was 0.2 cm/s. However, at the same rain rate, when the hydraulic conductivity increased to 0.8 cm/s, the water film depth decreased by 41%. When the hydraulic conductivity increased to 1.0 cm/s, there was no water accumulation on road surface. Similar to the effect of pavement thickness, the positive effect of hydraulic conductivity on the reduction of water film depth decreased in moderate to heavy rain conditions.

9) The hydroplaning speed increases with the increase of hydraulic conductivity under light rain. This suggests that the hydraulic conductivity plays a significant role in road safety during light rain condition. While under moderate rain to heavy rain rates, hydroplaning speed was not affected by the PFC layer properties (layer thickness and

hydraulic conductivity). Therefore, speed control should be implemented for road safety. At these scenarios, drivers are advised to drive below 80 km/h to avoid hydroplaning.

10) Although pore clogging has negative effect on hydraulic conductivity, the effect on hydroplaning was only significant at light rain. At moderate to heavy rain rates, the effect of clogging on hydroplaning is very limited. This is similar to the effect of hydraulic conductivity of PFC.

11) The increase of cross slope significantly improves driving safety at rainy condition. For the roadway with eight traffic lanes, the preferred cross slope to fully prevent hydroplaning was found 2% in light rain 4% in moderate rain since there was no water flow under these conditions. In heavy rain, when the cross slope increased from 1.5% to 4.0%, the hydroplaning speed increased by 10%.

12) The skid resistance and braking distance analyses demonstrate that the vehicle braking distance increases with the increasing of water film depths, since the skid resistance decreases with the increasing of water film thickness. It is also indicating that the AASHTO requirements of braking distance cannot be fulfilled at certain water film depth and vehicle speed.

6.2.3 Rolling Resistance

1) Concrete pavement caused less tire rolling resistance than asphalt pavements. There were 3.0% to 4.4% differences in rolling resistance between asphalt and concrete pavements, depending on asphalt pavement thickness. To be more specific, the tire rolling

resistance on asphalt pavements with asphalt layer thickness of 254 mm and 104 mm were 45.45 N and 44.85 N, respectively, as compared to that on rigid pavement (43.55 N).

2) Driving on rigid concrete surface can provide better fuel economy and less CO_2 emission, compared with asphalt pavement surfaces under the same tire load and temperature.

3) It is worth noting that the asphalt pavement thickness might not be an influential factor on tire rolling resistance, with less than 1.5% significance between 104 mm and 254 mm asphalt layers. This suggests that increasing pavement thickness may not be an effective approach to reduce tire rolling resistance.

4) It was observed that due to the deflection of flexible pavement, the tire-pavement contact stress was slightly greater than those on rigid pavement surface, which indicated that more rubber was in contact with rigid pavement surface, thus more energy was dissipated.

5) Results showed that a 19% reduction of rolling resistance was found when temperature increased from 25 ºC to 50 ºC. Within the tire operating range, the amount of energy dissipated by rubber blocks subject to repeated deformation decreased temperature increased. Thus, the tire rolling resistance was lower when ambient temperature became higher.

6) The change of pavement temperature solely had little influence on tire rolling resistance of passenger car within the temperature range considered in the simulation. For

example, the increase of temperature from 25 ºC to 50 ºC, the tire rolling resistance fluctuates around 0.02%.

7) Tire temperature has great impact on tire rolling resistance. Within the tire operating range, the amount of energy dissipated by rubber blocks subject to repeated deformation decreased as temperature increased. Thus, the tire rolling resistance was lower when ambient temperature became higher.

8) The results indicate 4.4% reduction of rolling resistance (due to pavement deflection) will lead to fuel savings of 0.07 litres per 100 km. A reduction of rolling resistance of 19% (due to tire temperature increase) will result in fuel savings of 0.23 liters per 100 km. It is obvious that the fuel consumption is more sensitive to tire temperature change.

9) The vehicle fuel consumption and CO_2 emissions are dependent on the vehicle type (such as tire types, engine power, engine speed etc.). Therefore, when studying fuel economy and green gas emission, such factors cannot be ignored.

6.3 Recommendations for Future Research

This research has developed comprehensive tire-pavement interaction models respectively, for noise simulation, hydroplaning and braking distance, and rolling resistance. In addition, this research studied the effect of pavement surface characteristics on each aspect separately. Although the numerical models can provide accurate results for tire-pavement interactions. There are still some limitations of the model. For example, due to the uncertainties resulted from pavement conditions, the numerical models do not

simulate changes in the water due to dirt or sand for hydroplaning analysis. More research works are needed to connect these functional requirements to pavement design, management, and maintenance strategies. The following are some recommendations for the future works towards this direction:

1) The tire-pavement interaction noise model built in this study only considered tire vibrational noise and thus requires model calibration with field measurement. Future work can be conducted to consider the effect of air pumping on tire-pavement noise to improve model accuracy.

2) The mathematical model of sheet flow used for water film depths prediction only considers cross slopes and ignores the effect of longitudinal slopes on drainage capacity of porous asphalt surface course. The mathematical model can be replaced by numerical water film depth prediction model that considers real geometric design and mixture type of roadways using FEM and fluid dynamics.

3) The hydroplaning model built in this research only took into consideration of vehicles driving on straight road sections. Typically, at curved sections, the cross slopes of traffic lanes between the centerline and the inside edge are higher than the ones in the straight section to counteract centrifuge force, which will affect sheet flow depths on road surface. Therefore, there is a need to conduct hydroplaning risk analysis on curved sections, especially on superelevation transition sections.

4) Many field studies have been conducted to quantify the effect of pavement roughness and texture on rolling resistance, which have more significant influences on

rolling resistance than pavement deflection. Therefore, the rolling resistance prediction model should be extended to cover these surface characteristics.

5) This study built tire-pavement interaction model for noise, safety, and rolling resistance and discussed the influential factors of each function. A further study on pavement surface characteristics incorporating all these aspects is therefore most needed, to guide highway engineers in the selection of appropriate surface mix and texture design for noise, safety, and rolling resistance.

6) PFC has been proven to clog over time which will impair its safety benefits. However, there is still much uncertainty about the mechanism of clogging and the way to prevent it. In the future study, the clogging effect in PFC and how it affects maintenance strategy during service life of PFC should be considered.

REFERENCES

Alvarez, A. E., A. E. Martin, C. K. Estakhri, J. W. Button, C. J. Glover, and S. H, Jung. *Synthesis of Current Practice on the Design, Construction, and Maintenance of Porous Friction Courses*. FHWA/TX-06/0-5262-1, Texas Transportation Institute-Texas A & M University, College Station, TX., 2006.

Alvarez, A. E., A. E. Martin, and C. Estakhri. Drainability of Permeable Friction Course Mixtures. *Journal of Materials in Civil Engineering*, Vol. 22, 2010, pp. 556-564.

Anfosso-Lédée, F., and M. T. Do. Geometric Descriptors of Road Surface Texture in Relation to Tire-Road Noise, *In Transportation Research Record: Journal of the Transportation Research Board*, No. 1806, TRB, National Research Council, Washington, D.C., 2002, pp. 160-167.

Akbarian, M., and F. Ulm. *Model Based Pavement-Vehicle Interaction Simulation for Life Cycle Assessment of Pavements*. Master of Science thesis. Concrete Sustainability Hub, Massachusetts Institute of Technology, Cambridge, MA, 2012.

Allard, J. F. *Propagation of Sound in Porous Media*. Elsevier Applied Science, London and New York, 1993.

Anfosso-Lédée, F., and M. T. Do. Geometric Descriptors of Road Surface Texture in Relation to Tire-Road Noise. *Transportation Research Record*, No. 1806, 2002, pp. 160-167.

Aybike, O., and H. John. Pavement Characteristics Affecting the Frequency Content of Tire/pavement Noise. *Noise Control Engineering Journal*, Vol. 53, 2010, pp. 563-571.

AASHTO. *A Policy on Geometric Design of Highways and Streets*. American Association of State Highway and Transportation Officials, Washington, DC, 2011.

ASTM. ASTM Standard E 274-97. *Standard Test Method for Skid Resistance for Paved Surface Using a Full-scale Tire*. ASTM Standards Sources (CD-ROM), Philadelphia, 2005a.

ASTM. ASTM Standard E 524-88. *Standard Specification for Standard Smooth Tire For Pavement Skid-resistance Tests*. ASTM Standards Sources (CD-ROM), Philadelphia, 2005b.

ASTM. ASTM Standard E 524-08. *Standard Specification for Standard Smooth Tire For Pavement Skid-resistance Tests*. ASTM Standards Sources (CD-ROM), Philadelphia, 2005b.

Agrawal, S. K., and J. J. Henry. Technique for Evaluating Hydroplaning Potential of Pavements. *Transportation Research Record*, No. 633, 1977, pp. 1-7.

ABAQUS. *Analysis User's Manual*. Abaqus, Version 6.10-EF, 2010.

Average Annual Miles per Driver by Age Group. U.S. Department of Transportation, Federal Highway Administration. https://www.fhwa.dot.gov/ohim/onh00/bar8.htm . Accessed July, 17, 2018.

Anderson, D. A., R. S. Huebner, J. R. Reed, J. C. Warner, and J. J. Henry. *Improved Surface Drainage of Pavements: Final Report*. NCHRP Web Document 16, Pennsylvania Transportation Institute, Pennsylvania State University, State College, 1998.

Booz, A. H. *Ten-year Averages from 2002 to 2012 Analyzed by Booz Allen Hamilton, Based on NHTSA Data*, US Department of Transportation, Federal Highway Administration, 2012, http://www.ops.fhwa.dot.gov/weather/q1_roadimpact.htm.

Berbee, R., G. Rijs, R. de Brouwer, and L. van Velzen. Characterization and treatment of runoff from highways in the Netherlands paved with impervious and pervious Asphalt, *Water Environment Research*, Vol. 71, pp. 183-190.

Beckenbauer, T., P, Klein, J. F. Hamet, and W. Kropp, 2008 *Tyre/road Noise Prediction: A Comparison Between the SPERoN and HyRoNE models - Part 1*, in Proceedings of Acoustics08, 2008, Paris, France.

Balmer, G. G., and B. M, Gallaway. *Pavement Design and Controls for Minimizing Automotive Hydroplaning and Increasing Traction*. Frictional Interaction of Tire and Pavement, ASTM STP 793, 1983, pp. 167-190.

Browne, A. L. Mathematical Analysis for Pneumatic Tire Hydroplaning. *American Society for Testing and Materials*, 1975, pp. 75-94.

Browne, A. L. *Dynamic Hydroplaning of Pneumatic Tires*. PhD Thesis, North Western University, USA, 1971.

Bester, C. J. Effect of Pavement Type and Condition on the Fuel Consumption of Vehicles. *In Transportation Research Record: Journal of the Transportation Research Board*, 1984, pp. 28-32.

Benbow, E., J. Iaquinta, R. Lodge, and A. Wright. *Investigation of the Effects of Pavement Stiffness on Fuel Consumption*. Published Project Report PPR 253, TRL Limited, 2007.

Balzarini, D., I. Zaabar, and K. Chatti. Impact of Concrete Pavement Structural Response on Rolling Resistance and Vehicle Fuel Economy. *In Transportation Research Record: Journal of the Transportation Research Board*, 2017, pp. 84-94.

Brebbia, C. A., J. Telles, and L. Wroble. *Boundary Element Techniques: Theory and Applications in Engineering*, Springer-Verlag, 1984.

Bernhard, R., and R. I. Wayson. *An Introduction to Tire/Pavement Noise of Asphalt Pavement*. Institute of Safe, Quiet and Durable Highways, West Lafayette, IN: Purdue University, 2005.

Ball, J. E, and K. Rankin. The Hydrological Performance of a Permeable Pavement. *Urban Water Journal*, Vol. 7, 2010, pp. 79-90.

Chen, J., X. Ma, H. Wang, P. Xie, and W. Huang. Experimental Study on Anti-Icing and Deicing Performance of Polyurethane Concrete as Road Surface Layer. *Construction and Building Materials*, Vol. 161, 2018, pp. 598-605.

Clark, S. K. Rolling Resistance of Pneumatic tire. *Tire Science and Technology*, Vol. 6, 1978, pp. 163-175.

Clapp, T. G., and A. C. Eberhardt. Computation and Analysis of Texture-Induced Contact Information in Tire-Pavement Interaction. *In Transportation Research Record: Journal of the Transportation Research Board*, TRB, National Research Council, Washington, DC. 1986, pp. 23-29.

Coleri, E., J. T. Harvey, I. Zaabar, A. Louhghalam, and K. Chatti. Model Development, Field Section Characterization, and Model Comparison for Excess Vehicle Fuel Use Attributed to Pavement Structural Response. *Transportation Research Record: Journal of the transportation Research Board*, 2016, pp. 40-50.

Coleri, E., and J. T. Harvey. Impact of Pavement Structural Response on Vehicle Fuel Consumption. *Journal of Transportation Engineering, Part B: Pavements*, Vol. 143, 2017.

Copley, L. G. Integral Equation Method for Radiation from Vibrating Bodies. *The Journal of the Acoustical Society of America*, Vol. 41. 1967, pp. 807-816.

Charbeneau, R. J., and M. E. Barrett. Drainage Hydraulics of Permeable Friction Courses. *Water Resources Research*, Vol. 44, 2008, pp. 1-10.

Chow, V. T. *Open-Channel Hydraulics*. McGraw-Hill, New York, 1959.

Coleri, E., M. Kayhanian, J. T. Harvey, K. Yang, and J. M. Boone. Clogging Evaluation of Open Graded Friction Course Pavements Tested under Rainfall and Heavy Vehicle Simulators. *Journal of Environmental Management*, Vol. 129, 2013, pp. 164-172.

Chen, J., H. Wang, and H. Zhu. Investigation of Permeability of OGFC Considering Effects of Anisotropy and Two-Dimensional Flow. *Construction and Building Materials*, Vol. 145, 2017, pp. 218-325.

Chen, J., X. Yin, H. Wang, and Y. Ding. Evaluation of Durability and Functional Performance of Porous Polyurethane Mixture in Porous Pavement. *Journal of Cleaner Production*, Vol. 188, 2018, pp. 12-19.

Clark, S. K. Rolling Resistance of Pneumatic Tire. *Tire Science and Technology*, Vol. 6, 1978, pp. 163-175.

Cho, J. R., J. H. Choi, W. S. Yoo, J. G. Kim, and J. S. Woo. Estimation of Dry Road Braking Distance Considering Frictional Energy of Patterned Tires. *Finite Elements in Analysis and Design*, Vol. 42, 2006, pp. 1248-1257.

Chen, J., H, Wang and H. Zhu. Analytical Approach for Evaluating Temperature Field of Thermal Modified Asphalt Pavement and Urban Heat Island Effect. *Applied Thermal Engineering*, Vol. 113, 2017, pp. 739-748.

Daughaday, H., and C. Tung. *A mathematical analysis of hydroplaning phenomena*, C. A. Lab. Tech. Report No. AG-2495-S-1, 1969.

Descornet, G. *Road Surface Influence on Tire Rolling Resistance*. Surface Characteristics of Roadway: International Research and Technologies STP 1031, American Society for Testing and Materials, Philadelphia, 1990.

Dong, B., L. Zhang, M. Chen, B. Tang, and T. Liu. Influencing Factor of Hydrodynamic Pressure on Tire in Wet Weather Based on Fluent. *Journal of Highway and Transportation Research and Development (English Edition)*, Vol. 7, 2013, pp. 98-104.

Delanne, Y. The Influence of Pavement Evenness and Macrotexture on Fuel Consumption. *Vehicle-Road Interaction*, American Society for Testing and Materials, Philadelphia, PA. 1994, pp. 240-247.

Descornet, G., B. Faure, J. F. Hamet, X. Kestemont, M. Luminari, L. Quaresma, D. Sandulli. *Traffic Noise and Road Surfaces: State of the Art*. Belgian Road Research Centre, Brussels, 2000.

Ding, Y., and H. Wang. BEM-FEM Model for Truck Tire-Pavement Interaction Noise Prediction. *Tire Science and Technology*, Vol. 44, 2016, pp. 212-224.

Ding, Y., and H. Wang. FEM-BEM Analysis of Tyre-Pavement Noise on Porous Asphalt Surfaces with Different Textures. *International Journal of Pavement Engineering*, 2017, pp. 1-8.

Ding, Y., and H. Wang. Computational Investigation of Hydroplaning Risk of Wide-Base Truck Tyres on Roadway. *International Journal of Pavement Engineering*, 2018.

Ding, Y., and H. Wang. Evaluation of Hydroplaning Risk on Permeable Friction Course using Tire-Water-Pavement Interaction Model. *In Transportation Research Record: Journal of the Transportation Research Board*, 2018.

Ejsmont, J. A. *Comparison of Road and Laboratory Measurements and Influence of Some Tire Parameters on Generation of Sound*, Swedish Road and Transport Research Institute, Sweden, 1982.

Eshel. A. A. *Study of Tires on a Wet Runway*, Publication Report No. RR67-24, Annex Corporation, 1967.

Evans, E., and P. Zemroch. Measurement of the Aerodynamic and Rolling Resistances of Road Tanker Vehicles from Coast-down Tests. *Journal of Automobile Engineering*, Vol. 198, 1984, pp. 211-218.

Ebbott, T., R. Hohman, J. P. Jeusette, and V. Kerchman. Tire Temperature and Rolling Resistance Prediction with Finite Element Analysis, *Tire Science and Technology*, Vol. 27, 1999, pp. 2-21.

Ejsmont, J., S. Taryma, G. Ronowski, and B. Swieczko-Zurek. Influence of Temperature on the Tyre Rolling Resistance. *International Journal of Automotive Technology*, Vol. 19, 2018, pp. 45-54.

Franssen, E. A. M., B. A. M. Staatsen, and E. Lebret. Assessing Health Consequences in an Environmental Impact Assessment: the Case of Amsterdam Airport Schiphol. *Environmental Impact Assessment Review*, Vol. 22, 2002, pp. 633-653.

Fujikawa, T., H. Koike, Y. Oshino, and H. Tachibana, H. Definition of Road Roughness Parameters for Tire Vibration Noise Control. *Applied Acoustics*, Vol. 66, 2005, pp. 501-512.

Flintsch, G.W., L. Tang, S. W. Katicha, E. de Leon, H. Viner, A. Dunford, K. Nesnas, F. Coyle, P. Sanders, R. Gibbons, B. Williams, D. Hargreaves, T. Parry, K. McGhee, R. M, Larson, K. Smith. *Splash and Spray Assessment Tool Development Program, Final Report, DTFH61-08-C-00030*, 2014.

Ferry, J. D. *Viscoelastic Properties of Polymers*, John Wiley & Sons, Hoboken, NJ, USA, 1980.

Fwa, T. F., E. Lim, and K. H. Tan. Comparison of Permeability and Clogging Characteristics of Porous Asphalt and Pervious Concrete Pavement Materials. *In Transportation Research Record: Journal of the Transportation Research Board*, No. 2511, 2015, pp. 72-80.

Glennon, J. C. Roadway Hydroplaning-Measuring Pavement Wheel Rut Depths to Determine Maximum Water Depths. Retrieved from: http://www.crashforensics.com/papers.cfm?PaperID=56

Gallaway, B. M., R. E. Schiller and J. G. Rose. *The Effects of Rainfall Intensity, Pavement Cross Slope, Surface Texture and Drainage Length on Pavement Water Depths*. College Station, Texas: Texas Transportation Institute, 1971.

Gallaway, B. M. *Pavement and Geometric Design Criteria for Minimizing Hydroplaning*. Publication FHWA-RD-79-31. FHWA, U.S. Department of Transportation, 1979.

Golbakhshi, H., M. Namjoo, and M. Mohammadi. Evaluating the Effect of Dissipated Viscous Energy of a Rolling Tire on Stress, Strain and Deformation Fields Using an Efficient 2D FE Analysis. *International Journal of Automotive Engineering*, Vol. 4, 2014, pp. 629-637.

Georgiadou, E., K. Kourtidis, and I. Ziomas. *Exploratory Traffic Noise Measurements at Five Main Streets of Thessaloniki*, Greece. Global Nest Journal, Vol. 6, 2004, pp. 53-61.

Gunaratne, M., Q. Lu, J. S. Yang, J. Metz, W. Jayasooriya, M. Yassin, and S. Amarasiri. *Hydroplaning on Multi Lane Facilities*. BDK84 977-14. Florida Department of Transportation Research, 2012.

Gallaway, B. M. *Pavement and Geometric Design Criteria for Minimizing Hydroplaning*. Report No. FHWA-RD-79-31. Federal Highway Administration, Texas Transportation Institute, 1979.

Grogger, H., and M. Weiss. Calculation of the Three-Dimensional Free Surface Flow around an Automobile Tire. *Tire Science and Technology*, Vol.24, 1966, pp.39-49.

Greenwood, I. D., and C. R. Bennett. *Modelling Road User and Environmental Effects in HDM-4*, Association mondiale de la Route/World Road Association, La Defense, France, 2001.

Grover, P. Modeling of Rolling Resistance Test Data. *SAE Technical Paper*, 1998, pp.1-12

Horne, W. B. and R. C. Dreher. *Phenomena of Pneumatic Tire Hydroplaning*. National Aeronaustics and Space Administration, Washington D.C, 1963.

Horne, W., T. Yager. and G. Taylor. *Review of Causes and Alleviation of Low Tire Traction on Wet Runways*, NASA Technical Note, 1968.

Hibbs, B. and R. Larson. *Tire Pavement Noise and Safety Performance: PCC Surface Texture Technical Working Group*. Report No. FHWA-SA-96-068. Federal Highway Administration. Washington, D.C, 1966.

Harrin, E. *Low Tire Friction and Cornering Forces on a Wet Surface*, Technical Note 4406, National Advisory Committee for Aeronautics, Langley Aeronautical Laboratory, Langley Field, VA, 1958.

Hernandez, J., I. L. Al-Qadi, and H. Ozer. Baseline Rolling Resistance for Tires' on-road Fuel Efficiency Using Finite Element Modeling. *International Journal of Pavement Engineering*, 2016, pp.1-9.

Hamzah, M. O., M. R. M. Hasan, and M. Van De Ven. Permeability Loss in Porous Asphalt due to Binder Creep. *Construction and Building Materials*, Vol. 30, 2012, pp. 10-15.

Horne, W. B., and R. C. Dreher. *Phenomena of Pneumatic Tire Hydroplaning*. NASA Technical Note D-2056, NASA, National Aeronautics and Space Administration, 1963.

Highway Research Board. *National Cooperative Highway Research Program Synthesis of Highway Practice 14*. Highway Research Board, National Academy of Sciences, Washington, DC, USA, 1972.

Horne, W. B., and J. A. Tanner. Joint NASA-British Ministry of Technology Skid Correlation Study: Results from American Vehicles. *Pavement Grooving and Traction Studies, NASA SP-5073*, National Aeronautics and Space Administration, Washington, D. C., pp. 325-360.

ISO/CD 11819-2. *Acoustics –Measurement of the Influence of Road Surfaces on Traffic Noise – Part 2: The Close-Proximity Method*, ISO, Geneva, Switzerland, 2000.

Klein. P., T. Beckenbauer, J. F. Hamet, and W. Kropp. Tyre/road Noise Prediction: A Comparison between the SPERoN and HyRoNE Models-Part 2. *Journal of the Acoustical Society of America*, Vol. 123, 2008.

Kropp, W., K. Larsson, and S. Barrelet. *The Influence of Belt and Tread Band Stiffness on the Tyre Noise Generation Mechanisms*. Proceedings. of the international Congress on Acoustics(ICA), USA, 1998.

Kanitpong, K., C. Benson, and H. Bahia. Hydraulic Conductivity (Permeability) of Laboratory-Compacted Asphalt Mixtures. *Transportation Research Record: Journal of the Transportation Research Board*, No. 1767, 2003.

Kramer, O., J. D. Ferry. *Dynamic Mechanical Properties*. Science and Technology of Rubber, San Diego: Academic Press, 1994.

Liao, G., M. S. Sakhaeifar, M. Heitzman, R. West, B. Waller, S. Wang, and Y. Ding. The Effects of Pavement Surface Characteristics on Tire/Pavement Noise. *Applied Acoustics*, Vol.76,2014, pp. 14-23.

Li, M., W. V. Keulen, M. van de Ven, A. Molenaara, and G. Tang. Investigation on Material Properties and Surface Characteristics Related to Tyre-Road Noise for Thin Layer Surfacing, *Construction and Building Materials*, Vol. 59, 2014, pp.62-71.

Leland, T. J. W., T. J. Yager, and U. T. Joyner. *Effects of Pavement Texture on Wet Runway Braking Performance*, NASA Technical Note D-4323, 1968.

Lu, X. *Effects of Road Roughness on Vehicular Rolling Resistance. In Measuring Road Roughness and Its Effects on User Cost and Comfort*. ASTM STP 884. T.D. Gillespie & M. Sayers (eds.). American Society for Testing and Materials, Philadelphia, PA. 1985, pp. 143-161.

Lu, T., N. H. Thom, and T. Parry. *Numerical Simulation of the Influence of Pavement Stiffness on Energy Dissipation*. In Proceedings of the International Conference on Computing in Civil and Building Engineering, Vol. 30, 2010, pp. 483-488.

Lee, H. W., J. R. Cho, W. B. Jeong, K. M. Jeong, and K. W. Kim. Mesh Generation and Hysteretic Loss Prediction of 3-D Periodic Patterned Tire. *International Journal of Automotive Technology*, Vol. 15, 2014, pp. 411-417.

Li, M., H. Wang, G. Xu, and P. Xie. Finite Element Modeling and Parametric Analysis of Viscoelastic and Nonlinear Pavement Responses under Dynamic FWD Loading. *Construction and Building Materials*, Vol. 141, 2017, pp. 23-35.

Li, M. *Tyre-Road Noise, Surface Characteristics and Material Properties*, in Road and Railway Engineering in the Faculty of Civil Engineering and Geosciences, Technical University Delft: Delft, 2013.

Lee, Y. P. K., Y. Liu, Y. Liu and T. F. Fwa. *Skid Resistance Prediction by Computer Simulation*. 8th International Conference on Applications of Advanced Technologies in Transportation Engineering (AATTE). Applications of Advanced Technologies in Transportation Engineering, 2004.

Larson, M., and K. Smith. *Splash and Spray Assessment Tool Development Program*, Final Report, DTFH61-08-C-00030, 2014.

Murad, M., and K. Abaza. Pavement Friction in a Program to Reduce Wet Weather Traffic Accidents at the Network Level. *In Transportation Research Record: Journal of the Transportation Research Board*, TRB, National Research Council, Washington, D.C., 1949, pp.126-136.

McGovern, C., P. Rush, and D. A. Noyce. *State Practices to Reduce Wet Weather Skidding Crashes*, Publication FHWA-SA-11-21, Federal Highway Administration, U.S. Department of Transportation, Washington D. C., 2011.

Martin, C. S. *Hydroplaning of Tire Hydroplaning Final Report*, Project B-608, Georgia Institute of Technology, 1966.

Mosher, L. G. *Results from Studies of Highway Grooving and Texturing by Several State Highway Departments*. Pavement Traction and Grooving Studies, NASA SP-5073, Washington D.C., USA, 1969, pp. 465-504.

Moore, D. F. Prediction of Skid Resistance Gradient and Drainage Characteristics for Pavements. *Highway Research Record*, 1966, Vol. 131.

Miller, J. S., and Y. B. William. *Distress Identification Manual for the Long-Term Pavement Performance Program*. U. S. Department of Transportation, 2003, pp. 90-91.

Mars, W. V. Multiaxial Fatigue Crack Initiation in Rubber. *Tire Science and Technology*, Vol. 29, 2001, pp. 171-185.

Nelson, P. M. *Transportation Noise Reference Book*. London, Boston: Butterworth, 1987.

National Academies of Sciences, Engineering, and Medicine. *Estimating the Effects of Pavement Condition on Vehicle Operating Costs*. Washington, DC: The National Academies Press, 2007.

Nelson, J. T., E. Kohler, A. Öngel, and B. Rymer. Acoustical Absorption of Porous Pavement, *In Transportation Research Record: Journal of the Transportation Research Board*, No. 2058, TRB, National Research Council, Washington, D.C., 2008, pp. 125-132.

Narasimha Rao, R., R. K. Kumar and P. C. Bohara. A Sensitivity Analysis of Design Attributes and Operating Conditions on Tyre Operating Temperatures and Rolling Resistance Using Finite Element Analysis." Proceedings of the Institution of Mechanical Engineers, Part D: *Journal of Automobile Engineering*, Vol. 220, 2006, pp. 501-517.

Nielsen, L., and T. Sandberg. A New Model for Rolling Resistance of Pneumatic Tires. *SAE Technical Paper*, 2002, pp.1-10.

Ongel, A., and J. Harvey. Pavement Characteristics Affecting the Frequency Content of Tire/Pavement Noise, *Noise Control Engineering Journal*, Vol. 58, 2011, pp. 563-571.

O'Boy, D. J., and A. P. Dowling. Tyre/Road Interaction Noise-Numerical Noise Prediction of a Patterned Tyre on a Rough Road Surface. *Journal of Sound and Vibration*, Vol. 323, 2009, pp. 270-291.

Okano, T., and M. Koishi. *Hydroplaning Simulation Using MSC. Dytran*. Proceedings of the 3rd European LS-DYNA Users Conference, Paris, France, 2001.

Oh, C. W., T. W. Kim, H. Y. Jeong, K. S. Park and S. N. Kim. Hydroplaning Simulation for a Straight-Grooved Tire by Using FDM, FEM and an Asymptotic Method. *Journal of Mechanical Science and Technology*, Vol 22, 2008, pp. 34-40.

Ong, G. P., T. F. Fwa, and J. Guo. Modeling Hydroplaning and Effects of Pavement Microtexture. *In Transportation Research Record: Journal of the Transportation Research Board*, No. 1905, 2005, pp.166-176.

Ong, G. P. *Hydroplaning and Skid Resistance Analysis Using Numerical Modeling*, Doctoral, National University of Singapore, 2006.

Ong, G. P., and T. F. Fwa. Transverse Pavement Grooving Against Hydroplaning, I: Simulation Model. *Journal of Transportation Engineering*, Vol. 132, 2006, pp. 441-448.

Ong, G. P., and T. F. Fwa. Part 3: Pavement Surface Properties-Vehicle Interaction: Analysis of Effectiveness of Longitudinal Grooving Against Hydroplaning. *In Transportation Research Record: Journal of the Transportation Research Board*, No.1949, 2006, pp. 113-125.

Ong, G. P., T. F. Fwa and A. Kumar. Transverse Pavement Grooving Against Hydroplaning. II: Design. *Journal of Transportation Engineering*, Vol. 132, 2006, pp. 449-457.

Ong, G. P., and T. F. Fwa. Prediction of Wet-pavement Skid Resistance and Hydroplaning Potential. *Journal of the Transportation Research Board*, 2007, pp.160-171.

Ong, G. P., and T. F. Fwa. Wet-Pavement Hydroplaning Risk and Skid Resistance: Modeling. *Journal of Transportation Engineering*, Vol. 133, 2007, pp. 590-598.

Ong, G., and T. F. Fwa. Modeling and Analysis of Truck Hydroplaning on Highways. *Journal of the Transportation Research Board*, No. 2068, 2008, pp.99-108.

Ong, G., and T. F. Fwa. Runway Geometric Design Incorporating Hydroplaning Considerations, *Journal of the Transportation Research Board*, 2009, pp. 118-128.

Ong, G. P., T. F. Fwa, and J. Guo Modeling Hydroplaning and the Effects of Pavement Micro-Texture. *In Transportation Research Record: Journal of the Transportation Research Board*, No. 1905, Transportation Research Board of the National Academies, Washington, D.C., 2005, pp. 166-176.

Ong G. P., and T. F. Fwa. Transverse Pavement Grooving against Hydroplaning, I-Simulation Model. *Journal of Transportation Engineering*, Vol. 132, 2006, pp. 441-448.

Okano, T., and M. A. Koishi. A New Computational Procedure to Predict Transient Hydroplaning Performace of a Tire. *Tire Science and Technology*, TSTCA, Vol. 29, 2001, pp. 2-22.

Oh, C. W., T. W. Kim, H. Y. Jeong, K. S. Park, and S. N. Kim. Hydroplaning Simulation for a Straight-grooved Tire by Using FDM, FEM and Asymptotic Method. *Journal of Mechanical Science and Technology*, Vol. 22, 2008, pp. 34-40.

Pelloli, R. Road Surface Characteristics and Hydroplaning. *In Transportation Research Record: Journal of the Transportation Research Board*, No. 624, TRB, 1977, pp. 27-32.

Pouget, S., C. Sauzéat, H. D. Benedetto, and F, Olard. Viscous Energy Dissipation in Asphalt Pavement Structure and Implication for Vehicle Fuel Consumption. *Journal of Materials in Civil Engineering*, Vol. 24, 2012.

Park, H., S. K. Youn, T. Song, and N. J. Kini. Analysis of Temperature Distribution in a Rolling Tire due to Strain Energy Dissipation. *Tire Science and Technology*, Vol. 25, 1997, pp.14-28.

Parlett, B. N. Toward a Black Box Lanczos Program. *Computer Physics Communications*, Vol. 53. 1989, pp. 169-179.

Putman, B. J., and L. C. Kline. Comparison of Mix Design Methods for Porous Asphalt Mixtures. *Journal of Materials in Civil Engineering*, Vol. 24, 2012, pp. 1359-1367.

Pacejka, H. B. *Tire and Vehicle Dynamics*. Society of Automotive Engineers, Oxford, 2002.

Roylance, D. *Engineering Viscoelasticity*, Cambridge, MA: MIT Press, 2001.

Rustighi, E., S. J. Elliott, S. Finnveden, K. Gulyás, T. Mócsai, and M. Danti, M. Linear Stochastic Evaluation of Tyre Vibration Due to Tyre/Road Excitation, *Applied Acoustics*, Vol. 310, 2005, pp.1112-1127.

Praticò, F. G., and A. Moro. Permeability and Volumetrics of Porous Asphalt Concrete. *Road Materials and Pavement Design*, Vol. 8, 2007, pp. 799-817.

Rugonyi, S., and K. J. Bathe. On Finite Element Analysis of Fluid Flows Fully Coupled with Structural Interactions. *Computer Modeling in Engineering and Sciences*, Vol. 2, 2001, pp.195-212.

Rose, J. G., and B. M. Gallaway. Water Depth Influence on Pavement Friction. *Journal of Transportation Engineering*, Vol. 103, No. 4, 1997, pp. 491-506.

Sandberg U., and J. A. Ejsmont. *Tire/Road Noise Reference Book*. Informex, Kisa, 2002.

Sandberg, U. Road Traffic Noise-the Influence of the Road Surface and Its Characterization. *Applied Acoustics*, Vol. 21, 1987, pp. 97-118.

Suresha, S. N., G. Varghese, and U. R. Shankar. Laboratory and Theoretical Evaluation of Clogging Behaviour of Porous Friction Course Mixes. *International Journal of Pavement Engineering*, Vol. 11, 2010, pp. 61-70.

Sandberg, U., and G. Descornet, G. *Road Surface Influence on Tire/Road Noise-Part I and II*. Proceedings of. Internoise 80, Miami, Florida, USA, 1980.

Sandberg, U. Road Traffic Noise-the Influence of the Road Surface and Its Characterization. *Applied Acoustics*, Vol. 21, 1987, pp. 97-118.

Stocker, A. J., J. T. Dotson, and D. L. Ivey. *Automobile Tire Hydroplaning-A Study of Wheel Spin-Sown and Other Variables*, Research Report, Texas Transportation Institute Texas A&M University College Station, Texas, 1974.

Staughton, G. C. and T. Williams. *Tyre Performance in Wet Surface Conditions*, Road Research Laboratory Report LR 355, 1970.

Seta, E., Y, Nakajima, T. Kamegawa, and H. Ogawa. Hydroplaning Analysis by FEM and FVM: Effect of Tire Rolling and Tire Pattern on Hydroplaning. *Tire Science and Technology*, Vol. 28, 2000, pp. 140-156.

Sandberg, U., A. Bergiers, J. A. Ejsmont, L. Goubert, R. Karlsson, and M. Zöller. *Road Surface Influence on Tyre/Road Rolling Resistance*. Report MIRIAM_SPI_04. Swedish National Road and Transport Research Institute (VTI), Linköping, Sweden, 2011.

Schmidt, B. *Energy Reduction in the Road Infrastructure Network as a Function of Roads Functional and Structural Conditions*, in 16th International Road Federation World Meeting, Lisbon, Portugal, 2010.

Sumitsawan, P., S. Romanoschi, and S. A. Ardekani. *Effect of Pavement Type on Fuel Consumption and Emissions*. Proceedings of the 2009 Mid-Continent Transportation Research Symposium, Ames, 2009.

Sandberg, U. *Rolling Resistance-Basic Information and State-of-the-Art on Measurement Methods. Swedish National Road and Transport Research Institute (VTI)*. Report No. MIRIAM_SPI_01, 2011.

Shida, Z., M. Koishi, T, Kogure, and K. Kabe. Rolling Resistance Simulation of Tires Using Static Finite Element Analysis. *Tire Science and Technology*, Vol. 27, 1999, pp. 84-105.

Soliman, A. Effect of Road Roughness on the Vehicle Ride Comfort and Rolling Resistance. *SAE Technical Paper*, 2006, pp. 1-11.

Sandberg U., J. A. Ejsmont. Tire/Road Noise Reference Book. Informex, Kisa, 2002.

Sakhaeifar, M., A. Banihashemrad, G. Liao, B. Waller. Tyre-pavement Interaction Noise Levels Related to Pavement Surface Characteristics. *Road Materials and Pavement Design*, Vol. 19, 2018.

Shaw, R. P. Boundary Integral Equation Methods Applied to Wave Problems. *Applied Science Publishers*, Vol. 1, 1979, pp. 121-153.

Schwanen, W., H. M. Leeuwen, A. A. A. Peeters, G. J. Blokland, H. F. Reinink, and W. Kropp. *Acoustic Optimization Tool RE3: Measurement Data Kloosterzande Test Track*, Delft, The Netherlands, 2007.

Sun, L., and B. S. Greenberg. Dynamic Response of Linear System to Moving Stochastic Sources. *Journal of Sound and Vibration*, Vol. 229, 2000, pp. 957-972.

Sun, I. Simulation of Pavement Roughness and IRI Based on Power Spectral Density. *Mathematics and Computer in Simulation*, Vol, 61,2003, pp. 77-88.

Suresha, S. N., G. Varghese, and U. R. Shankar. Laboratory and Theoretical Evaluation of Clogging Behaviour of Porous Friction Course Mixes. *International Journal of Pavement Engineering*, Vol. 11, 2010, pp. 61-70.

Srirangam, S. K., K. Anupam, C. Kasbergen, A, Scarpas, V. Cerezo. Study of Influence of Operating Parameters on Braking Friction and Rolling Resistance. *In Transportation Research Record: Journal of the Transportation Research Board*, No. 2525, TRB, 2015, pp. 79-90

Shakiba, M., H. Ozer, M. Ziyadi, and I. L. Al-Qadi. Mechanics Based Model for Predicting Structure-Induced Rolling resistance (SRR) of the Tire-pavement System. *Mechanics of Time-Dependent Materials*, Vol. 20, 2016, pp. 579-600.

Tielking, J. T. *Conventional and Wide Base Radial Truck Tyres*. Proceedings of the Third International Symposium on Heavy Vehicle Weights and Dimensions, Queen's College Cambridge, UK, 1992, pp. 182-190.

Taylor, G. W., P. Farrel, and A. Woodside. *Additional Analysis of the Effect of Pavement Structures on Truck Fuel Consumption*. National Research Council of Canada (NRC), Ottawa, Ontario, 2000.

Taylor, G. W., and J. D. Patten. *Effects of Pavement Structure on Vehicle Fuel Consumption-Phase III*. Project 54-HV775. Report No. CSTT-HVC-TR-068. National Research Council of Canada, Ottawa, Ontario, 2006.

U.S. Environmental Protection Agency. *Sources of Greenhouse Gas Emissions*, 2016, https://www.epa.gov/ghgemissions/sources-greenhouse-gas-emissions.

Ullitdz, P., B. Schmidt, and O. Nielsen. *Energy Reduction in the Road Infrastructure Network as a Function of Roads Functional and Structural Conditions*. Proceedings of the 16th International Road Federation World Meeting, Lisbon, Portugal, 2010.

U.S. Department of Transportation, National Highway Traffic Safety Administration. *The Pneumatic Tire*, DTO HS 810 561, 2006.

U.S. Automobile Registrations from 2000 to 2016. Statista-the Portal for Statistics. https://www.statista.com/statistics/192998/registered-passenger-cars-in-the-united-states-since-1975/. Accessed July, 17, 2018.

Velinsky, S. A., and R. A. White. Increased Vehicle Energy Dissipation Due to Changes in Road Roughness with Emphasis on Rolling Losses. *SAE Technical Paper*, 1979, pp.1-16.

Wang, H., Y. Ding, G. Liao, and C. Ai. Modeling and Optimization of Acoustic Absorption for Porous Asphalt Concrete. *Journal of Engineering Mechanics*, Vol. 142, 2016.

Wong, J. *Theory of Ground vehicles. 1st ed*. New York: Wiley, 1978.

Walter, J. D., and F. S. Conant. Energy Losses in Tires. *Tire Science and Technology*, Vol. 2, 1974, pp. 235-260.

Williams, F., and T. Dudek. Load-deflection Hysteresis and Its Relationship to Tire Rolling Resistance. *Rubber Division Symposia*, Vol. 1, American Chemical Society, Rubber Div., Akron, OH, 1983, pp. 105-139.

Wolhuter, K. M. *Geometric Design of Roads Handbook*. CRC Press, Boca Raton, Florida, 2015.

Whicker, D., A. L. Browne, D. J. Segalman, L. E. Wickliffe. A Thermomechanical Approach to Tire Power Loss Modeling. *Tire Science and Technology*, Vol. 9, 1981, pp. 2-18.

Wong, J. *Theory of Ground Vehicles*. 1st ed. New York: Wiley, 1978.

Wang, H. and I. L. Al-Qadi, and I. Stanciulescu. Simulation of Tyre-pavement Interaction for Predicting Contact Stresses at Static and Various Rolling Conditions. *International Journal of Pavement Engineering*, Vol. 13, 2012, pp. 310-321.

Wang, H. and I. L. Al-Qadi, and I. Stanciulescu. Effect of Surface Friction on Tire-Pavement Contact Stresses during Vehicle Maneuvering. *International journal of Pavement Engineering*, Vol. 140, 2014.

Wang, H., Y. Ding, G. Y. Liao, and C. F. Ai. Modeling and Optimization of Acoustic Absorption for Porous Asphalt Concrete. *Journal of Engineering Mechanics*, Vol. 142, 2016.

Wang, H., I. L. Al-Qadi, and I. Stanciulescu. Effect of Surface Friction on Tire-Pavement Contact Stresses during Vehicle Maneuvering. *Journal of Engineering Mechanics*, Vol. 140, 2014.

Wong, J. Y. *Theory of Ground Vehicles*. New York, NY: Wiley, 2018.

Wang, H., and M. Li. Comparative Study of Asphalt Pavement Responses under FWD and Moving Vehicular Loading. *Journal of Transportation Engineering*, Vol. 142, 2016.

Wang, H., M. Li, and N. Garg. *Perpetual Pavement Responses under Single and Dual Wheel Aircraft Gear Loading Bearing Capacity of Roads*, Railways and Airfields, Taylor & Francis Group, 2017, pp. 1791-1798.

Wang, H. *Analysis of Tire-pavement Interaction and Pavement Responses Using a Decoupled Modeling Approach (Doctoral dissertation)*. Retrieved from Graduate Dissertations and Theses at Illinois, http://hdl.handle.net/2142/24326, 2011.

Yoshida, T., Y. Osada, T. Kawaguchi, Y. Hoshiyama, K. Yoshida, and K. Yamamoto. Effects of Road Traffic Noise on Inhabitants of Tokyo , *Journal of Sound and Vibration*, Vol. 205, 1997, pp. 517-522.

Yang, J. S. *Tire-Pavement Noise Simulation and Analysis*. Ph.D. Dissertation, National University of Singapore, Illinois, Singapore, 2013.

Yager, T., W. P. Phillips, and W. Horne. *A Comparison of Aircraft and Ground Vehicle Stopping Performance on Dry, Wet, Flooded, Slush, Snow, and Ice-Covered Runways*, NASA Technical Note TN D-6098, 1970.

Yeager, R. W., and J. L. Tuttle. Testing and Analysis of Tire Hydroplaning. *SAE Technical Paper*, 1972, pp. 1-12.

Yoo, P. J. and I. L. Al-Qadi. Truth and Myth of Fatigue Cracking Potential in Hot-Mix Asphalt: Numerical Analysis and Validation. *Journal of Association of Asphalt Paving Technologists*, Vol. 77, 2008, pp. 549-590.

Zhang, L., G. P., Ong, and T. F. Fwa. Investigating the Effect of Asphalt Pavement Texture on Tire/Road Noise: A Finite Element Method-Boundary Element Method (FEM-BEM) Based Approach. *In Transportation Research Record: Journal of the Transportation Research Board*, No. 3754, TRB, 2015.

Zhou, H., G. Wang, J. Yang, and K. Xue. Numerical Simulation of Tire Hydroplaning and Its Influencing Factors, *Applied Mechanics and Materials*, 2014, pp. 580-585.

Zhang, L., G. P. Ong, and T. F. Fwa. Developing an Analysis Framework to Quantify and Compare Skid Resistance Performance on Porous and Nonporous Pavements. *In Transportation Research Record: Journal of the Transportation Research Board*, No. 2369, 2013, pp. 77-86.

Zhang, L., T. F. Fwa, G. P. Ong and L. J. Chu. Analysing Effect of Roadway Width on Skid Resistance of Porous Pavement. *Road Materials and Pavement Design*, Vol. 17, 2016, pp. 1-14.

Zwikker, C., and C. W. Kosten. *Sound Absorbing Materials*, Elsevier Publishing Company, New York, 1949.

Zhou, H., G. Wang, and Y. Ding, J. Yang, C. Liang, and J. Fu. Effect of Friction Model and Tire Maneuvering on Tire-Pavement Contact Stress. *Advances in Materials Science and Engineering*, Hindawi Publishing Corporation, 2015.